Orbital Tori Construction Using Trajectory Following Spectral Methods

DISSERTATION

Ralph E. Bordner III, Major, USAF

AFIT/DS/ENY/10-09

DEPARTMENT OF THE AIR FORCE
AIR UNIVERSITY

AIR FORCE INSTITUTE OF TECHNOLOGY

Wright-Patterson Air Force Base, Ohio

APPROVED FOR PUBLIC RELEASE; DISTRIBUTION UNLIMITED

The views expressed in this document are those of the author and do not reflect the official policy or position of the United States Air Force, the United States Department of Defense or the United States Government.

AFIT/DS/ENY/10-09

ORBITAL TORI CONSTRUCTION USING TRAJECTORY FOLLOWING SPECTRAL METHODS

DISSERTATION

Presented to the Faculty

Graduate School of Engineering and Management

Air Force Institute of Technology

Air University

Air Education and Training Command

in Partial Fulfillment of the Requirements for the

Degree of Doctor of Philosophy

Ralph E. Bordner III, B.S.As.E., M.S.

Major, USAF

September 2010

APPROVED FOR PUBLIC RELEASE; DISTRIBUTION UNLIMITED

AFIT/DS/ENY/10-09

ORBITAL TORI CONSTRUCTION USING TRAJECTORY FOLLOWING SPECTRAL METHODS

Ralph E. Bordner III, B.S.As.E., M.S.
Major, USAF

Approved:

Dr. William E. Wiesel Jr. Dissertation Advisor	Date
Dr. Richard G. Cobb Committee Member	Date
Dr. John Raquet Committee Member	Date
Dr. William P. Baker Committee Member	Date

Accepted:

M. U. THOMAS Dean, Graduate School of Engineering and Management	Date

AFIT/DS/ENY/10-09

Abstract

By assuming the motion of a satellite about the earth's geopotential mimics the known Kolmogorov-Arnold-Moser (KAM) solution of a lightly perturbed integrable Hamiltonian system, this research focused on applying trajectory following spectral methods to estimate orbital tori from sampled orbital data. From an estimated basis frequency set, orbital data was decomposed into multi-periodic Fourier series, essentially compressing ephemerides for long-term use. Real-world Global Positioning System (GPS) orbital tracks were decomposed and reconstructed with error from as low as few kilometers per coordinate axis over a 10-week span to tens of kilometers per coordinate axis over the same time period, depending on the method chosen. These less-than-precision-level results were due primarily to the resonant orbits of the GPS constellation. Additionally, the trajectory following spectral methods chosen experienced difficulties converging on a complete basis set when using data time spans much smaller than the period of the slowest system frequency. However, the lessons learned from GPS led to a new orbital tori construction method. This approach focused on fitting local spectral structures, denoted as frequency clusters, within the sampled orbital data to the analytical form of the windowed, truncated, continuous Fourier transform. Methods employing direct use of the observed spectrum as well as least squares fitting techniques were developed with considerable success. For portions of the low-earth-orbit regime, maximum errors per coordinate axis in orbital tori fits were kept below 5 meters over a time period of 1 year. Simulations using the Hubble Space Telescope yielded 1-dimensional root mean square errors of less than 2 meters in each coordinate axis in the initial and predicted ephemeris fits, both of which used 1-year-long tracks of numerically integrated data.

AFIT/DS/ENY/10-09

Dedicated to my wife; I am really here now.

Acknowledgements

Many describe the effort to obtain a doctoral degree in the military as a high-risk, low-reward endeavor. While the low-reward assertion I challenge, the high-risk statement is spot on. If it were not for the help of many people along the way, I would not have reached this favorable conclusion. To them many thanks is due.

First from a spiritual perspective, thank you Lord for through you all things are possible. My blessings are as uncountable as the number of KAM tori in a lightly perturbed Hamiltonian system.

Next, to my advisor and committee chair, Dr. William Wiesel, I say thank you. C.S. Lewis said the task of a teacher isn't to cut down jungles, but to irrigate desserts. While you may have not cut the Nile river in my mind, you have definitely placed a small spring. Thank you for all of your guidance, patience, and office chats. I look forward to the lifetime of learning that lies ahead.

To my committee, thank you for your time and guidance. Dr. Richard Cobb, Dr. William Baker and Dr. John Raquet, I sought out each one of you not only for your expertise but for your character. Your enthusiasm, professionalism and knowledge were invaluable to me over the last three years.

To my fellow students and friends, thanks for being there. While y'all are simply too numerous to list individually, a special thanks goes to Martin Eilders who helped with the nuances of LaTeX, golf, and much more.

Lastly and definitely most importantly, to my family, and especially to my wife, I say THANK YOU!!! From being a ghost during the first year of the program to being a frustrated grump during the last two years, you have always stood by my side and supported me when I needed it most. There is absolutely no way I could have finished this program without you. I love you all more than words can say.

Ralph E. Bordner III

Table of Contents

Page

Abstract iv

Acknowledgements vi

List of Figures x

List of Tables xiii

List of Acronyms xiv

I. Introduction 1

1.1 An Improbable Fellowship: Transformation, KAM Tori, AFSO 21, Strategic Airlift and GPS 1
1.2 GPS: Past, Present and Future 4
1.2.1 GPS Overview 4
1.2.2 GPS Space Segment Evolution 6
1.2.3 GPS Accuracy Requirements Evolution 8
1.2.4 Accuracy and System Evolution Impact on GPS Operations 9
1.3 Research Solutions for GPS 11

II. Past, Current and Related Research 15

2.1 Basic Theory 15
2.1.1 Integrable Hamiltonian Systems 16
2.1.2 Perturbed Integrable Hamiltonian Systems 21
2.2 Previous and Related Efforts Using KAM Theory 26
2.2.1 Efforts Not Related to Artificial Earth Satellites 28
2.2.2 Previous and Current Artificial Satellite Research 31
2.3 GPS Resonance 34
2.3.1 GPS Constellation History 34
2.3.2 GPS Resonance-related Studies 37
2.4 Possible Effects of KAM Theory on GPS 37
2.5 Summary 41

III. GPS Torus Construction from High-Precision Data 42

3.1 General Approach 44
3.2 High-Precision GPS Orbital Data 45
3.3 The GPS Spectral Content 46
3.4 Fourier Analysis Methods 56
3.4.1 Modified Laskar Method 60

Page

3.4.2 Laskar Decomposition 66
3.4.3 Quick-Look Decomposition Trials with LAGEOS1 70
3.5 The Method of Least Squares 76
3.5.1 Initial Estimates of Fourier Coefficients 77
3.5.2 Least Squares Fit of Frequencies and Coefficients 81
3.6 Summary 88

IV. Spectral Decomposition by Frequency Groupings 91

4.1 Geopotential Model and Satellite Dynamics 93
4.2 A Frequency Cluster-Based Approach 96
4.2.1 Orbit Survey 97
4.3 Decomposition by Frequency Clusters 99
4.3.1 Survey of Results 106
4.4 Least Squares Fit of Frequency Clusters 111
4.4.1 Survey of Results 114
4.5 Low-Frequency Coefficient Correction by Simulated Annealing 122
4.5.1 Simulated Annealing Algorithm 122
4.5.2 Selection of Simulated Annealing Parameters 124
4.5.3 Example of Results 126
4.6 Compare and Contrast Cluster-Based Methods 127
4.7 Orbit Prediction Example with Geopotential Only 128

V. Conclusions 132

5.1 Limitations of Trajectory Following Tori Construction Methods 132
5.2 GPS Orbital Tori 134
5.3 Orbital Spectral Decomposition by Frequency Cluster 134
5.4 Final Conclusions and Recommendations 135

Appendix A. Hamiltonian Dynamics 139

Appendix B. Hamilton Jacobi Theory 142

Appendix C. Notional UERE Analysis 145

Appendix D. Analytic Truncated Fourier Transform of Two Frequencies 149

Appendix E. IGS Data Format Detail 152

Appendix F. Windowed ATCFT Expressions 156

Page

Appendix G. Basis Set Survey 159

Appendix H. Error From a Non-Cluster-Based Approach 160

Bibliography 162
Vita 170

List of Figures

Figure Page

1. GPS Constellation [64] 5
2. Interplay Between GPS Segments 6
3. Position Dilution of Precision (PDOP) [64] 8
4. PDOP During 2007 [64] 10
5. 2-D Harmonic Oscillator 22
6. The Standard Map 27
7. Vertical Accuracy Degradation (in meters) of GPS-like Constellation after 2-years w/o Maneuvering [89] 36
8. Macroscopic GPS Error Components [64] 39
9. L1 Single-Frequency C/A-Code UERE Budget [80] 39
10. Notional Depiction of Orbital Torus Spectra 49
11. PRN22 Spectral Content (220weeks/p=2) 54
12. Evidence of 3rd Body Frequencies (PRN 22/220weeks/p=2) 55
13. 1-Frequency, GPS Torus Fit (PRN22/10 weeks/p=2) 63
14. 2-Frequency, GPS Torus Fit (PRN22/10 weeks/p=2) 64
15. TCFT of 2-Frequency, GPS Torus Fit (PRN22/10 weeks/p=2) 65
16. NAFF Torus Fit (PRN 22/10 weeks/p=5/221 coefs per axis) 67
17. Pre and Post NAFF TCFTs (PRN22/221 coefficients per axis) 69
18. Zoom of TCFT after NAFF (PRN22/221 coefficients per axis) 70
19. TCFT of Test Data ($\Omega_1 = .7$; $\Omega_2 = .361$, p=2, T=1000) 71

Figure Page

20. TCFT of Test Data (Ω_1 = .7; Ω_2 = .361, p=7, T=5000) 71

21. TCFT of LAGEOS1 Data (34 weeks/p=2) 73

22. Z-axis, 20-week LAGEOS1 Torus Fit (p=3/M = (4,8,L6)) 74

23. Z-axis, 1-week LAGEOS1 Torus Fit (p=3/manual expansion) 75

24. Least Squares Torus Fit (PRN22/10 Weeks/M = (6,6)) 88

25. Least Squares Torus Fit (PRN22/52 Weeks/M = (6,6)) 89

26. Spectra of Integrated Orbit (a=1.1 Re, e=0.05, i=30 deg) 97

27. High-Detail Plot of Integrated Orbit's Primary Triplet 98

28. Orbital Survey of Acceptable Ω_3 Magnitudes 99

29. Cluster Decomposition Torus Fit (a=1.1 Re, e=0.05, i=30 deg) 105

30. Comparison of Pre- and Post-Decomposition Transforms 106

31. Torus Fit Error w/o ATCFT (a=1.1 Re, e=0.01, i=0 to 75 deg) 107

32. Error Survey (a=1.1 Re, e=0.01, i=0 to 75 deg) 108

33. Error Survey (e=0.01, i=0 deg, a=1.1 to 1.6 Re) 110

34. Error Survey (e=0.01, i=30 deg, a=1.1 to 1.6 Re) 112

35. Error Survey (a=1.1 Re, e=0.01, i=0 to 75 deg) 115

36. Error Survey (e=0.01, i=0 deg, a=1.1 to 1.6 Re) 117

37. Error Summary (e=0.01, i=30 deg, a=1.1 to 1.6 Re) 118

38. Fourier Transform Snippet Comparison 121

39. Comparison of Fitting Methods, Z-axis Residuals 127

40. HST Orbital Torus Fit (p=2/$M = (6, 14, 6)$) 129

Figure Page

41. HST Orbital Torus 1-yr Prediction Fit ($M = (6, 14, 6)$) 130

42. HST Orbital Torus 1-yr Prediction Fit ($M = (6, 20, 6)$) 131

43. Orbital Survey of Acceptable Ω_1 Magnitudes 159

44. Orbital Survey of Acceptable Ω_2 Magnitudes 159

45. Torus Fit Error w/o ATCFT (i=0 deg, e=0.01, a=1.1 to 1.6 Re) 160

46. Torus Fit Error w/o ATCFT (a=1.1 Re, e=0.01, i=0 to 75 deg) 161

47. Torus Fit Error w/o ATCFT (i=30 deg, e=0.01, a=1.1 to 1.6 Re) 161

List of Tables

Table Page

1. Notional Decrease in UERE by using Orbital Tori (Daily Upload Scenario) 40
2. Summary of Trajectory Following Spectral Methods 44
3. Spectral Decomposition of Main Triplet 49
4. Basis Frequency Set for LAGEOS1 72
5. Summary of Trajectory Following Spectral Methods 93
6. Summary of Trial Cases (a=1.1 Re, e=0.01, i=0 to 75 degrees) 108
7. Summary of Trial Cases (i=0 degrees, e=0.01, a=1.1 to 1.6 Re) 110
8. Summary of Trial Cases (i=30 degrees, e=0.01, a=1.1 to 1.6 Re) 112
9. Summary of Trial Cases (a=1.1 Re, e=0.01, i=0 to 75 deg) 115
10. Summary of Trial Cases (e=0.01, i=0 deg, a=1.1 to 1.6 Re) 118
11. Summary of Trial Cases (e=0.01, i=30 deg, a=1.1 to 1.6 Re) 119
12. Basis Frequency Set for the HST 128
13. Summary of HST Orbital Torus Fit 129
14. Summary of HST Orbital Predication Results 129
15. URE, UEE and UERE for Standard GPS Operations 147
16. URE, UEE and UERE for Notional KAM Tori Model 148
17. Example of SP3 Data Format 155

List of Acronyms

Acronym	Definition
2SOPS	2nd Space Operations Squadron
AFSO 21	Air Force Smart Operations
AMC	Air Mobility Command
ATCFT	Analytical, Truncated, Continuous, Fourier Transform
COE	Classical Orbital Elements
CV	Constellation Value
DFT	Discrete Fourier Transform
DoD	Department of Defense
DSP	Digital Signal Processing
EBK-FFT	Einstein-Brilloiun-Keller Fast Fourier Transform
ECR	Earth Centered Rotating
EOMs	Equations of Motion
GA	Ground Antenna
GLAN	Air Mobility Command
GPS	Global Positioning System
IGS	International GNSS Service
KAM	Kolmogorov-Arnold-Moser
LAGEOS	Laser Geodynamics Satellites
MCS	Master Control Station
MEO	Medium Earth Orbit
MS	Monitor Station
NAFF	Numerical Analysis of the Fundamental Frequency
PPS	Precise Positioning Service
PRN	Pseudorandom Noise
Re	Earth Radii
SA	Selective Availability or Simulated Annealing
SGP4	Simplified General Perturbations Satellite Orbit Model 4
SIS	Signals In Space
SPS	Standard Positioning Service
SVN	Satellite Vehicle Number
TCFT	Truncated, Continuous Fourier Transform
TQM	Total Quality Management
UEE	User Equipment Error
UERE	User Equivalent Range Error
URE	User Range Error
USAF	United States Air Force

ORBITAL TORI CONSTRUCTION USING TRAJECTORY FOLLOWING SPECTRAL METHODS

I. Introduction

1.1 An Improbable Fellowship: Transformation, KAM Tori, AFSO 21, Strategic Airlift and GPS

On 26 June 1948, the British and American military forces began a nearly year-long effort called Operation Vittles, probably better known to most people as the Berlin Airlift. During the course of the 15-month operation, the strategic airlift effort delivered 2,325,509.6 tons of cargo, which included food, coal, and passengers [15]. This operation is considered by many as the greatest humanitarian effort and display of airlift capability in history. In fact, not until Operations Provide Hope, Unified Response and Operation Enduring Freedom had the world seen any effort approach the level of support provided by the Berlin Airlift [32]. From an operational logistics perspective, the world may never again see an operation on the scale of Operation Vittles since the methods of strategic airlift have been vastly improved, mostly due to improved technology. According to Castillo, it took 277,569 flights to deliver the aforementioned 2.3M tons of cargo. With Air Mobility Command's (AMC) modern aircraft, those 2.3M tons could be handled by a little over 30,000 C-17 flights or just under 20,000 fully loaded C-5 aircraft flights. A very stark contrast from the World War II era, where the C-47 and C-54 aircraft could only haul a paltry 6,000 lbs and 19,000 lbs, respectively [7].

While the evolution of the United States' airlift capability has certainly nothing to

do with KAM tori[1], the Global Positioning System, Hamiltonian dynamics or even the most basic aspects of orbital mechanics, it does underscore what the military must do to maintain superiority in the spectrum of military operations, particularly in space: continually change to meet current and future battlefield conditions. Isaac Asimov's quote about change [5], which is nearly identical to that made by Heraclitus almost 2,000 years prior, embodies the spirit of what the Department of Defense (DoD) calls transformation:

> *"The only constant is change, continuing change, inevitable change, that is the dominant factor in society today. No sensible decision can be made any longer without taking into account not only the world as it is, but the world as it will be." – Isaac Asimov*

For those with a little white near the temples (and especially to those with a lot), transformation is not a new concept, rather it is an evolved twist on older ideas. The predecessors to the current transformation and efficient operations foci of the United States Air Force (USAF) and DoD-at-large include total quality management (TQM), continuous process improvement, and probably a number of other business-related initiatives adopted by the DoD of which this researcher is unaware. In particular, the USAF defines transformation as:

> Transformation: A process by which the military achieves and maintains asymmetric advantage through changes in operational concepts, organizational structure, and/or technologies that significantly improve warfighting capabilities or ability to meet the demands of a changing security environment. [50]

In addition to transformation, the USAF has adopted Air Force Smart Operations for the 21st Century (AFSO 21) in order to improve the way it accomplishes its

[1]KAM tori are the surviving invariant tori (i.e. dough-nut shaped surfaces) within the phase space of a lightly perturbed integrable Hamiltonian system.

missions [104]. Thus, while transformation seeks out effects-based changes in weapon systems, thinking and organizational mindset, AFSO 21 focuses on streamlining the already established processes by which it executes its missions. Hence, AFSO 21 is similar to that of Lean Manufacturing, Six Sigma, and other business and/or production management strategies in that it seeks to eliminate waste and redundancy from methods. Regardless of the type of change being sought, the challenge of current USAF leadership is how to bring about change such that it is inline with the DoD's and USAF's transformation and AFSO 21 goals rather than just make things different but the same. Unfortunately, if the latter is accomplished, leadership will cause their constituents to seek comfort as in Spencer Johnson's "Who Moved My Cheese" or empathy in the comical panes of Dilbert rather than bring about true transformation and process improvement.

The work contained within these bindings was done in the spirit and from the perspective of transformation and process improvement. Methods to exploit the implications of KAM theory on earth-orbiting satellites were explored. In particular, the Global Positioning System (GPS), the standardbearer of the United States space-based satellite programs, was critically examined to see if changes within its current orbital mechanics paradigm would translate into meaningful gains in performance and efficiency. GPS is a military system whose success in both the military and civilian arenas is without precedent. The initial 18-satellite constellation has blossomed into a 32-satellite constellation and multi-billion dollar global industry. The once struggling military system has quickly transcended its military roots in a matter of a few decades and is used today as a black-box technology by the average auto operator, precision farmer, hiker, ATM, and even locust swarm tracker! With the civilian, high-precision demand of GPS growing, and past and current success of GPS causing current operational commanders to want more and better GPS, the original operational concept

is being stressed. Thus, it was determined that GPS was ripe to analyze for areas where it may be changed to achieve better performance, and to do so by hopefully working smarter, not just harder.

1.2 GPS: Past, Present and Future

Before instituting any change, one must ask themselves if the change will make the system or process better or if the change is done for change itself. Simply stated, is the system good enough as is? If so, or if change will only bring marginal increase in performance at unproportionate cost, the best course of action may be to maintain the present configuration or process. From a GPS perspective, a good place to begin looking for possible change is to investigate how GPS has matured due to increased civilian use and how this change has affected the original GPS concept of operations. As with any investigation, this search begins with a review of fundamental concepts and definitions.

1.2.1 GPS Overview.

GPS is an all-weather, 24-hour, radio-signal-based, absolute positioning service maintained by the DoD. GPS has two positioning services available for use, the Standard Positioning Service (SPS) and the Precise Positioning Service (PPS). The SPS is the default service available to everyone free of charge while the PPS is for authorized users only, usually the DoD. The GPS enterprise itself consists of three segments: space, control and user [12].

The space segment is simply composed of the orbiting satellites. Each satellite broadcasts a radio signal which is converted into a pseudorange (i.e. the true range plus a timing offset due to differences in user, satellite and GPS clocks) upon reception by a user handset. A minimum of four pseudoranges are required to produce

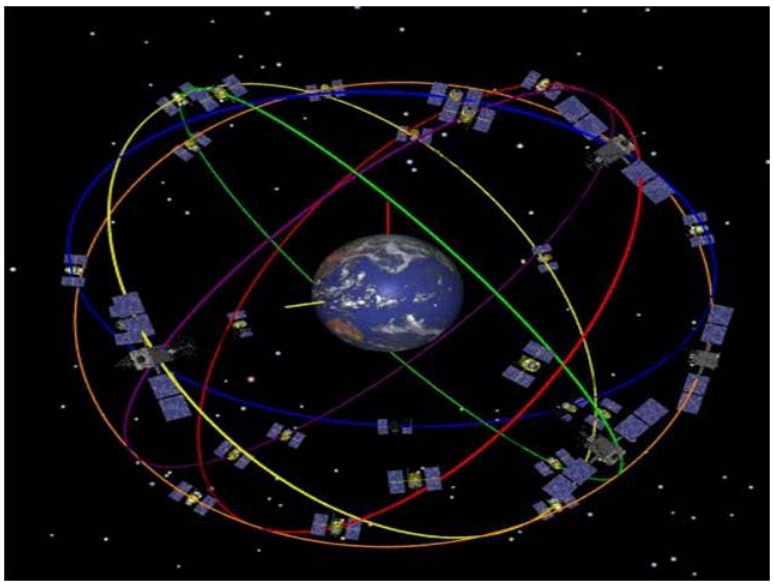

Figure 1. GPS Constellation [64]

a three-dimensional position fix, given no positional assumptions. The satellite constellation is currently baselined at 24 satellites; however, 30 or more active satellites are usually on orbit. In the past, a maximum of 31 active satellites were operating. However, in 2008, the GPS Master Control Station (MCS) infrastructure was updated to accommodate up to 32 actively transmitting satellites [64]. The control segment consists of the personnel and systems that operate, maintain and monitor the GPS satellites and their mission signals. The personnel reside primarily in Colorado Springs at the 2nd Space Operations Squadron (2SOPS), although operations and analysis personnel are scattered all over the world, in particular at Los Angeles AFB. The major control systems include the Ground Antennas (GA), the Monitor Stations (MS), and the MCS. Succinctly stated, the MSs receive the mission signals and transmit them to processing systems and personnel within the MCS. Based on analysis of the mission signals and operational requirements, the MCS uses a GA to contact and upload, if necessary, the GPS satellites with data. From there, the process loops again. A notional, graphical description of this interplay between the GPS control segment components can be seen at Figure 2. The final segment is the

user segment. The user segment consists of all of those who use the GPS signals, military or civilian. By far, this segment is the most dynamic and is the cause of much of the analytical GPS work done over the past several decades. In fact, as the user segment's needs change, so does the design of the space-based system and the ground control infrastructure and personnel that support it.

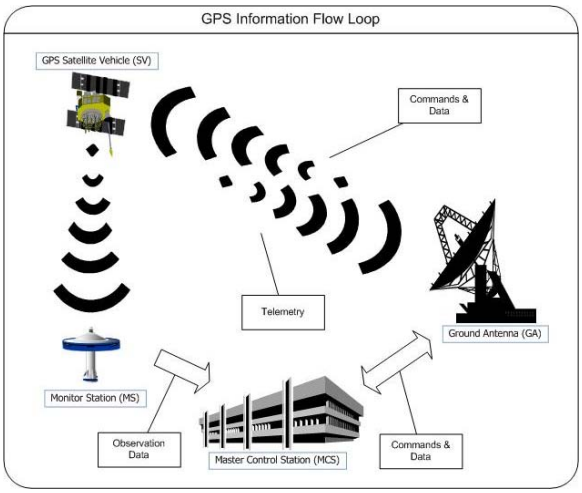

Figure 2. Interplay Between GPS Segments

1.2.2 GPS Space Segment Evolution.

The GPS space segment was originally designed as a 24-satellite, or 24-ball in operator vernacular, constellation with three 63-degree inclined planes of equally divided and spaced satellites. However, it was ordered to be reduced after budget cuts in the early 1980's. This single act set off a flurry of analysis into constellation design options for GPS [63, 13, 11]. Ultimately, an 18-ball constellation (with 3 spares) was selected. The constellation was designed according to a Walker delta pattern scheme of 18/6/2. Explicitly, this means the 18 satellites were equally spaced in six planes, each inclined at 55 degrees, with a relative phasing angle parameter of 2 [65]. The planes' inclinations were reduced from the original specification of 63 degrees to 55 degrees due to launch vehicle constraints after it was decided the space shuttle

would not be the primary launch vehicle. The orbits themselves were chosen to be semi-synchronous with a period of just under 12 hours, which produced an exact repeating groundtrack every 23 hours, 55 minutes and 56.6 seconds [37]. While this constellation was proven to be adequate, Dr. Paul Massat of the Aerospace Corporation optimized this solution. He showed that with 18 satellites and 3 spares using non-uniform spacing, the constellation could maintain its 98 percent worldwide coverage specification with 95 percent less degradation [96]. Eventually, program funds were returned to the system and the constellation was increased to 21 satellites with three on-orbit spares in the mid-1990's. Once again, Dr. Massat, in concert Dr. Rhodus, developed this 21-ball constellation by leveraging the non-uniform spacing concept [71]. Twenty-one satellites were chosen because this number showed to be the minimum needed to provide adequate global coverage based on a performance specification called constellation value, or CV. CV at that time translated to the fraction of the earth and time that four satellites with 5 degree elevation mask angle produced a PDOP of less than 10 [43]. Presently, the PDOP threshold is set at 6 [80]. PDOP stands for Position Dilution of Precision and it is one of the several dilution of precision parameters that have been developed to quantify GPS performance as a function of relative geometry [59]. Thus, the non-uniform design takes into consideration that GPS needs more than just mere visibility to satellites to ensure excellent performance; it needs favorable satellite geometry. Pictorially, PDOP is illustrated by Figure 3 [64]. Mathematically speaking, PDOP is the quotient of the root sum square of the second-moments of the three-dimensional error probability distribution and the standard deviation of the composite error statistic denoted User-Equivalent Range Error (UERE), or:

$$PDOP = \frac{\sqrt{\sigma_{x_u}^2 + \sigma_{y_u}^2 + \sigma_{z_u}^2}}{\sigma_{UERE}}. \tag{1}$$

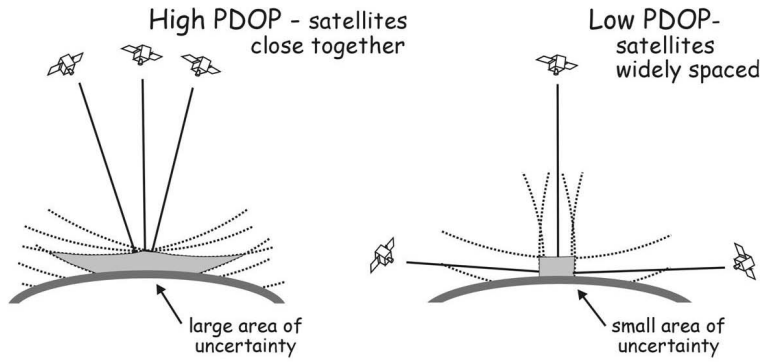

Figure 3. Position Dilution of Precision (PDOP) [64]

To establish the CV for a given GPS constellation, the world is divided into equal-area sample points and then the best PDOP value for those points is calculated every few minutes. Then the ratio of those sample points who have an equal or less value than the threshold PDOP value to the total number of sample points is calculated. This latter result is the constellation's CV [2]. Ideally, the CV is 1, but normally some region of the world will have degraded performance, hopefully some non-useful region, thereby reducing the CV to some value slightly lower than 1.

Due to the success and importance of GPS to the US military and the millions of users worldwide, the constellation is now set to a minimum of 24 satellites. However, 28 or more have been on orbit since the late 1990's and 32 are currently on orbit as of April 2010. Since the constellation has more satellites than for which it was designed, the additional satellites are strategically placed to protect GPS availability and performance due to unexpected satellite outages and/or based on mission need analysis. As one can imagine, as the size of the constellation increased, so did the demand on accuracy of the system.

1.2.3 GPS Accuracy Requirements Evolution.

GPS performance has improved greatly since it first went operational in the 1990's. In 1993, the GPS navigation performance specification for the SPS was $\leq$ 100 *meters*

in the horizontal plane, 95 percent of the time and $\leq$ 156 *meters* in the vertical plane, 95 percent of the time [79]. Since that time, GPS users have gained an increasing intolerance to inaccuracy in the navigation solution. Military commanders want extremely precise navigation signals for their precision munitions to decrease the probability of collateral damage in a strike while the billions of civilian GPS users worldwide have created a plethora of applications which rely on consistently precise navigation solutions, such as aircraft navigation. Since 1993, this growing demand for accuracy caused the intentional degradation of the civilian signals, called Selective Availability (SA), to be turned off and the creation of numerous initiatives to reduce error in the GPS pseudoranges. As a result, the average GPS user today can get very accurate navigation solutions and the most recent GPS SPS specification shows that the average accuracy shall be maintained to $\leq$ 9 *meters* in the horizontal plane, 95 percent of the time and $\leq$ 15 *meters* in the vertical plane, 95 percent of the time. This translates to GPS providing SPS signals in space (SIS) user range error (URE) with less than 4 *meters* rms of error [80]. URE and its close relative user equivalent range error (UERE), which includes the user-induced error due to equipment, are two of the usual pseudorange statistics used when describing GPS performance.

1.2.4 Accuracy and System Evolution Impact on GPS Operations.

Every decision ever made about GPS has had its effects felt at the operational level. From additional training procedures to increased manning profiles, the operational squadron has adapted to meet the challenges set by its users. Obviously, the most significant hurdles overcome have been those challenges created due to changes in constellation configuration and mission requirements as described previously. Since these types of changes increase the amount of care and feeding the constellation demands, they have exacted a price on 2SOPS. Specifically, GPS has experienced an

impressive increase in operations tempo since it first went operational in 1993. According to 2SOPS's statistics from 2007 [27], the operations tempo caused operational crews to perform an average of 2.69 contacts (or sorties in aircraft lingo) per hour per day in order to meet performance specifications. If one considers GPS operates 24 hours a day, 7 days a week, 365 days a year, that contact total sums up to over 23,000 contacts a year. Even with this workload, 2SOPS normally exceeds advertised performance metrics. Figure 4 shows the results of 2SOPS's effort for 2007 from a PDOP perspective [64].

% of a day PDOP ≤ 6	SPS PS	SPS PS	Actual	Time PDOP > 6
Global average	98%	28.8 minutes	99.99%	0.2 minutes
Worst location	88%	2.9 hrs	98.90%	15.8 minutes

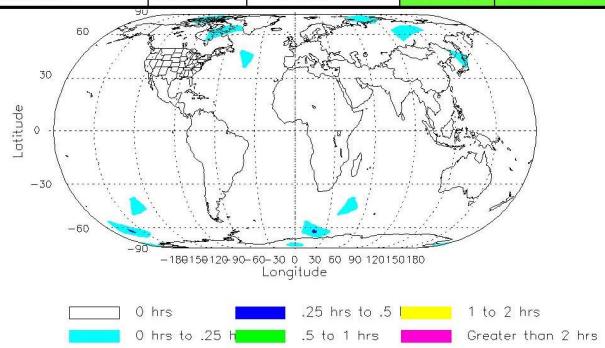

Figure 4. PDOP During 2007 [64]

Roughly speaking and from personal experience of the author, a little more than half of all contacts are primarily done for navigational data update purposes. The other half or so are done to monitor the health of the satellite bus and various payload equipment. Additionally, hidden within the impressive annual contact statistics are continuous maintenance operations, to include maintaining the specified longitude of ascending node, or Geographic Longitude of Ascending Node (GLAN) in GPS parlance, for each satellite. This is done so that PDOP does not suffer to the point of breaking CV tolerances. Each quarter, every satellite is analyzed to determine if an on-orbit maneuver is necessary. If required, maneuver planning begins for those satellites about two weeks prior to the desired maneuver date. The actual maneuver

will cause each satellite to be off-line for 4 to 5 hours, but 2SOPS advertises a 12-hour outage as a worst case scenario [28]. If each of the 32 satellites need to be moved every 12 months on average, this translates to as much as 384 hours of outages a year and over 62 man-weeks of planning effort. Thus, this on-orbit maintenance requires a full section of off-line orbital analysts to be active all year long, and this level of effort does not even include the standard trending and analysis that each satellite's subsystems require. When combined with the Herculean workload already accomplished by the operational crews, it is clear the 2SOPS is an extremely busy squadron.

1.3 Research Solutions for GPS

From the preceding discussion, it is evident that there are areas to improve within GPS. Specifically, any advance in how to maintain satellite constellation geometry and/or reduce operational activity would benefit the 2SOPS and any reduction in the pseudorange errors would be beneficial to the user community. By using a theorem from the 1950's, it is believed both of these areas can be addressed.

In 1954, A. N. Kolmogorov announced a theorem that stated the N-dimensional torus (where N is the degrees of freedom of the system) whose surface is filled with multiply periodic [2], phase space motions of an integrable Hamiltonian system does not disappear as a result of a small change in the system Hamiltonian [62]. Due to contributing work by J. Moser and V. I. Arnold in the early 1960's on this theorem [78, 3], the theorem is now known as the KAM theorem, in their collective honor. Simply stated, the results of this theorem mean that periodic motion of such a Hamiltonian system remains periodic under small perturbations and that the resulting motion is just a deformed version of the original motion. Thus, the complicated 2N phase

[2]Multiply periodic is used here to mean the trajectories of the system experience simple periodic motion in each coordinate, but the frequencies of each axis are not rationally related such that the overall motion is not simply periodic.

space motion of a nonlinear, lightly perturbed system remains highly deterministic. Furthermore, if more than one system lie on the same torus (i.e. multiple satellites), they will maintain their relative geometry on that torus indefinitely. Considering the fact that nearly integrable Hamiltonian systems are often used in celestial mechanics, astronomers have known about and used this theorem for years for natural satellite motion. While little work has been done for artificial satellites, that does not mean it does not apply and thankfully so, as the applicability to GPS performance issues is clear.

Currently, GPS uses the solvable two-body problem approach to model its satellites' motion. As such, it models the earth's geopotential via spherical harmonic coefficients through the 18th order and then stretches the two-body solution such that it approximates (to a desired time span) the actual solution via a perturbing acceleration term. This latter term includes small acceleration terms due to solar pressure radiation, outgassing, body torques and lunar/solar effects [59, 51, 6]. Thus, the GPS satellites are given ephemerides such that for a given 4-hour or 6-hour block of time [59], they will broadcast the osculating, Keplerian classical orbital elements (COE), their time of applicability, and how they change over that time period. Consequently, at only one point in time, known as the ephemeris epoch time, are the COEs "exact". Most of the time they are estimated by correction terms that are based on an approximate solution to the dynamical motion. Clearly, this method is not precise. As the desire for GPS uber-accuracy increases, the community should look for a better method since no matter how exquisitely one estimates yaw rates, body shapes, etc., the resulting dynamical solution is ultimately limited by the underlying model. To better the model, this author believes we must look at the methods of analytical mechanics as it pertains to Hamiltonian systems. By appealing to the KAM theorem, it is the author's assessment that the underlying dynamics model would become

exquisitely precise. Of course, this does not mean that a one-time-solution-for-all-time trajectory can be found. Rather, it simply means that a nearly, all-inclusive solution to the motion of a satellite may be found with less complexity and effort than current methods while at the same time retaining its validity for much longer timespan.

This research's main focus was on applying the KAM theorem to the GPS orbital regime and then subsequently attempting to perform orbital mechanics with the result. The desired end product was an evolutionary upgrade to the current baseline GPS orbital mechanics solution by replacing the current approach of using a solution to the *approximate* orbital motion with what is believed to be an approximate solution to the *actual* motion. This is a subtle but very important difference. Thus, the key questions addressed by this work are clear:

- Can GPS orbits be modeled as KAM tori? If so, will this effort lead to increased GPS accuracy? How much so?
- Can the KAM theorem be applied such that the burden on GPS operations is reduced?

The following chapters detail the effort to answer these questions. Chapter II presents an overview of the underlying theory for this work, past and current research using the KAM theorem as well as a review GPS constellation development and accuracy improvement initiatives. Chapter III expands on the basic theory, and it introduces the approach and methodology used to answer the research questions for GPS. The Laser Geodynamics Satellites (LAGEOS) were also examined to a lesser extent due to some of the difficulties experienced with GPS data. The chapter finishes with results attained and the conclusions drawn from the them. Chapter IV details research on the construction of orbital tori estimates outside of the GPS orbital regime.

Specifically, it takes the lessons learned from Chapter III, develops improved methods and then applies them to orbital regimes more amenable to proposed techniques. The chapter concludes with results and conclusions on these methods. Finally, Chapter V briefly summarizes all efforts undertaken and provides top-level conclusions as well as recommendations for further research.

II. Past, Current and Related Research

2.1 Basic Theory

This research is an empirical and numerical search for, and subsequent exploitation of, behavior that resembles the solutions of what Henri Poincaré called the Fundamental Problem of Dynamics. Stated another way, this research is interested if the observed orbital motion of a satellite, and in particular a GPS satellite, mimic the known solutions of a system whose Hamiltonian function, $\mathcal{H}$, is that of an integrable Hamiltonian function, $\mathcal{H}_{integrable}$, plus that of small perturbation, $\mathcal{H}_{perturbation}$. Mathematically, this can be written as:

$$\mathcal{H} = \mathcal{H}_{integrable} + \epsilon \mathcal{H}_{perturbation}, \tag{2}$$

where ϵ is a small perturbation parameter.

Much work has been done over the past several hundred years regarding perturbation techniques within the field of celestial and orbital mechanics, and arguably the most celebrated and extensive work was accomplished by Poincaré, which culminated in 1899 [88]. Even as magnificent as this work was and still is, the methods contained within it ultimately diverge over large timescales due to the problem of small divisors. Thus, it wasn't until the 1950's that solutions to Equation 2 for a majority of initial conditions and Hamiltonians were found. As mentioned previously, this landmark achievement was initially accomplished by Andrey Kolmogorov [62]. His work was later rigorously verified by Moser and Arnold [78, 3], resulting in the KAM theorem. However, prior to presenting the formal details and impact of this theorem, a brief emphasis of a few underlying theoretical concepts is needed.

2.1.1 Integrable Hamiltonian Systems.

To begin this discussion, let us consider only dynamical systems that possess a single function which contains the total description of their system's motion. In the study of Hamiltonian dynamics, this function is appropriately named the Hamiltonian, denoted here as $\mathcal{H}$ [73]. The equations of motion of this dynamical system are found by applying the well-known Hamilton's Equations to the system Hamiltonian:

$$\dot{q}_i = \frac{\partial \mathcal{H}}{\partial p_i} \tag{3}$$

$$\dot{p}_i = -\frac{\partial \mathcal{H}}{\partial q_i}, \tag{4}$$

where q_i and p_i are the generalized coordinate and momenta variables, respectively. See Appendix A for a brief review of Hamiltonian dynamics. Hamiltonian systems possess two special properties that in the context of invariant tori, should be stressed: their symplectic nature[1] and their preservation of volume within the Hamiltonian flow. To illustrate these qualities, first recall the definition of the Poisson bracket for any two functions F and G [40]:

$$[F, G]_{\mathbf{q},\mathbf{p}} = \sum_j \left(\frac{\partial F}{\partial q_j} \frac{\partial G}{\partial p_j} - \frac{\partial F}{\partial p_j} \frac{\partial G}{\partial q_j} \right). \tag{5}$$

Thus, under this definition, the Hamiltonian equations of motion become:

$$[q_i, \mathcal{H}] = \dot{q}_i \tag{6}$$

$$[p_i, \mathcal{H}] = \dot{p}_i. \tag{7}$$

[1]Hamiltonian flow in the phase space preserves a symplectic structure, meaning the 2-form on the manifold remains invariant.

Poisson brackets are commonly used in canonical transformation theory and in determining canonical invariants. One such invariant is the differential symplectic area. The symplectic condition of Hamiltonian mechanics states that the differential symplectic area, defined as:

$$\delta \mathbf{p}_u \cdot \delta \mathbf{q}_v - \delta \mathbf{q}_u \cdot \delta \mathbf{p}_v, \tag{8}$$

where u and v are infinitesimal vectors within the Hamiltonian vector field, is independent of time. According to Ott, this can be described as the conservation of the algebraic sum of the parallelogram areas formed by projecting the infinitesimal vectors to the N conjugate coordinate planes (p_i, q_i) [82]. This means infinitesimal areas are preserved in Hamiltonian flow. Due to this property, it is an easy extrapolation to say symplectic areas are conserved. The symplectic area is defined by the Poincaré's invariant integral of the first order as:

$$J_1 = \oint_S \mathbf{p} \cdot d\mathbf{q}, \tag{9}$$

where J_1 is invariant over the path. Similar to that of differential symplectic area, this means that the symplectic area is constant over the phase space and is independent of time. By taking Poincaré's invariant integral to the $2N$ order, it can be shown the symplectic condition implies the volume of the dynamical phase flow of the system is conserved [73]. This incompressibility condition of the phase space flow is called Liouville's theorem and it allows us to make assumptions about invariant tori after perturbation, namely that they are deformed yet maintain their phase space volume. It can be further shown that Hamiltonian systems also act like an ideal fluid. Thus, not only do infinitesimal volumes maintain a constant value (no matter the deformation experienced), but the circulation around an arbitrary number of phase space

trajectories is also constant. Equation 9 will prove valuable later as we shall see it can be used to explicitly find one half of a coordinate transformation that constructs the desired KAM torus in question from the native coordinates and conjugate momenta.

The intent of dynamical methods based on energy relationships like the Hamiltonian formulation is to reduce an otherwise unwieldy or "impossible" Newtonian dynamics problem into a much more reasonable (and hopefully completely solvable) problem. In and of themselves, the Hamiltonian equations of motion found beginning at Equation 3 do not immediately or necessarily make the dynamic equations simple to solve. While it is intuitively clear there is a benefit to $2N$ first-order differential equations, it is usually not until further manipulation of the problem that the true benefit of the Hamiltonian formulation of dynamics is revealed. A usual first step in making the problem simpler is to find constants within the problem, commonly referred to as integrals of the motion. Integrals of the motion reduce the dimension of the problem by an amount equal to their number as they are a form of natural constraint. Thus, the time evolution of one coordinate is solved without having to resort to solving the equation of motion. One test for explicitly finding integrals of the motion is that of the aforementioned Poisson bracket.

To demonstrate this, let us now further restrict our set of dynamical systems to those Hamiltonian systems that are conservative and whose Hamiltonian functions themselves are time-independent. Using the definition of the Poisson bracket at Equation 5, the result of the bracket of the Hamiltonian with any constant function independent of the coordinates and momenta is quickly shown to be:

$$
\begin{aligned}
[c, \mathcal{H}]_{\mathbf{q},\mathbf{p}} &= \sum_j \left(\frac{\partial c}{\partial q_j} \frac{\partial \mathcal{H}}{\partial p_j} - \frac{\partial c}{\partial p_j} \frac{\partial \mathcal{H}}{\partial q_j} \right) && (10) \\
&= \frac{d\mathcal{H}}{dt} && (11) \\
&= 0. && (12)
\end{aligned}
$$

Thus, by the properties of a Poisson bracket, it is shown that the bracket is zero as well as the total time derivative of the Hamiltonian. This, of course, is true for all conservative, time-independent Hamiltonians. However, in general, c does not have to be independent of the coordinates and conjugate momenta. In fact, if Equation 10 holds for any general constant function c, then c is an integral of the motion and we have demonstrated a viable, albeit somewhat ad hoc, way to test for integrals of the motion [40].

It is usually desired to have as many integrals of the motion as possible. In fact, if $2N$ integrals of the motion could be found for an N-degree-of-freedom problem, the solution of the dynamical motion in phase space is the time-evolution of a set of constant-valued functions. Theoretically, this could be done by using the Poisson bracket property shown previously that the bracket of a integral of the motion and a time-independent Hamiltonian is zero. Once two integrals have been found, the rest can be constructed via Jacobi's identity [40]. However, this method usually does not produce viable results. A more common and productive approach would be to use canonical transformations via Hamilton-Jacobi theory [97]. See Appendix B for a review of Hamilton-Jacobi transformation theory. The important result of Hamilton-Jacobi theory is that it is sometimes possible to find a canonical transformation, i.e. one that preserves the symplectic form of Hamilton's equations, that literally *solves* a dynamical problem. An important class of dynamical systems is the one composed

of integrable ones. A system is defined as integrable if N independent integrals of the motion are found. While such systems are rarely found naturally, many systems are very close to integrable systems. Hence, integrable and nearly integrable systems are very well studied and used, and they are the systems of which this work will restrict itself. Section 2.1.2 will cover extending integrable systems to nearly integrable ones.

Now, to continue this discussion, we need to further restrict our pool of dynamical systems to those that are not only integrable, but also periodic. However, since this work is concerned with the analysis of orbiting artificial satellites, this really is not much of a restriction. When a dynamical system is periodic, it is often very useful to transform the native, generalized coordinates and momenta into more useful variables called action and angle variables. This transformation effectively makes the system Hamiltonian a function of the constant momenta variables alone and allows the underlying motion to be seen much more clearly. Integrable, periodic Hamiltonian systems are said to have quasi-periodic, or multiply periodic, motion. Quasi-periodic means the motion is composed of periodic motion with N fundamental frequencies, Ω_j, and it can be modeled as a N-tuple Fourier series of the form:

$$f(t) = a_{n_1 \ldots n_N} exp(i(n_1\Omega_1 t + n_2\Omega_2 t + \cdots + n_N\Omega_N t)), \tag{13}$$

where $n_1, n_2, \ldots, n_N$ are extended to any desired order M in each orthogonal axis. Thus, the end Fourier series representation will be a set of M-order Fourier series coefficients in each coordinate axis and one full set of N independent frequencies (i.e. common to all axes). In the limit, the Fourier transform of such a series will yield delta functions at each integer linear combination of the basis frequencies [82]. From an equations of motion (EOMs) perspective, the quasi-periodic motion can be described in terms of the ironically named constant *action*, I, and linearly varying *angle*, θ, variables:

$$\dot{I}_j = 0 \tag{14}$$

$$\dot{\theta}_j = \frac{\partial H(I)}{\partial I_j} = \omega_j(I). \tag{15}$$

In this case, the phase space motion is restricted to lie on the surface of an N-dimensional torus, also referred to as an N-torus [4, 21]. If the fundamental frequencies are incommensurate (i.e. irrational), then the motion of the system will densely fill the surface of what is called a nonresonant torus. Otherwise, the motion will lie on a resonant torus and the system trajectories will close upon each other according to the winding number, also called the rotation number, of the system [82]. As an example, consider a two-degree-of-freedom harmonic oscillator (2DHO). With $N = 2$, the phase space is four-dimensional, thus the constant energy surface is a three-dimensional manifold and exists as the wrapping of a 2-torus. This wrapping is where the system trajectories exist. Figure 5.1 demonstrates this graphically, where the blue lines represent the phase space trajectories of the system. Figure 5.1 represents one energy level set for the 2DHO. If we assume a small random number of nearby initial conditions, plot all of the resulting invariant tori as nested tori, and then take a cross-section of this entire structure, we would obtain the Poincaré surface of section found at Figure 5.2. It must be emphasized that only a small number of the uncountably infinite number of nested tori are depicted here.

2.1.2 Perturbed Integrable Hamiltonian Systems.

Getting to the point of describing a periodic, integrable Hamiltonian system was somewhat lengthy. To make it worse, not many real systems can be literally described and subsequently analyzed based on this type of model. Thankfully, this is not a dead end for real-world applicability of the concept. It is a common hypothesis that many

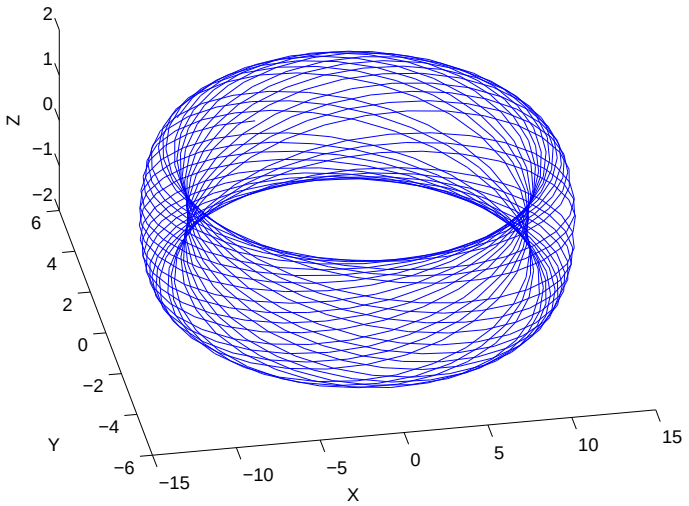

5.1: Single Set of Torus Trajectories

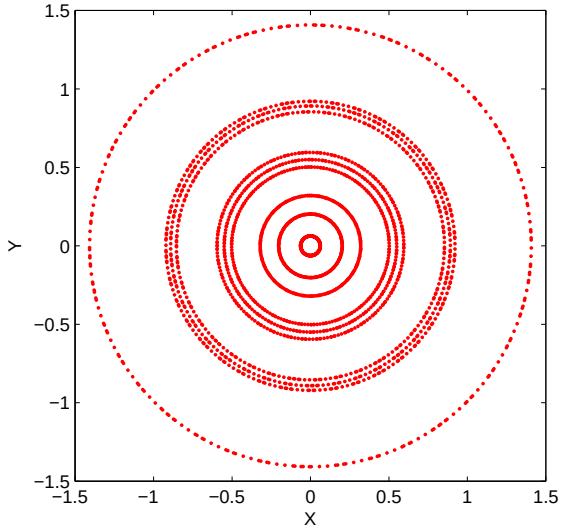

5.2: Poincaré Surface of Section of Torus

Figure 5. 2-D Harmonic Oscillator

systems can be modeled as a variation to the aforementioned and this hypothesis is the underlying assumption of this work. Hence, recall Equation 2. If we rewrite this to incorporate action-angle notation and assume the standard perturbation theory terminology, the fundamental equation becomes:

$$\mathcal{H}(\mathbf{I}, \theta) = \mathcal{H}_o(\mathbf{I}) + \epsilon \mathcal{H}_1(\mathbf{I}, \theta), \tag{16}$$

where once again ϵ is a small, real perturbation parameter much less than 1, and $\mathcal{H}_o$ and $\mathcal{H}_1$ are real, analytic functions. The solution to this problem perplexed many for many years. As indicated previously, Poincaré called it the Fundamental Problem of Dynamics, and in 1954 A. N. Kolmogorov conjectured with an outline of a proof that:

> **Theorem.** *If an unperturbed system is nondegenerate, then for sufficiently small conservative hamiltonian perturbations, most non-resonant invariant tori do not vanish, but are only slightly deformed, so that in the phase space of the perturbed system, too, there are invariant tori densely filled with phase space curves winding around them conditionally periodically, with a number of independent frequencies equal to the number of degrees of freedom. These invariant tori form a majority in the sense that the measure of the complement of their union is small when the perturbation is small.* [4]

Like most theorems, this one was "easily" stated and "carefully" proven nearly 10 years later by Arnold and Moser. Since the proofs are exceedingly long and intricate, they will not be included here. Rather, only a summary of the importance of the result will be discussed since the result is key to this work and not the proof of the theorem itself. However, the proofs can be found easily in the literature. With a little extra effort, they can be found in English-translated form [3, 78, 62].

Essentially, the KAM theorem takes the perturbed Hamiltonian at Equation 16, assumes an N-dimensional tori exists, and then seeks out an action-angle coordinate

transformation to map the perturbed Hamiltonian to that of a new one such that it is a function of the new action variables only (similar to that described in Section 2.1.1):

$$\mathcal{H}(\mathbf{I}, \theta) = \mathcal{H}^{'}(\mathbf{I}^{'}). \tag{17}$$

The new Hamiltonian, $\mathcal{H}^{'}$, is found by solving the Hamilton-Jacobi equation for the generating function, S:

$$\mathcal{H}'(\mathbf{I}') = \mathcal{H}\left(\frac{\partial S(I', \theta)}{\partial \theta}, \theta\right). \tag{18}$$

Once found, the transformation to switch between old and new coordinates/momenta is accomplished via standard techniques. The initial proofs of Kolmogorov's theorem were to solve the Hamilton-Jacobi equation at Equation 18 through *superconvergent*, iterative methods similar to Newton's method, thereby circumventing the problem of small divisors [4]. The rapid convergence is possible via this type of approach since the series is approximated at each step using best estimate available rather than with the series initially used. The KAM theorem shows the solutions converge quickly when the perturbations are *sufficiently small* and the N frequencies are *sufficiently incommensurate*, thereby showing perpetual stability for the system. While the definition of sufficiently small is often conditional to a particular problem, the term sufficiently incommensurate has been shown to explicitly mean that the independent frequencies must meet the diophantine condition from number theory of [14]:

$$\left|\sum_{i=1}^{N} a_i \omega_i\right| \geq C\|a\|^{-\nu} \; for \; all \; a = \{a_1, a_2, \ldots, a_n\} \in \mathcal{Z}^n, \tag{19}$$

where $C \geq 0$ and $\nu \geq 0$. From the perspective of Lebesgue measure, the survival of invariant tori was found to happen *most* of the time, and as ϵ goes to zero, so does the size of the phase space volume not containing invariant tori. These tori exist on a Cantor set which does not contain any open set, even though its measure is large [30]. Therefore, the probability of a perturbed, nearly integrable, periodic system not being described by an invariant, deformed tori in phase space is small [4]. For those resonant tori whose frequencies are approximated by rationals, they find themselves destroyed after a perturbation and they are often replaced by pairs of hyperbolic and elliptic orbits in the vacated phase space. These orbits are accompanied commonly by chaotic orbits as well [82]. While not a true Poincaré surface of section, Figure 6.1 shows a plot of the well-known Standard Map under some slightly perturbed initial conditions. The large, concentric KAM structures are clearly evident. The collections of loosely organized dots and smaller KAM structures within the plot notionally represent the destruction of previously unperturbed KAM tori into chaotic orbits, island chains of resonant tori (i.e. elliptic orbits) and hyperbolic orbits. Figure 6.2 is a close-up of the detail near a resonant perturbation. The elliptic orbit structure is evident on the left and right of the figure while the hyperbolic asymptotes are suggested by the detail in the center of the figure. Once again, the lack of pattern in the dots suggests possible chaotic orbits.

As alluded to above, the common stumbling block in strict, analytical applications of the KAM theorem is the term *sufficiently small* perturbations. It can be stated generally that many believe the solar system (and consequently the earth-moon system) cannot be modeled via the KAM theorem since the restriction on the size of the perturbation parameter (which is routinely assessed to be the ratio of the main-body masses in the problem) is normally violated [21]. However, this does not mean the principle ideas within KAM theory cannot be exploited in the earth-moon system

with artificial satellites. This is due to the fact that while it is sufficient for perturbations to be small for tori to exist, the theorem does not state that it is necessary since the absence of small perturbations does not mean tori do not exist. While most research has approached applying the KAM theorem to find invariant KAM tori from an analytical perspective, this work attempted to do a numerical search for the KAM tori themselves and then back out an analytical approximation of the tori according to current theory. Hence, it was hoped that invariant tori could be found in the earth-moon system even though current analytical methods may fail to find them in the general case. For a review of recent analytical work, to include that of computer-aided analytical research, a 2006 paper by Celletti does an excellent summary of analytical KAM theory work done in the solar system [21]. Should third body perturbations prove to be too large for KAM to apply to Earth orbiting satellties, it was hoped that Nekhoroshev's theorem regarding the *effective* stability of nearly-integrable systems (as opposed to the KAM theorem's statement of perpetual stability) would still apply [81]. This theorem has been interpreted by some as meaning that KAM tori are "sticky" and thus, some general phase space trajectories near KAM tori remain "stable" on exponential timescales [87, 76]. However, a more useful result for this work may have been found by Deshalms and Guitérrez [30]. According to their proof of Nekhoroshev's theorem, it may be possible to find trajectories that essentially appear to reside on KAM tori and will remain so on timescales sufficiently long enough for satellite applications. They define these apparent tori as nearly invariant tori.

2.2 Previous and Related Efforts Using KAM Theory

While KAM theory is nearly 50 years old, its use on significant applied research problems has been limited. This is partly due to the restrictions placed on the theory itself; the dynamical system in question needs to be nearly integrable with only small

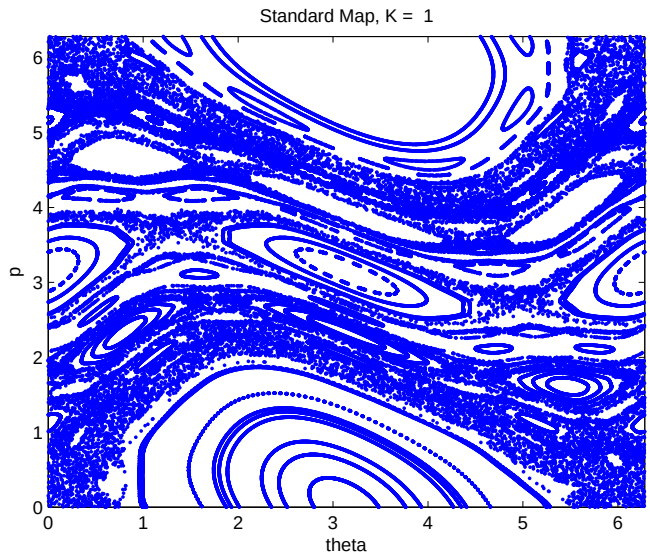

6.1: Illustration of the Destruction of Resonant Tori

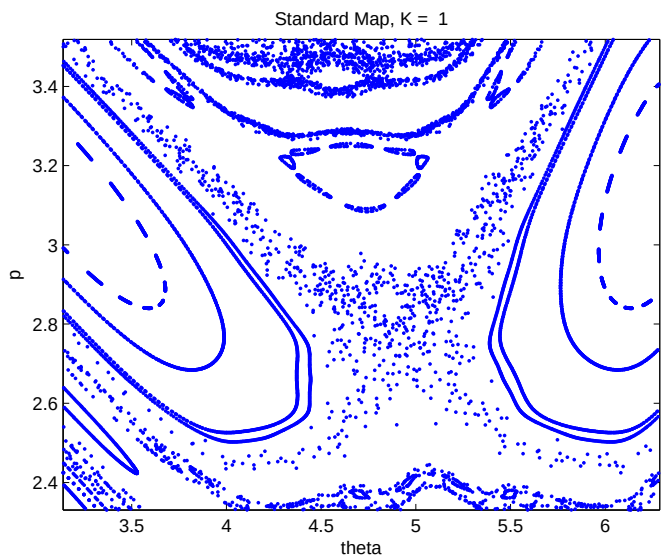

6.2: Detail of Elliptic, Hyperbolic and Chaotic Trajectories

Figure 6. The Standard Map

perturbations present, and it should ideally not experience resonances. Another reason for its lack of use might be from its nearly exclusive use by mathematicians in theoretical research. This may have created a quarantine-like effect on the theory, keeping it from being used by even the most adventurous of applied researchers. Even so, the literature is full of references to KAM theory. From the perspective of this work, they can be grouped into two categories: those dealing with artificial earth satellites and those that do not.

2.2.1 Efforts Not Related to Artificial Earth Satellites.

The vast majority of KAM-related research has nothing to do with artificial satellites. Most work has been done by mathematicians and physicists on theoretical problems ranging from galaxy formations to quantum mechanics. With that said, there are a large number of the papers pertaining to celestial mechanics. Arnold began the research with his 1963 work on the N-body problem [3]. Since the 1980's, one of the more prolific producers in the realm of celestial mechanics and KAM theory is Allesandra Celletti. While many are mathematical or general theoretical papers [18, 22], several are solely focused on celestial mechanics topics [16, 19, 20, 17]. Further, Celletti does a nice historical survey of KAM and the N-body problem in a 2006 paper [21]. Since most of this celestial mechanics work is analytic, it was not of much use for the research questions at hand. However, the work done in the field of galactic dynamics beginning in the early 1980's held much more value in context of this research due to their numerical approach to the problem of finding invariant tori.

In 1982, Binney and Spergel published a series of papers showing how to obtain non-classical integrals of the motion from the spectral lines of a set of numerically integrated orbits within galactic potentials [9, 10]. Since the spectral lines from

Fourier analysis suggested quasi-periodic motion, the integrals obtained were the action integrals discussed in the basic theory section. This analysis led them and others to conclude that N-dimensional galaxies modeled as collections of orbits could be described in phase space as an N-tori. Their papers discussed methods by which to obtain the actions such that the coordinates could be expressed as a Fourier series through numerical fitting methods of the torus. Later papers by Binney, Kumar and McGill [8, 72] mature and generalize this work, to include modeling a target potential with a known, toy potential and then mapping to the former via a generating function, thereby constructing the invariant tori. Kaasalainen and Binney further refine these methods in their subsequent work [58]. They overcome the problem of a toy potential being too dissimilar from its target potential by introducing point transformations into the process [57]. Kaasalainen then extended this work by considering chaotic orbits [56].

This research aimed to leverage the idea of Binney, Spergel, Kumar and McGill, but stopped short in creating a toy Hamiltonian. Rather, the torus was approximated through Fourier analysis and refined by estimation techniques, if necessary. Advanced techniques in Fourier analysis have been developed by Laskar, Wodnar and Gomez [66, 67, 41, 103]. Laskar developed a method called the Numerical Analysis of the Fundamental Frequency (NAFF). Conceptually, it is similar to that of common Fourier analysis, however it is much more accurate. Since the angle coordinates vary linearly in time as Ωt on a torus, accuracy in the approximation of the fundamental frequencies, Ω, is of the utmost importance. Laskar shows that the NAFF method converges to solutions with accuracies in the basis frequencies on the order of $\frac{1}{T^4}$, where T is the half of the sampling period. This is in contrast to the accuracy of standard fast Fourier transform techniques of $\frac{1}{T}$. It must be noted that Laskar uses a Hanning window filter of:

$$\chi_p\left(\frac{t}{T}\right) = \frac{2^p(p!)^2}{(2p)!}\left(1 + cos\left(\pi\frac{t}{T}\right)\right)^p, \tag{20}$$

where p can be loosely thought of as a level of precision parameter. As p is increased, so does the level of accuracy in the frequency estimates of quasi-periodic systems. Laskar's second paper shows that for regular motion, values of 3 and 5 seem to be the cut-off for increased precision of the NAFF algorithm. Gomez also used the Hanning window and offered a complementary method in characterizing quasi-periodic motion by using the Discrete Fourier Transform (DFT) [41]. His approach uses a preliminary method to find the basis frequencies (Laskar or otherwise) and then forces the equality between the DFT of the actual quasi-periodic oscillation and its approximation.

While the Hanning window is an overall good filter for determining both frequency and amplitude of a periodic signal, other filters are better in determining frequency or amplitude by themselves. In light of the work of Harris [47] and others in the study of harmonic analysis [52, 48], this research considered using different window functions, and possibly even separate windows for the amplitude and frequency estimates to increase accuracy. This idea of using various window functions to achieve different results has also been investigated in the field of quantum mechanics. Palma and Echave discuss several Einstein-Brilloiun-Keller Fast Fourier transform (EBK-FFT) methods that have used one or more windows in estimating the frequencies, coordinates, momentas, and semi-classical eigenvalues of multidimensional systems [85]. While Palma and Echave did not use windows in their work, their use of analytical Fourier transforms to estimate the Fourier series coefficients and frequencies shows potential promise for detecting and quantifying peaks in the modulus of the Fourier transform where the methods of Laskar and others may encounter problems.

Laskar methods are also mentioned in work by Guzzo and Morbidelli on Nekhoroshev's theorem [45, 46, 77]. However, they do not build the torus explicitly, rather

they just show effective stability of the periodic system. This was an important result to this research as an assumed torus may be the best option for satellite operations, especially if absolute stability within the desired operating regime is not provable or attainable. Analysis using methods like theirs on quasi-periodic systems may be necessary to determine the maximum useful time period for the nearly invariant tori assumed.

2.2.2 Previous and Current Artificial Satellite Research.

Very little has been done with KAM theory as it applies to orbiting artificial satellites. In fact, not until the recent work done and overseen by Wiesel [99, 100, 101, 102] was any research found to be directly applicable or even related to this proposed research. For example, Markeev and Bardin [70] used KAM theory to study the oscillatory rigid body motion of a rotating satellite in a circular orbit about a planet. Others mention KAM theory in the study of the restricted three-body problem and other well-known but restrictive problems, but they do not explicitly use it [93]. Palacian produced work regarding orbiting earth satellites, but he took an analytical approach to KAM theory as opposed to the numerical approach of this research. His research took a very restrictive look at the problem of a low-orbiting satellite about an earth-like planet with an inhomogeneous gravitational field [84]. The problem is restrictive in that it is assumed the satellite was in low orbit, the Keplerian term was dominant, and the system Hamiltonian only included zonal and tesseral harmonics up to the second order. Even so, he did show the existence of invariant tori for the three-degree-of-freedom Hamiltonian system by using a special form of the KAM theorem. Steichen and Giorgilli [94] discuss J2 effects on the long-term stability of artificial satellites about the earth. Their theoretical research neglects several key conservative and non-conservative perturbations, especially in light of GPS orbits,

but nonetheless they show a practical use of Nekhoroshev's theorem. Specifically, they show long-term stability of artificial satellite earth orbits.

As mentioned previously, the only work done with direct applicability to this research is that done by Wiesel and those who did research under his supervision. In Wiesel's first paper [99], he shows through numerical analysis similar to Laskar's methods that it appears earth orbits can be modeled as invariant KAM tori and he details an analytical method to estimate the three fundamental frequencies of earth-orbit KAM tori. His later work demonstrates different torus construction algorithms [100] as well as linearized solutions about a reference KAM torus [101]. From his initial work, three master's theses by Craft, Little and Derbis were spawned. Craft focused on long-term behavior on a torus in hopes that the torus concept could be used for orbital formation flight [26]. His results showed that while formations experience oscillatory relative motion, the drift between them is very small, especially if the formations are tight. Drift rates were on the order of nanometers per second for constellations with separation distances on the order of a kilometer. Little's research was very similar to this proposed research in that it attempted to fit KAM tori to the orbits of real-world earth-orbiting satellites, the NASA satellites Jason and GRACE[2]. The results for Jason and GRACE were promising as independent frequencies were found and accuracy in orbital predictions were on the order of one kilometer after two weeks. Further refinement in the algorithms should extend the usability of the fitted torus and lower the prediction errors to more acceptable levels for more sensitive applications. The work done by Derbis is the most relevant work to this author's research.

Derbis attempted to model GPS orbits as KAM tori, however, she was not completely successful [31]. Her efforts successfully identified two fundamental frequencies

[2]Jason and GRACE are two Low Earth Orbit earth observation programs managed by NASA. Both programs use low-earth orbits and have low eccentricities.

within the spectral content revealed by a modified Laskar approach, however she did not identify the third. Derbis set up her satellite dynamics model within the Earth Centered Rotating (ECR) frame per Wiesel's first KAM tori paper [99]. Thus, she expected to find the three fundamental frequencies to be the anomalistic frequency, an earth rotation/nodal regression rate combo frequency, and the apsidal regression rate. Unfortunately, analysis only revealed the first two frequencies. One reason for this may be that she might have unknowingly been looking for the wrong frequency. It is believed by this researcher that the third frequency may possibly be the long-frequency created by the resonance condition in the GPS orbital regime and not the apsidal regression rate. Recall that a resonant perturbation will cause a frequency to be destroyed, and if the phase space motion lies near a newly created tori within the phase space, this frequency will be replaced by a librational-type frequency around the resonance. It is believed that this frequency has been mentioned in unrelated research by Hugentobler et al to have a period on the order of eight years or more [51] and will be discussed shortly in the GPS resonance section.

The first aim of this research was to confirm Derbis' initial findings. Then, an orbital torus for a GPS orbit was to be fit to precision GPS ephemeris and its goodness of fit evaluated. Subsequent efforts were to involve evaluating orbital predictions for numerous GPS satellites by first ignoring the small, long-frequency motion and then comparing the orbital estimate to real-world data collections. Obviously, the former effort does not have any guarantee for useful results; however, it was believed that the long frequency was slow enough such that it was negligible on time scales of interest in this problem. In a best-case scenario, it was hoped that accurate orbital predictions could be made on time periods that were much longer than current prediction windows of 4 or 6 hours used by GPS. However, complications were encountered during research which limited the investigation of these ideas. If these obstacles can be overcome,

this type of analysis may lead to study into alternative GPS orbital regimes and constellation designs. Chapter III will expound in further detail what results were attained with GPS data and what conclusions that could be drawn from the research accomplished.

2.3 GPS Resonance

As the previous sections have shown, perturbations on resonant tori within the Medium Earth Orbit (MEO) region have negative consequences for strict interpretations of KAM theory as it pertains to GPS. It also does so for current, standard GPS operations. Recall from Section 1.2.4 that each satellite requires periodic station-keeping to maintain its specified GLAN. This maneuver requirement is a direct result of operating in a semi-synchronous orbital regime, and it has been studied extensively over the years.

2.3.1 GPS Constellation History.

GPS orbits were selected to reside within the MEO belt, and precisely speaking, each GPS orbit is designed to have a semi-major axis of 26,560.377 km with and eccentricity of no more than .02 [59]. The MEO belt has become a common orbital regime to place navigational systems (i.e. Galileo, GLONASS) due to the nearly repeatable groundtracks produced by its orbital altitudes. This repeatable motion is needed to maintain predictable, repeatable and favorable DOPs. However, GPS orbits are different than other navigational systems in that they are placed in a deep 2:1 resonance with the earth's geopotential. Considering the resonant perturbations experienced at this orbital location, an obvious question from a celestial mechanician's perspective is why would one do that to themselves? The answer is quite simple. The GPS developers were more focused on system demonstration and validation than

the subtleties of resonances and the long-term issues they may present. Considering the negative commentaries in the GPS literature regarding this now well-understood resonance effect on GPS satellites, for example those found by Green et al, Massatt, Píriz, and de Moraes [43, 71, 89, 75, 92], the constellation designers would probably raise/lower the constellation slightly such that the resonance effect was eliminated, or at least reduced, if they had the chance to redesign the constellation. Regardless, the point of placing the GPS satellites precisely at the 2:1 resonance point was due to the DoD's desire to have *exactly* repeating groundtracks such that desirable and repeatable satellite geometry over the US Army's Yuma Proving Grounds in Arizona, as well as certain parts of the Atlantic for the US Navy, was obtained for testing and validation purposes [43, 71]. During the 1980's when the initial test constellation of Block I satellites were being launched, this approach worked well and allowed for continual tweaks and analysis to be performed on the system at large (as well as user equipment) [2]. Of course, upon FOC, the GPS community was left with an undesired (yet free) side effect of the deep 2:1 resonance. A simple illustration of this resonance effect can be explained by an afternoon in your backyard with your child. Just as a very small, regularly timed push of your child on a swing will result in great increases in the amplitude of their swing height (and terror) over time, a resonant perturbation affects the size of the semi-major axis of a GPS orbit (and workload of the GPS analysts). Píriz et al show in their paper that over time, resonance effects cause secular, nonlinear drift in the semi-major axis, which obviously also affects the eccentricity. These changes translate into coverage problems (i.e. degraded PDOP). The plot in Figure 7 shows the projected effects on worldwide vertical accuracy within the GPS system if the GPS satellites were not maintained within their assigned GLANs for two contiguous years [89]. While the resonant geopotential effects can and are mitigated by periodic maneuvers (every 6 to 18 months depending on how close

each satellite is to each of the four equilibrium points within the resonant regime), these maneuvers cause outages in mission service until the satellite can be moved and its orbit redefined. In the past, this took as many as 3 days, but currently it can be done within a day. A single satellite down for such a small period may not seem significant, but one satellite outage can nontrivially affect PDOP. Further, the manpower required to support such maneuvers are costly and there is always a risk of on-orbit failure due to mishap [13]. Regardless, as better performance is required (i.e. possibly done though lower PDOP values from tighter GLAN tolerances), the frequency of maneuvers may increase such that even a small outage is amplified by a large constellation [43].

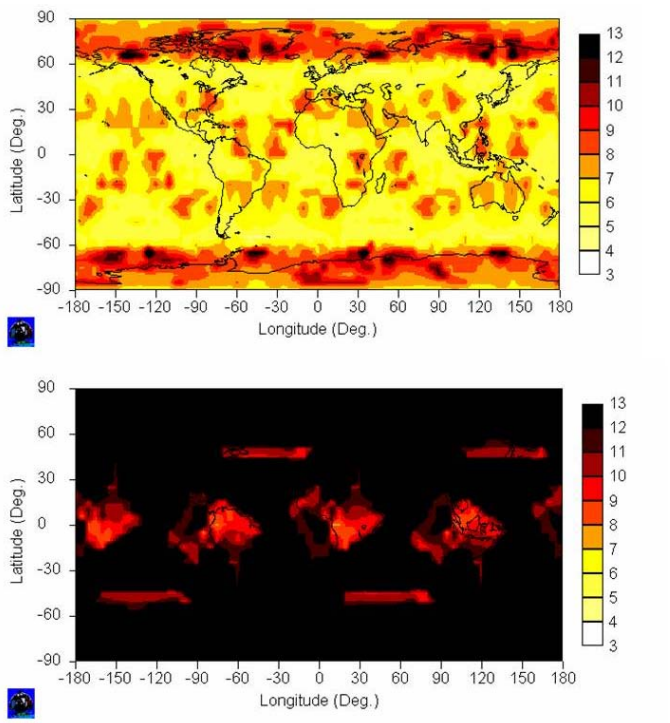

Figure 7. Vertical Accuracy Degradation (in meters) of GPS-like Constellation after 2-years w/o Maneuvering [89]

2.3.2 GPS Resonance-related Studies.

The resonance effect on GPS has been studied by many authors. In the previous section, several papers regarding the effects on coverage were briefly introduced. However, this is only a subgroup of the overall analysis. Since the disposal strategy of the GPS program is to boost the decommissioned satellites into higher parking orbits until their fuel tanks are spent, some authors have extensively studied the long-term effects of the MEO perturbations, to include the resonance effect, on disposal orbits [23, 24, 39]. Additionally, others have investigated station-keeping schemes for GPS-like orbits, albeit with higher eccentricity [35, 36]. From an analytical and non-operational perspective, others investigated GPS orbit sensitivity to the resonant geopotential effects [91, 54, 51]. As alluded to earlier, one author in particular (Hugentobler) appears to have quantified a long-period oscillation at 8 years or more [51]. Regardless of research motivation, the common idea in all of this work is to devise ways to deal with the resonance. Due to the fundamental nature of KAM tori, this research shows that putting all satellites on a single orbital torus may eliminates, or at least significantly minimizes, the need for maneuvers. However, this idea may require moving the constellation out of the resonant regime. Whether or not the orbital altitude needs to change to accommodate this one-torus concept, the satellites will still drift relative to each other and the net effect of this drift on PDOP will have to be studied.

2.4 Possible Effects of KAM Theory on GPS

KAM theory has the potential to affect GPS in two ways. First, it should lower the amount of error in the pseudoranges. This will explicitly reduce the error in any derived position solution. Secondly and probably most importantly, KAM theory should allow for longer use of ephemerides due to the nature of the KAM solution.

This has the potential of decreasing operations tempo within the GPS MCS.

In a perfect world, GPS solutions would have no error. However, errors due to the receiver clock, the onboard satellite clock, tropospheric and ionospheric delays, receiver noise, multipath, and miscellaneous small-order noises always creep into the navigation solution [90]. All error sources related to the user segment are commonly gathered together and called the User Equipment Error (UEE) while all error sources related to the space and control segments are gathered together and called the User Range Error (URE). Pictorially, this is represented in Figure 8 [64]. The root square sum of UEE and URE is known as the User Equivalent Range Error (UERE). Thus, UERE becomes:

$$UERE = \sqrt{(URE)^2 + (UEE)^2}. \tag{21}$$

A typical UERE budget can be found in Figure 9 [80], however the UEE portion is notional as user equipment performance varies. By far, the largest error source in the GPS UERE budget is due to environmental factors. After those, the next largest error source is due mostly to the atomic clocks onboard each spacecraft. That leaves ephemeris errors, which this work is primarily concerned with, and other miscellaneous errors as the smallest error sources remaining. Consequently, any gain provided by the KAM theorem will be overshadowed by the shortcomings of the onboard atomic clocks and propagation issues. While each new block of GPS satellites shows increased clock stability, improvements are still many years from allowing clock performance errors be considered negligible [83].

To qualitatively understand what gains may be achievable by applying KAM theory to GPS, let us look at a rough, notional analysis of reducing ephemeris errors in the GPS UERE budget found in Figure 9. First, assume an invariant torus can be found for each GPS satellite. To make comparisons simple, let normal GPS operations be maintained (i.e. a daily navigation upload), but assume each torus is

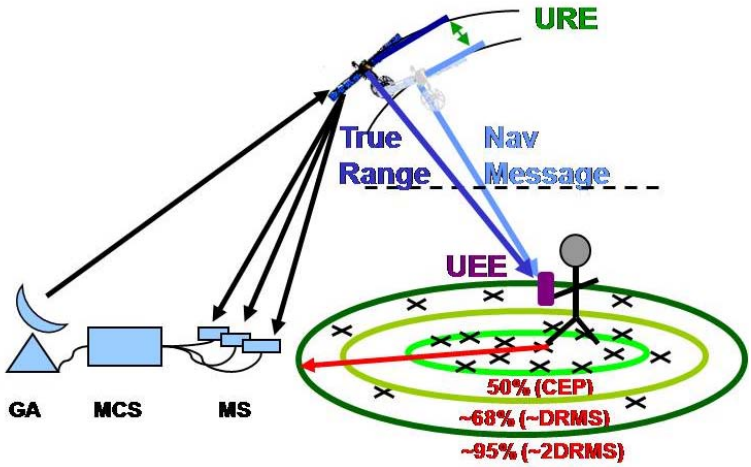

Figure 8. Macroscopic GPS Error Components [64]

Segment	Error Source	UERE Contribution (95%) (meters)		
		Zero AOD	Max. AOD in Normal Operation	14.5 Day AOD
Space	Clock Stability	0.0	8.9	257
	Group Delay Stability	3.1	3.1	3.1
	Diff'l Group Delay Stability	0.0	0.0	0.0
	Satellite Acceleration Uncertainty	0.0	2.0	204
	Other Space Segment Errors	1.0	1.0	1.0
Control	Clock/Ephemeris Estimation	2.0	2.0	2.0
	Clock/Ephemeris Prediction	0.0	6.7	206
	Clock/Ephemeris Curve Fit	0.8	0.8	1.2
	Iono Delay Model Terms	9.8-19.6	9.8-19.6	9.8-19.6
	Group Delay Time Correction	4.5	4.5	4.5
	Other Control Segment Errors	1.0	1.0	1.0
User	Ionospheric Delay Compensation	N/A	N/A	N/A
	Tropospheric Delay Compensation	3.9	3.9	3.9
	Receiver Noise and Resolution	2.9	2.9	2.9
	Multipath	2.4	2.4	2.4
	Other User Segment Errors	1.0	1.0	1.0
95% System UERE (SPS)		12.7-21.2	17.0-24.1	388

Figure 9. L1 Single-Frequency C/A-Code UERE Budget [80]

good for much longer than one day. In a best case scenario, application of KAM theory would effectively drive the Satellite Acceleration Uncertainty within the Space Segment errors to zero. It would also reduce Clock/Ephemeris Estimation, Clock-/Ephemeris Prediction and Clock/Ephemeris Curve Fit errors within the Control Segment portion of the UERE budget. Appendix C shows a notional calculation of a new UERE under the assumptions just presented. The results are summarized in Table 1. According to this crude approximation, the potential decrease of a notional GPS UERE may be as much as 2.4 percent under a daily upload scenario. If the interval of upload is moved to 14.5 days, the decrease in UERE is nearly 18 percent when compared to current DoD specification. As it can be clearly seen, the advantage of applying KAM theory is very evident as the time since ephemeris epoch increases (assuming the validity of the torus is much greater than the time interval in question). Of course, this is highly hypothetical and the actual performance increase may be not as much. Additionally, UERE budgets are the minimum standard advertised by the DoD. Thus, improvement over *actual* GPS performance metrics may be less. Regardless, it is a notable improvement nonetheless.

Table 1. Notional Decrease in UERE by using Orbital Tori (Daily Upload Scenario)

Error (meters)	Two Body GPS Model (Max AOD)	Notional KAM Tori GPS Model
URE	16.14	15.72
UEE	5.51	5.51
UERE	17.06	16.66

The best effect on GPS, however may be found at the operational level in the form of reduction in operations tempo. Currently, GPS satellites are uploaded at least daily with navigation data corrections. If a KAM tori can be found to approximate a GPS satellite orbit, the satellite would only need to be uploaded on the order of the validity of this torus (as opposed to the daily assumption made above), which may be on the order of weeks, months, or longer. Further, if all satellites within each plane can be

placed on the same torus, then the need to maneuver may disappear. This latter result depends however on how PDOP changes, which is beyond the scope of this research.

2.5 Summary

KAM theory is well studied, but it has not been commonly applied to real-world problems, especially as it pertains to earth-orbiting satellites. While prior research on modeling artificial satellite orbits with KAM tori is extremely limited, preliminary results are promising. The results of similar numerical KAM tori fitting efforts in galactic dynamics and other genres have yielded a set of tools that are useful in numerically finding invariant tori and serve as a stepping stone for methods to find orbital tori for earth satellites. While the earth-moon system has not been conducive to finding KAM tori through analytical means, they still may be present, as evidenced by numerical research from Wiesel. Regardless, the guarantee of perpetual stability assured by KAM theory may not be necessary as research using Nekhoroshev's theorem shows that effective stability may be more than sufficient when lifespans and mission parameters of operational satellites are taken into consideration. Finally, based on error analysis of GPS pseudoranges, the KAM theorem should be able to be applied such that it will not only reduce pseudorange errors but also reduce the operational tempo at the 2SOPS.

III. GPS Torus Construction from High-Precision Data

One of the terminal objectives of the numerical work within this research was to accurately reproduce a finite time history of real-world, high-precision data taken from an assumed quasi-periodic oscillation (i.e. a GPS satellite's orbit) by means of an N-tuple Fourier series representation of the said quasi-periodic oscillation, should it exist. Ideally, the Fourier series would allow the compression of the sampled data to a set of Fourier parameters that could be used for precision orbital prediction on a time scale longer than the time interval sampled or at least longer than the short prediction periods used currently for GPS operations. Thus, the desired Fourier series was of the form [100]:

$$\mathbf{q}(t) = \sum_{\mathbf{j}} \left\{ C_{\mathbf{j}} \cos(\mathbf{j} \cdot \mathbf{\Omega} t) + S_{\mathbf{j}} \sin(\mathbf{j} \cdot \mathbf{\Omega} t) \right\}, \tag{22}$$

where the multiple index summation vector, $\mathbf{j}^T = (j_1, j_2, \ldots, j_N)$, is dotted with the basis frequency set, $\mathbf{\Omega}$, and is expanded out to any arbitrary integer limit in each element according to the vector:

$$\mathbf{M} = (index\ limit_{j_1},\ index\ limit_{j_2}, \ldots,\ index\ limit_{j_N}) \tag{23}$$

in each axis, $\Omega^T = (\Omega_1, \Omega_2, \ldots, \Omega_N)$ is the basis frequency set, N is the dimension of the basis set, and $\mathbf{q}(t)$ is the time history of the reconstructed sampled position data. To be clear, the summation vector $\mathbf{j}$ must be chosen with care as to avoid problems when reconstructing the time domain data from the final estimate of the Fourier series due to symmetrical trigonometric properties (i.e. avoid problems due to $\cos(x) = \cos(-x)$, etc). Without taking these into account, the set of frequency combinations obtained would not be linearly independent and any decomposition/reconstruction method would undoubtedly use portions of the signal more than once while believing

it is not. The result is usually very large errors in the fit of the torus. Wiesel points this out [99], and he shows that combinations of the basis frequencies must be chosen such that the summation vector $\mathbf{j}$ have only positive values in the first non-zero index. For example, if $\mathbf{j}$ for two basis frequencies is summed over all integer combinations through $M = 1$ in both basis frequencies, then the summation index list would be:

$$\begin{aligned} \mathbf{j} &= j_{0,0},\ j_{0,1},\ j_{1,-1},\ j_{1,0},\ j_{1,1} \\ &= (0,0), (0,1), (1,-1), (1,0), (1,1). \end{aligned} \tag{24}$$

From the Fourier series representation at Equation 22, the coordinates and momenta can be backed out for orbit re-creation, prediction and other related orbital mechanics efforts. Until a torus can be constructed directly from the equations of motion for the unrestricted orbital problem at hand, one must resort to trying to detect the torus from a sampled set of orbital position data. This has been done with the results of numerical integration [99, 26] and high-precision, real-world data [69]. This chapter details efforts taken to construct a torus from the latter for the GPS constellation, and in particular, using high-precision, fitted data from the International Global Navigation Satellite Systems Service (IGS). This chapter will introduce the relevant theory necessary for this effort, address how the theory was implemented and adapted for this specific research problem, and highlight key observations and conclusions.

As alluded to previously, the GPS orbital regime proved to be a most difficult candidate for orbital tori construction efforts using trajectory following spectral methods. Difficulties were expected, but they proved even more arduous than anticipated. Consequently, several methods were developed, each with their own varying levels of success. It was hoped that precision-level fits (i.e. those equal to or better than current GPS operational methods) could be obtained for orbital timespans much longer than

the current day-long (or less) intervals presently used. However, this result was not realizable due to the competing desires of high accuracy and keeping data timespans, not to mention algorithm complexity, palatable to operational users. Table 2 summarizes the spectral methods employed for GPS orbital tori construction efforts, to include key issues encountered and results obtained. The methods from Chapter IV that were applied on low earth orbits are also listed for completeness; this summary will be presented once again in Chapter IV.

Table 2. Summary of Trajectory Following Spectral Methods

Orbit Type	Type of Data	Methods Applied	Issues	Key Results
MEO	Observed	3-Freq, Modifed NAFF	Near-commensurability, Small Ω_3, Unmodeled perturbations	Excessively large error
MEO	Observed	2-Freq, Modified NAFF	Near-commensurability, Small Ω_3, Unmodeled perturbations	Large error, Linear error growth $>$ 15 km per axis for 10-wk fit
MEO	Observed	1-Freq, Modified NAFF	Near-commensurability, Small Ω_3, Unmodeled perturbations	Large error (especially in Z-axis) Linear error growth $>$ 30 km per axis for 10-wk fit
MEO	Observed	NAFF	Near-commensurability, Small Ω_3	Error on the order of meters, however no underlying torus
LEO	Integrated	Frequency Cluster Decomp	Potential for small Ω_3 depending on orbital parameters	Error in fits range from a few meters to a few kilometers
LEO	Integrated	Least Squares Decomp	Potential for small Ω_3 depending on orbital parameters	Error in fits range from a few meters to a tens of kilometers, High sensitivity to "small" Ω_3
LEO	Integrated	Least Squares Decomp w/ Coefficient Correction by Simulated Annealing	Potential for small Ω_3 depending on orbital parameters	Corrects large errors due to "small" Ω_3. Error similar to that of cluster-based method

3.1 General Approach

Since the unknowns on the right hand side of Equation 22 must be identified, the general approach is fairly obvious. First, a highly accurate approximation of the basis frequencies must me made. Second, the Fourier series coefficients (i.e. the amplitude of the Fourier transform at each integer combination of the basis frequencies) must be determined. The coefficients are found directly from analysis of the Fourier transform of the data according to the following:

$$C_{(\mathbf{0},\mathbf{0},\ldots,\mathbf{0})^{\mathbf{N}}} = \Re\Phi(0), \tag{25}$$

$$C_{\mathbf{j}} = 2\Re\Phi(\Psi_{\mathbf{j}}),\ and \tag{26}$$

$$S_{\mathbf{j}} = -2\Im\Phi(\Psi_{\mathbf{j}}), \tag{27}$$

where $\Phi(\Psi_{\mathbf{j}})$ is the Fourier transform of the data at $\Psi_{\mathbf{j}}$, which is an integer multiple of the basis frequencies according to the summation vector $\mathbf{j}$. The real and imaginary portions of the Fourier transform are denoted by $\Re$ and $\Im$, respectively. At this point, all unknowns would be resolved and an initial torus could be constructed and its quality assessed. Of course, the latter assessment would be made by comparing the error in the fit of the torus. Since GPS is a high-precision system, the error in the fit would need to be on the order of meters over the given time span. If the torus fit is poor, it may be necessary to treat the initially obtained values of the frequencies and coefficients as preliminary estimates and then refine them through an iterative, fitting process. This research accomplished these aforementioned tasks by using Fourier analysis to obtain initial estimates of the basis frequencies, a Fourier analysis or least squares method to provide initial estimates of the Fourier coefficients, and a least squares algorithm to further refine the total Fourier series estimate.

3.2 High-Precision GPS Orbital Data

The GPS orbital data used for this research was obtained through the IGS [34]. The IGS is a collection of over 200 contributing organizations in more than 80 countries. The IGS has a global tracking network of more than 300 permanent GPS stations. These sites continuously send data to IGS Analysis Centers, where the precision IGS products are created. Data provided by the IGS is free of charge and is available

for download by anyone. The IGS provides various forms of GPS ephemerides and related products on the NASA server, from precision orbit fits to clock data. The most useful data for this work was found to be the final, precise orbit files. This product provides satellite positions in the ECEF frame at 15 minute intervals, according to GPS time, with advertised accuracies on the order of 2.5 centimeters rms in each axis. These files are updated weekly and provided in one day increments, based on the GPS week number. A MATLAB script was written to extract this daily data and store it in week-long files for analysis. As such, all GPS analysis in this work was done in week intervals. An example of the precision orbit files and their descriptions can be found an Appendix E.

It must be noted that the IGS is not the only provider of precision GPS orbits. In fact, within the GPS community there is some debate on which ephemerides are the most precise [83]. However, for the efforts within this work, it is believed that most of the precision arguments are not pertinent as long as the method for obtaining the position measurements, as well as the data's reference frame, is consistent. Trial simulations were accomplished with precision data from the National Geospatial Intelligence Agency [33] with little or no difference in results from those using the IGS products. Unfortunately, not much can be drawn from this result as the fits obtained from both sets of data were not of any considerable quality. When and if high-quality orbital torus estimates can be obtained for GPS, both data sources should be used and compared.

3.3 The GPS Spectral Content

Prior to applying Fourier analysis techniques to examine the spectral content of a GPS orbit, it was useful to perform preliminary theoretical calculations to determine a predicted set of basis frequencies. As introduced in Section 2.2.2, Wiesel has

introduced theoretical relationships to determine such a set [99], and they are provided here without any rigorous derivation. However, it is important to highlight that the basis frequencies for the geopotential-only solution to the earth orbiting problem number three and that they have clear physical interpretations within the earth-fixed frame. The three fundamental frequencies can be described as the anomalistic frequency, the earth's rotational frequency combined with the nodal regression rate, and the apsidal regression rate. The first frequency, the anomalistic frequency, is nearly the mean motion of the orbit itself. The components of the estimate of this frequency are the average angular frequency minus its rate of change due to the the average, linearized disturbing function [60]. In other words, it is approximately the resulting mean motion due to the secular effects of the geopotential considering only J2. Thus, this frequency can crudely be described as "setting up" the satellite's orbit as it describes the dominant rotational motion about the earth. Wiesel shows this frequency to be approximately:

$$\Omega_{1,J2} \approx \sqrt{\frac{\mu}{a^3}} \left\{ 1 - \frac{3J_2 R_\oplus^2}{2a^2(1-e^2)^{\frac{3}{2}}} \left(\frac{3}{2} \sin^2 i - 1 \right) \right\}. \tag{28}$$

This frequency is denoted with an extra subscript, J_2, to explicitly emphasize that this estimate of the $Omega_1$ frequency is based only on the J_2 component of the geopotential. The next frequency is how the previously established orbital motion precesses in the earth's rotating frame due to J2, hence it is a combination of the earth's rotational frequency and the nodal regression rate. Under the same assumption, this frequency is estimated to be:

$$\Omega_{2,J2} \approx \omega_\oplus + \frac{3\sqrt{\mu} J_2 R_\oplus^2}{2a^{\frac{7}{2}}(1-e^2)^2} \cos i. \tag{29}$$

Finally, the last of the basis frequencies was determined to be the description of

the motion introduced into the problem by the geopotential should the orbit not be perfectly circular. As such, it describes the rotation of the line of apsides, or the apsidal regression rate. Once again, this frequency is estimated to be:

$$\Omega_{3,J2} \approx -\frac{3\sqrt{\mu}J_2R_\oplus^2}{2a^{\frac{7}{2}}(1-e^2)^2}\left(\frac{5}{2}\sin^2 i - 2\right). \tag{30}$$

In each of these expressions, $R_\oplus$ is the radius of the earth, μ is the earth's gravitational parameter, J2 is the J2 term of the geopotential, $\omega_\oplus$ is the earth's rotation frequency, e is the orbital eccentricity, a is the orbital semi-major axis, and i is the orbital inclination. Thus, in hindsight, the basis set is essentially composed of frequencies that are already known due to perturbations about the earth [95], but under the paradigm of an KAM theory they have taken on a new, geometrical meaning: a torus. These three frequencies manifest in a repetitive and organized fashion within the spectral plot of orbital data. A notional representation of a small section of a typical orbital torus' Fourier transform is seen at Figure 10. The red spectral lines define a common pattern within the transform plot, a triplet structure. For orbits under the gravitational attraction of the full geopotential, this triple-line formation (to include the surrounding smaller, black lines) is copied over and over again in an asymptotically decreasing fashion along the frequency axis. While all three spectral lines of the triplet are found in each axis, the center line is most prominent in the Z-axis while the other two are strongest in the X and Y axes. This is due to rotating reference frame chosen.

If the torus is the fully degenerate case of the two-body problem, the spectral lines would be one copy of this triplet structure (i.e. only the red lines). In this instance, the middle line would be exactly the mean motion and the flanking lines would be the mean motion $\pm$ the rotation rate of the earth. The simple triplet pattern of the two-body problem takes on a much richer detailed look when under the influence

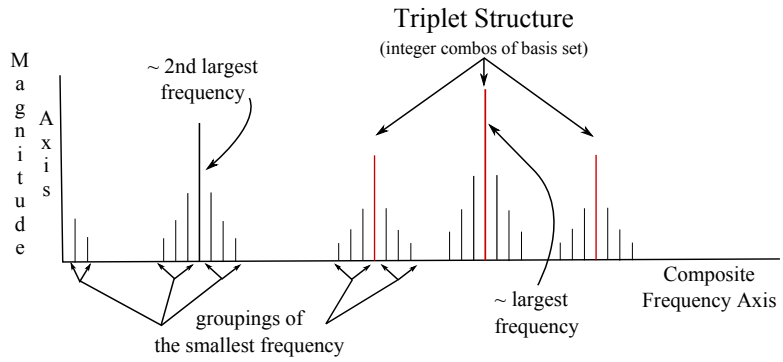

Figure 10. Notional Depiction of Orbital Torus Spectra

of the full geopotential (or high-order geopotential model for integrated data). The black spectral lines surrounding each of the red lines within the plot at Figure 10 is a crude representation of this detail. These flanking peaks surrounding each line of the main triplet structure are decaying echoes of the smallest basis frequency, which is approximately $\Omega_{3,J2}$. Unlike the simpler two-body scenario, the frequencies that compose the triplet structure while under the influence of the full geopotential are integer multiples of the entire basis set as opposed to just the mean motion and the earth's rotational frequency. Table 3 decomposes the main triplet into its individual basis frequency components under this scenario. For this example, the peaks in the main triplet structure have been numbered 1 through 3, from left to right. Both Wiesel and Craft comment on this structure in their work [102, 26]. In particular, Wiesel goes into considerable detail on the spectral lines of the Simplified General Perturbations Satellite Orbit Model 4 (SGP4) model and show how it correlates to its full orbital torus counterpart.

Table 3. Spectral Decomposition of Main Triplet

Triplet Line	$\lvert\Omega_1\rvert$	$\lvert\Omega_2\rvert$	$\lvert\Omega_3\rvert$
1	1	-1	-1
2	1	0	-1
3	1	1	-1

Using the aforementioned analytical expressions for the basis set at Equations 28,

29 and 30, Derbis determined the magnitude of the basis frequency estimates for GPS orbits to be [31]:

$$\Omega_{1,J2} = 2.0892e-02\frac{orbits}{15\ min} \tag{31}$$

$$\Omega_{2,J2} = 1.0446e-02\frac{orbits}{15\ min} \tag{32}$$

$$\Omega_{3,J2} = 6.3054e-07\frac{orbits}{15\ min}. \tag{33}$$

These were independently verified, however the units were renamed to $\frac{Radians}{GPS\ Epoch}$, where a *GPS Epoch* is defined here as one 15-minute interval between high-precision, GPS orbital position updates, or epochs. Thus, in this work, the analytical estimates of the basis frequencies were determined to be:

$$\Omega_{1,J2} = 0.131266446588158\frac{Rad}{GPS\ Epoch} \tag{34}$$

$$\Omega_{2,J2} = 0.065621984468624\frac{Rad}{GPS\ Epoch} \tag{35}$$

$$\Omega_{3,J2} = 3.964055611204401e-006\frac{Rad}{GPS\ Epoch}. \tag{36}$$

In the context of the larger real-world application of this orbital torus concept, these basis frequency estimates will need to be slightly altered due to other conservative perturbations, namely the moon and sun. While these effects are small, they must be accounted for in precision applications like GPS or for any application where the validity of the torus needs to be good for any significant period of time. These third-body frequencies can be found in many sources, but according to Vallado [95] these rates can be approximated by:

$$\Omega_{2,\ 3rd\ body} \approx -\frac{3\mu_{3rd\ body}(2+3e^2)[2-3\sin^2(i_{3rd\ body})]}{16r^3_{3rd\ body}n\sqrt{(}1-e^2)}\cos(i) \tag{37}$$

$$\Omega_{3,\ 3rd\ body} \approx \frac{3\mu_{3rd\ body}[2-3\sin^2(i_{3rd\ body})]}{16r^3_{3rd\ body}n\sqrt{(}1-e^2)}\left\{e^2+4-5\sin^2(i)\right\}. \tag{38}$$

For GPS, these values are approximately:

$$\begin{aligned}
\Omega_{2,\ Moon} &= -2.273770039222992e-007\frac{Rad}{GPS\ Epoch} && (39)\\
\Omega_{2,\ Sun} &= -8.013010695446439e-008\frac{Rad}{GPS\ Epoch} && (40)\\
\Omega_{3,\ Moon} &= 1.274501434191950e-007\frac{Rad}{GPS\ Epoch} && (41)\\
\Omega_{3,\ Sun} &= 4.505058717733763e-008\frac{Rad}{GPS\ Epoch}. && (42)\\
& && (43)
\end{aligned}$$

Thus, the final basis frequencies, minus any nonconservative perturbation effects, may be better estimated as:

$$\begin{aligned}
\Omega_1 &\approx \Omega_{1,J2} = 0.131266446588158\frac{Rad}{GPS\ Epoch} && (44)\\
\Omega_2 &\approx \Omega_{2,J2} - \Omega_{2,\ moon} - \Omega_{2,\ sun} = 0.065622291975734\frac{Rad}{GPS\ Epoch} && (45)\\
\Omega_3 &\approx \Omega_{3,J2} - \Omega_{3,\ moon} - \Omega_{3,\ sun} = 3.791554880607868e-006\frac{Rad}{GPS\ Epoch}. && (46)
\end{aligned}$$

To give an intuitive feel for what these values mean, it is useful to approximate the period of the oscillations from them. In this case, the theoretical approximate periods for Ω_1, Ω_2, and Ω_3 are .5 days, 1 day, and $16,500$ days (or nearly 45 years), respectively. However, recall from the previous chapter that due to the resonance

with the geopotential, which is apparent from the near commensurability of Ω_1 and Ω_2, the 45-year period associated with Ω_3 may have been replaced by a librational-type motion about the resonance. The period of this motion may be as low as 8 years [51]. Regardless, due to the long period of this smallest basis frequency, detection of it by means of Fourier analysis posed much more of a problem than the faster two. Similar to the consequences stemming from the Nyquist-Shannon sampling theorem is that it appears that in order to detect and reproduce the low-frequency content, a signal must be sampled for at least 2 periods. In the case of GPS's third basis frequency, this means a minimum of 16 years in a potentially best case scenario. More than likely, anywhere from 8 to 10 periods of this low frequency would need to be observed so that the NAFF-like algorithms used within this work could converge upon it with enough accuracy to be useful. Since even the oldest operational GPS satellites are no where near this old, let alone just two periods of the smallest frequency, Fourier analysis did not allow direct observation of this long-period motion. Even if satellites were of this age, the regular station-keeping GPS satellites endure would more than likely destroy any potential KAM torus upon which they reside[1]. Even though Fourier analysis techniques failed to reveal the smallest basis frequency, it was hoped that estimation algorithms could be used to make a parameter estimate with the available data. However, this also proved to be a false hope. As such, the torus construction methods employed within this work only used the two dominant, faster frequencies in the system, thereby ignoring the very small frequency motion. Initially, this was deemed acceptable since it was believed that sampling such a long period over a significantly smaller period (weeks versus years) would make the long-period frequency appear nearly static. While this latter statement is true if the frequencies

[1]Recall from KAM theory that perturbations should be small and conservative for the tori to remain after perturbation. Thruster maneuvers of any significance move a satellite off one torus and onto another, thus trajectory following methods require analysis *between* station-keeping maneuvers.

are looked at independently, spectral analysis showed that this long-period motion is not as easily ignored as hoped due to the way it weaves itself into the spectral signature of the torus. This will be discussed during the numerical results portions of this chapter.

With initial theoretical estimates of the basis frequencies calculated, Fourier analysis methods, as will be described in detail in Section 3.4, were used to approximate the actual spectral content of an on-orbit GPS satellite. For this effort, a GPS satellite known as GPS Satellite Vehicle Number (SVN) 47 (or Pseudorandom Noise (PRN) 22) was used. In fact, this satellite was analyzed almost exclusively in this research due to its special place within the GPS constellation. PRN 22 is located nearly on top of one of the two stable equilibrium points in the GPS orbital regime. Recall from Section 2.1.2 that resonant frequencies cause the phase space to effectively spawn pairs of stable and unstable equilibrium points, or nodes, under the presence of perturbations. PRN 22 was placed very near to one such stable equilibrium pair by chance since constellation design did not consider phase space behavior. As a consequence of its location, it experiences very little movement in its GLAN, which in turn means very few station-keeping maneuvers are required to maintain its position. As of September 2009, PRN 22 had not been moved since mid-2004. The plot in Figure 11 shows the spectral content of PRN 22 after processing 220 weeks of data (using a Hanning window of order 2). Original analysis examined the transform out to the Nyquist frequency, however only enough was included here to show the presence of the predicted basis frequencies from the preceding analytical expressions. PRN 22's spectral plot has clear similarities to the notional plot shown at Figure 10, however there are several key distinctions that should be made.

Like that in Figure 10, the beginnings of a clear pattern can be seen and the clean, delineated structure suggests a torus. The two X and Y peaks (in green and blue)

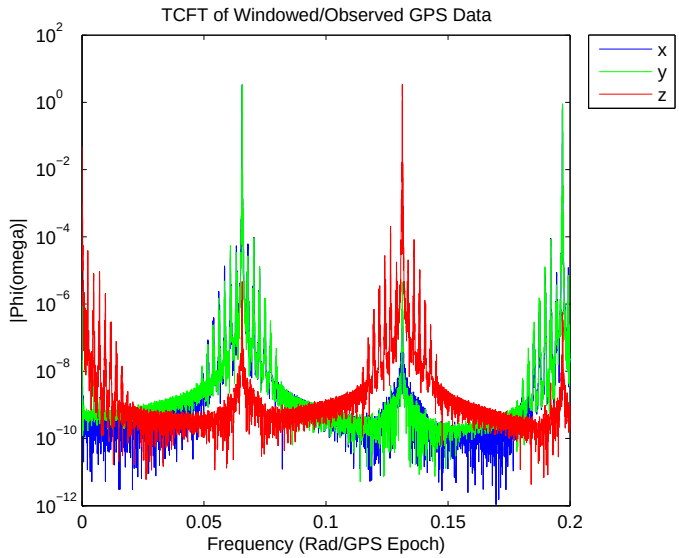

Figure 11. PRN22 Spectral Content (220weeks/p=2)

combined with the one large Z peak (in red) form one instance of the triplet structure discussed earlier. Due to the near commensurability of the two fastest frequencies, the largest of the transform peaks alternate at intervals of approximately Ω_2 between the z axis and x-y axes pair[2]. Furthermore, the near-commensurability is causing the primary triplet structure to actually hide portions of the other less prominent copies of the triplet structure as well as higher order harmonics of the two shorter-period oscillations. These peaks are literally hidden under the main lobe of the larger peaks. The only way to potentially overcome this effect is to increase the bounds of the orbit sample's time span. Unfortunately, this would require more data than is physically available.

Based on Figure 10, one may be inclined to assume the decaying peaks flanking each of the main triplet peaks are attributed to the smallest basis frequency. However, the long-period motion is so small that all of this detail is also shrouded by the primary lobes of the main triplet structure. Thus, after close examination of

[2]A clearer depiction of the alternating pattern within the Fourier transform can be seen Figure 17.1

these smaller flanking peaks, it was found that these peaks indicate the presence of third-body effects. They can be seen more clearly in Figure 12. The largest set of the smaller flanking peaks within the figure, which extend out nearly 8 visible harmonics from the largest peak, are attributable to the synodic and anomalistic lunar cycles of 29.530589 and 27.554551 days, respectively, or approximately 0.0022163 and 0.00237567 $\frac{Rad}{GPS\ Epoch}$. Hence, each flanking peak is separated by integer multiples of these lunar frequencies. Since the two are nearly commensurate, they do not separate into two distinguishable frequencies until a few harmonics out from the largest, central peak. The peaks surrounding the lunar harmonics (as well as the larger peaks in the triplet structure) are the harmonics associated with the earth's rotation about the sun. Similar to that of the lunar frequencies, the solar-cycle-induced peaks are separated by integer multiples of this nearly 365-day period, and in this plot, extend out for a few harmonics. Since the amount of data used in this spectral plot translates to just over 4 periods of the solar cycle, only a few barely defined harmonics of the solar frequency are visible.

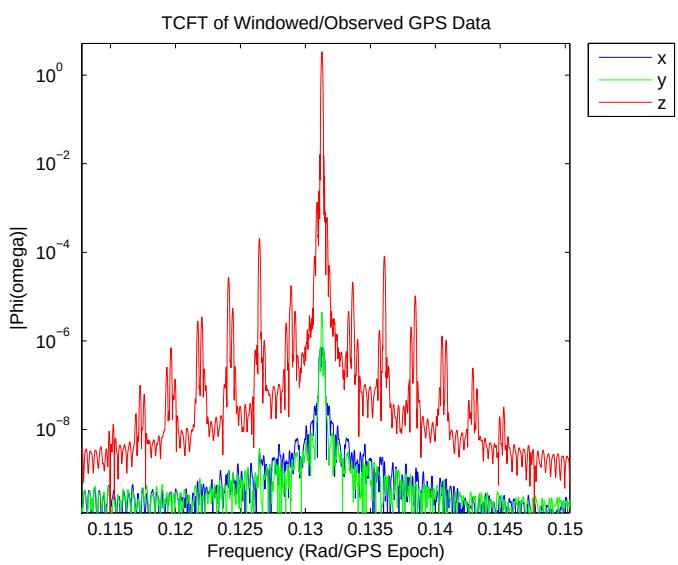

Figure 12. Evidence of 3rd Body Frequencies (PRN 22/220weeks/p=2)

This subtle appearance of the third body effects highlights a limitation in the tra-

jectory following methods. Without large amounts of data, much of the rich detail in the Fourier transform plot, especially that of small conservative influences which ultimately need characterized for precision applications, is either not detectable or poorly characterized. Should only weeks or months of data be taken, these low frequency effects will be missed. While some level of fit is still possible without incorporating them, its period of validity may be much shorter than a torus that does. This is where engineering judgement on how much data to use versus the goodness of fit is desired will need to be applied. Since the best possible fit with the longest period of usability will want to be achieved, the n-body effects will need to eventually be characterized and modeled via additional frequencies. This of course will require longer sampling times, which could conceivably reveal even more perturbations whose frequencies will need to be identified. Unfortunately, this makes the trajectory following method even more time-consuming and complex than it is already. However, until other methods are developed, this may be an unavoidable necessity, if the benefits of using a long-term orbital torus are desired. Previous orbital torus work using real-world data by Little [69] did not explicitly see such effects by third bodies since the orbital altitudes studied were nearly $15,000$ kilometers below that of GPS and the time spans used were much shorter. Thus, the third-body effects were dominated by the geopotential and air drag.

3.4 Fourier Analysis Methods

Initial GPS torus construction efforts concentrated solely on Fourier analysis methods in hopes they would suffice, thereby making fitting methods unnecessary. In keeping with the previously mentioned general approach, initial estimates of the system frequencies were first sought, followed by the coefficients. The basis frequencies were identified under the key assumptions that the motion was truly quasi-periodic

and that the non-degeneracy and diophantine conditions from KAM theory were met. Several recent approaches were reviewed, to include that of Gomez [41], Wodnar [103], Hunter [53] and Laskar [66, 67], but ultimately NAFF-like algorithms a la Laskar were chosen for MATLAB implementation despite potential lengthy processing times. Additionally, a NAFF-like approach was also used by Wiesel on characterizing artificial earth orbits as KAM tori with considerable success [99].

The NAFF approximates the truncated, continuous Fourier transform (TCFT) by scalar product, as opposed to using faster DFT methods, in order to minimize the effects of aliasing and leakage within the Nyquist interval [103]. When using a Hanning window of order one, the NAFF has been shown to converge upon the fundamental frequencies at a rate of $\frac{1}{T^4}$ for KAM problems instead of $\frac{1}{T}$ by standard Fourier transform methods, where T is half the sample interval [66, 67]. The NAFF approximates the quasi-periodic function by decomposing the transform according to the n-tuple Fourier Series of the form:

$$\mathbf{f}(t) = a_{(1,0,\ldots,0)^N} e^{i\Omega_1 t} + \sum_{k \in \mathbb{Z}^n - (1,0,\ldots,0)} a_k e^{i(k,\Omega)t};\ a_k \in \mathbb{C}, \tag{47}$$

or in the familiar equivalent real form which has been introduced previously

$$\mathbf{f}(t) = C_{(0,0,\ldots,0)^N} \cos(\Omega_0 t) + \sum_{\mathbf{j}} \left\{ C_{\mathbf{j}} \cos(\mathbf{j} \cdot \mathbf{\Omega} t) + S_{\mathbf{j}} \sin(\mathbf{j} \cdot \mathbf{\Omega} t) \right\}, \tag{48}$$

where the multiple summation vector $\mathbf{j}$ is defined as before, via a signal decomposition process. The decomposition process employed by Laskar, as well as a modified version of it, will be further discussed in Sections 3.4.2 and 3.4.1, respectively. However, looking closely at Equation 48, one can see that the only difference between it and the desired, final Fourier series approximation found at Equation 22 is some initial condition, $C_{(0,0,\ldots,0)^N}$, which can be found by evaluating the Fourier transform at zero.

Thus, the NAFF accomplishes the exact actions needed to decompose an orbit to an n-tuple Fourier series for torus reconstruction. In order to estimate the fundamental frequencies within this approximation at frequencies above zero, and every integer combination thereof, the NAFF finds the maximum amplitude of

$$\phi(\omega) = \langle \mathbf{f}(t), e^{i\omega t)} \rangle, \tag{49}$$

where the scalar product $\langle \mathbf{f}(t), \mathbf{g}(t) \rangle$ is defined by

$$\langle \mathbf{f}(t), \mathbf{g}(t) \rangle = \frac{1}{2T} \int_{-T}^{T} \mathbf{f}(t) \overline{\mathbf{g}}(t) \chi(t/T) dt, \tag{50}$$

and where $\chi(t)$ is a weight function which is positive, even function such that

$$\frac{1}{2} \int_{-1}^{1} \chi(t) dt = 1. \tag{51}$$

Recall the Hann (a.k.a. Hanning) window for Laskar's work as it was in Chapter II:

$$\chi_p \left(\frac{t}{T} \right) = \frac{2^p (p!)^2}{(2p)!} \left(1 + cos \left(\pi \frac{t}{T} \right) \right)^p. \tag{52}$$

The Hann window is used by Laskar to further reduce leakage effects in the Fourier transform. Leakage is the spreading the peak-of-interest's power into adjacent side lobes due to the use of sampled data whose length contains non-integer multiples of the basis frequencies. Windowing, as it is commonly called, is commonplace within the Digital Signal Processing (DSP) community to reduce leakage, so it is of no surprise this process was employed. Laskar's first NAFF paper postulated its assertions based on a Hann window of order 1. However, he does show in a subsequent paper that the order of the window, p, can take on integer value between 1 and 5 depending on the level of accuracy needed and the regularity of the motion. After $p = 5$ gains in convergence are greatly diminished. However, Craft [26] showed values of $p = 9$ or

more to lead to tight tori fits for low earth orbits. For this work, a Hanning window of $p = 2$ was used primarily. This is due to the fact that as p increases, so does the width of the main lobe. While this assists in frequency resolution and side lobe suppression, it does increase the opportunity of the main lobe shadowing any nearby peaks. This was also noticed by Wiesel [99] and Little [69] as well as commented on by Gomez [41].

Clearly, the NAFF is similar to common Fourier analysis methods with the distinctions noted above. Of course, instead of the familiar Fourier integral, the Fourier transform was calculated as a scalar product between the vectors of weighted sampled data values and $e^{i\omega t}$, with the desired number of frequency points ω depending on the level of frequency granularity desired in the output. Generally speaking, this research found it beneficial to use large values of frequency points (approximately 5000 for every integer frequency unit increment in the bandwidth of the signal being investigated), especially when investigating a data set for the first time. Too few points may obscure fine details in the spectral content, such as the cascading harmonics of the apsidal regression frequency about the two faster frequencies in the basis set. The strength in the NAFF algorithm lies in the fact that aliasing and leakage are thoroughly mitigated and that it converges much more quickly than standard methods. The penalties are time-consuming numerical evaluations and the potential to introduce errors during the approximation of the numerical integrals. Wodnar and Gomez assert that FFT methods can be used to mitigate these limitations. They argue that in the limit, the DFT and FFT are equivalent to that of the approximation of the continuous Fourier transform performed by Laskar, and further assert that Laskar's methods could be used to cue their own more efficient and potentially better algorithms. However, it is believed that Laskar-like methods are sufficient. Although, it is acknowledged that there are potential problems with interpolation schemes to

evaluate the Fourier transform integral. The numerical integrals approximated in this research were done via simple quadrature methods, specifically 3/8 and/or 1/3 Simpson's Rules, depending on the number of data samples to analyze. Thus, the error was quantified to be of third-order accuracy according to the following [25]:

$$E_a = -\frac{(b-a)^5}{180n^4}\overline{f}^{(4)}, \tag{53}$$

where a and b are the end points of the integration interval, n is the number of segments, and $\overline{f}^{(4)}$ is the average fourth derivative for the interval. It was assessed that this was sufficient. Regardless, the keys in implementing the NAFF algorithm are to sample fast enough to avoid aliasing effects, long enough to mitigate leakage, and to apply a window function of appropriate characteristics such that leakage is further minimized without affecting nearby frequency identification.

3.4.1 Modified Laskar Method.

The first algorithm used to estimate a GPS orbital torus followed the lead of Wiesel [99]. Wiesel's method is similar to the NAFF in most regards, however it cleverly avoids the cumbersome iterative, decomposition and subsequent basis set identification process by establishing a basis frequency set prior to any Fourier analysis efforts. The overall approach is to establish a theoretical basis frequency set, refine that estimate via the NAFF algorithm for those specific frequencies, and then determine the Fourier coefficients at each integer combination of the basis frequencies until the desired level of fit is achieved.

After estimating the basis frequencies from Equations 28 through 30, the maxima of the modulus of the Fourier transform of the orbital data at several prominent frequency combinations in each coordinate axis were found, and then an overall basis set for the torus was calculated through a least squares fit. Since the theoretical

frequencies are only estimates of the actual frequencies, the true basis frequencies exist where Equation 49 has maximum values. Each sought after frequency was found by searching for the maxima of the power of the signal, $\Phi(\omega)^2$, near each of the theoretical estimates of the basis frequency combinations in each coordinate through a Newton-Rhapson method, thus finding the frequency corresponding to the zero slope condition on the power curve. Once an initial basis set was calculated by the NAFF, the amplitudes of the Fourier transform of each desired integer combination of the basis frequencies were determined, being careful not to count frequencies more than once due to trigonometric identities. Since the spectral content of every orbital track is essentially unique, the number of coefficients required for a quality torus fit is also generally unique to the data set as well as the user's needs. Methods to find this number for a particular orbit are ad hoc. While this implies an iterative approach to find a proper fit, the use of an a priori basis set removes the cumbersome task of backing out the basis frequencies from a sorted list of frequencies and their corresponding coefficients after decomposition.

The success of Wiesel's method hinges on the validity of the assumption that the assumed basis frequencies are the only (or at least vastly dominant) frequencies in the data and that the frequency combinations are well-separated (i.e. fully resolvable from a spectral perspective). If the spectra within the Fourier transform are not well-separated, then the fit will be poor as information will be lost and/or possibly doubly accounted. This will be true regardless of whether or not the basis set is complete and converged upon sufficiently. Of course, the assumption that all frequencies were accounted for could be tested by performing an FFT of the residuals of the torus fit. If the fit is good, the FFT analysis should only show a noise-like pattern remaining. Should there be any additional, significant frequency content left, the FFT analysis should show peaks at the offending frequencies and their harmonics. Since capturing

all harmonics is impractical and sometimes unnecessary, the fit can be declared as sufficient as long as any organized, torus-like pattern is very weak in power (i.e. not having significant contribution to the signal) and/or the desired level of fit has been achieved.

Ultimately, this method did not achieve highly accurate orbital tori estimates for GPS orbits since the basis frequencies are nearly commensurate. Because the frequencies are near-integer multiples of each other, the harmonics of the basis set are mostly undistinguishable as they are commonly separated (spectrally) by only $10e-7\frac{Rads}{GPS\ Epoch}$ or less. As such, the lobes from nearby higher-power frequencies are completely covering contributions from lower power, higher-order harmonics, and upon trying to estimate the amplitudes of these higher-order frequency combinations, the amplitude of the dominant lower-order frequency combinations were obtained and used again. Thus, the error in fits of tori using high-order expansion in the basis set were on the order of thousands of kilometers. While efforts were taken to effectively sample faster (through interpolation) and longer, no reasonable amount of data could separate the peaks such that they were fully resolved. Even if the peaks could be partially resolved, the lobes are so close to each other that it is almost certain that the shoulders of the larger peaks would still impact determination of the nearby peak amplitudes since the larger peaks' shoulders would add to the amplitudes of the nearby peaks. Once again, another limitation of the trajectory following method was uncovered.

Permutations on Wiesel's method were attempted to see if relief from the near-commensurability could be obtained. The first attempt was to treat the two faster frequencies as if they merged, leaving only Ω_2 and Ω_3 as basis frequencies. However, since Ω_3 is very small, the long-period motion was treated as if it were static. Thus, 1-torus estimates only using Ω_2 were created. While the fits were much improved

over the original method since multiple sampling of amplitudes was not done, the two fastest frequencies were not commensurate enough such that treating them as a single, merged one was acceptable, especially in the z-axis. A sample of the results under a $\mathbf{M} = (10)$ expansion can be seen in Figure 13. Linear growth of the residuals in all axes of the torus fit is evident, especially in the Z-axis. This trend is consistent with all lengths of data samples used. The Z-axis is particularly sensitive for error, since Ω_1 has more power in this axis than it does in the X and Y axes. Since Ω_1 is assumed to have merged with Ω_2 in this method, any error from this assumption will show up in this axis the most. The linear growth suggests a mismatch in frequency identification, but equal or greater contributors to the error are more than likely the loss of higher-order harmonic information due to it being covered by the larger peaks as well as contributions from the moon. The lunar effects are possibly manifesting as the oscillatory envelope of the linear growth of the residuals. Should the other previously mentioned error sources be mitigated, it is believed the leftover lunar frequencies should create oscillatory residuals with a slower linear growth in the error.

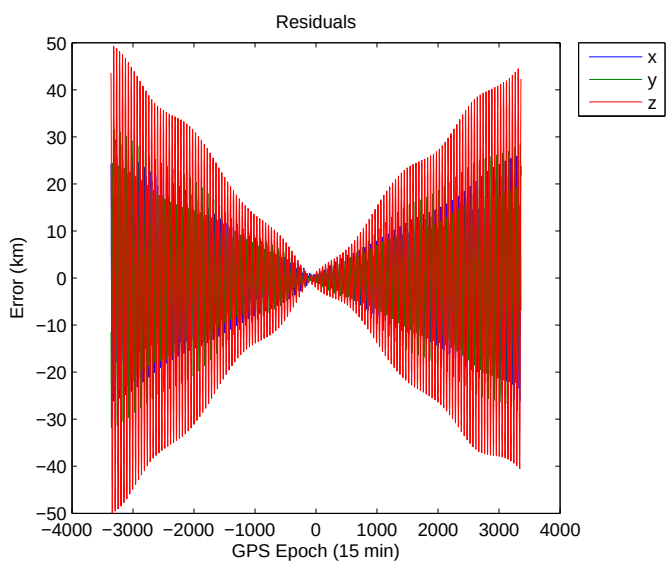

Figure 13. 1-Frequency, GPS Torus Fit (PRN22/10 weeks/p=2)

Another approach was to keep the basis frequencies independent yet only search

out very low-order harmonics to avoid over-sampling these lower-order peak amplitudes while trying capture higher-order (yet lower-power) peak information. Once again though, the third frequency was assumed to be static, thus 2-torus estimates were created. Figure 14 shows a sample of the results under a $\mathbf{M} = (10, 1)$ expansion. The Z-axis shows much improvement over the previous permutation of Wiesel's method since two frequencies were acknowledged, however the larger linear growth in error of the fit is still seen in the X and Y axis. As before, this can be attributed to a misidentification of the basis frequencies as well as effects from the moon and the lack of higher-order harmonic information. To illustrate the latter, the z-axis Fourier transform of the reconstructed torus was overlaid on that of the original data and it is shown in the plot at Figure 15.

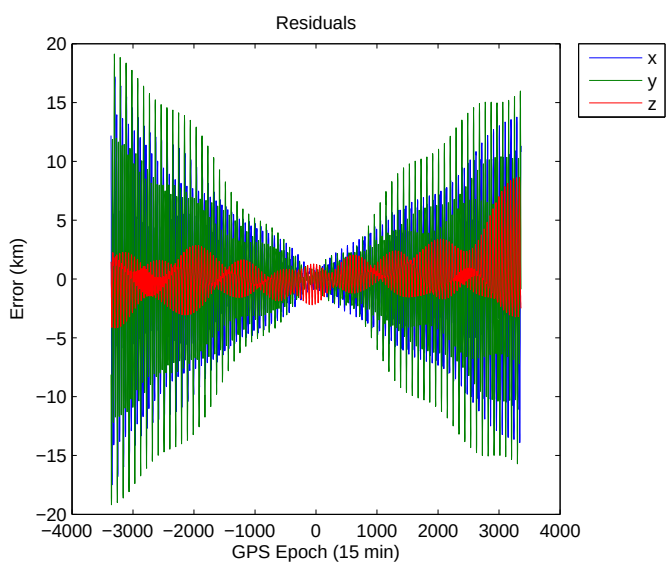

Figure 14. 2-Frequency, GPS Torus Fit (PRN22/10 weeks/p=2)

The green circles above the transform represent integer multiples of the basis frequencies selected for decomposition and analysis. Clearly the most visible, significant peaks are covered by the Fourier transform of the reconstructed orbital data, with exception of the lunar harmonics that started to appear. For a point of reference, peaks on the order of 10×10^{-10} on the magnitude axis correspond to contributions

within the error plots on the order of tens of centimeters or less. Thus, if the explicitly visible spectra in Figure 15 were the only frequency information present in the data, one would expect a better fit than what was attained since most are well-accounted for by the simple expansion of two basis frequencies. However, since the higher-order harmonics are literally covered by nearby peaks, they are not available for characterization and inclusion in the torus model. As highlighted previously, the only relief to this problem is to sample for longer periods until enough peaks emerge from the shadows of the larger peaks. Unfortunately, the longer the time period used, the more low-frequency effects (which are difficult to truly characterize) creep into the problem and the more impractical the method becomes for operational use. Hence, when fitting a torus, the goal should be to use a data sample that is long enough to achieve desirable fits, yet short enough to not invite slower frequency effects. This idea will be commented upon further in the next section.

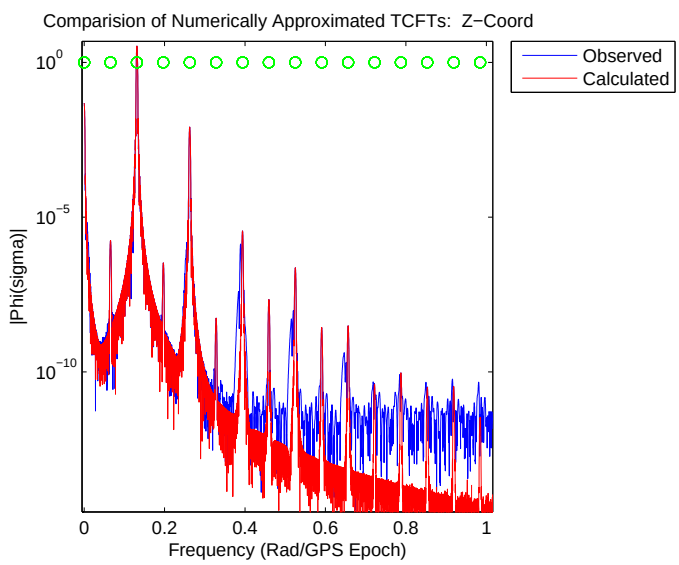

Figure 15. TCFT of 2-Frequency, GPS Torus Fit (PRN22/10 weeks/p=2)

3.4.2 Laskar Decomposition.

Since Wielsel's approach, and variations of it, did not fare well for GPS orbits, the next method used to detect a torus from precision orbital data was one that mirrored more closely that of Laskar. As such, no a priori basis set was assumed. The premise was to identify and decompose the prominent spectral peaks in decreasing order of size, and not by an orderly harmonic progression as done previously, such that each peak could be analyzed without being overly affected by larger, nearby peaks. This was motivated by the results seen in the plot at Figure 15. The assumption drawn from this plot was that if all visible peaks could be decomposed in decreasing order of magnitude, the fit would be improved since peak shoulder effects would be eased. It was also hoped that peaks that were only mostly covered would be revealed and thus available for analysis. Since no basis set would be assumed, this approach would also allow third body frequencies to be folded into the analysis much more easily. Unlike the faster frequencies in the basis set where the spectra associated with them is clean and systematically delineated, lunar frequency contributions appear sparsely within the transform due to the short time spans used thus far. As such, automated mechanization of third body frequency decomposition is difficult and must be treated almost in an ad hoc manner. Because of these factors, Laskar's NAFF decomposition process appeared superiorly suited for this effort.

The NAFF decomposes quasi-periodic signals by identifying the maximum amplitude of the windowed Fourier transform, finding its corresponding amplitude, subtracting the recently identified frequency content from the signal, and then repeating the process. The maximum amplitude of $\Phi(\omega)$ is determined exactly as done previously in Section 3.4.1. After determining the frequency and amplitude at the current iteration, the original signal is adjusted according to the following decomposition expression:

$$\mathbf{f}(t)_{k+1} = \mathbf{f}(t)_k - C_{\omega_k}\cos(\omega_k t) + S_{\omega_k}\sin(\omega_k t), \tag{54}$$

where k is the current iteration in the decomposition process and ω_k is the frequency corresponding to the k_{th} largest peak in transform, $\Phi(\omega)$. The process is repeated until the desired level of precision is reached. At that time, a survey of the decomposed peak frequencies must be accomplished to back out the fundamental frequencies as well as the torus itself. Unlike the method employed by Wiesel, this method can accommodate a fit even if the assumed basis set is a subset of the total number of basis frequencies. One simply needs to back out these frequencies based on the total number of frequencies picked up in the decomposition process. However, like Wiesel's method, success of the NAFF decomposition process also hinges on the validity of the assumption that the frequency combinations are spectrally well-separated.

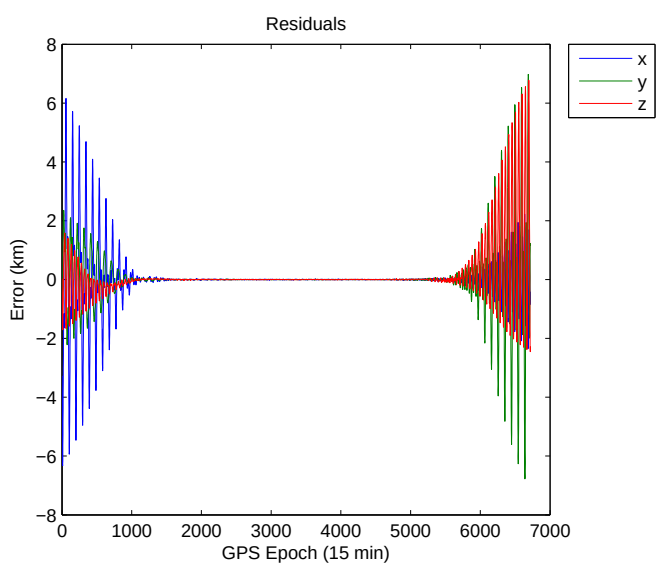

Figure 16. NAFF Torus Fit (PRN 22/10 weeks/p=5/221 coefs per axis)

One attempt of this method was accomplished with a 10-week sample of PRN22's orbital trajectory. It was analyzed using Laskar's decomposition method with a Hanning window of order $p = 5$. In all, 221 peaks were decomposed from each coordinate

axis to form estimates of the Fourier coefficients. The error of the fit can be seen at Figure 16. For most of the time interval, error is on the order of about 10 to 15 meters but rapid nonlinear growth is experienced near the edges of the time window. Other attempts were made on this data with coefficients reaching $1,000$ per axis and they show that as the number of coefficients increase, the error in the center of the fit decreases (less than 1 meter for $1,000$ coefficients). The magnitude of the rapid nonlinear growth also diminished and it did not visibly manifest until closer to the time window edges. However, the nonlinear growth was still very much evident. After inspection of the frequencies identified during these decomposition runs, it was noticed that even as the number of coefficients approached $1,000$, harmonics at and beyond the third harmonic of Ω_1 were still not being decomposed. Figures 17.1 and 17.2 demonstrate this; clearly the algorithm was only identifying peaks near the lower end of the frequency spectrum. These figures depict the original and post approximations of the TCFT for a 10-week, 221-coefficient GPS decomposition run. Notice how the left-most groups of frequency peaks have flattened while the remaining spectra is virtually untouched. Hence, the rapid nonlinear growth in the residuals can be attributed to the NAFF leaving pertinent portions of the sampled quasi-periodic function in the higher harmonics within the leftover signal. While one might infer from these figures that allowing the decomposition routine to process more frequencies and coefficients will produce a torus with meter-level error fit throughout the entire time window, this is not the case. Yes, the residuals would eventually flat line, but no appreciable, underlying geometrical object would be obtained.

Upon examination of the frequency lists after the decompositions, it was revealed that no clear pattern was present, as would be expected from that of a torus. Instead, what was found was an almost random list of frequencies centered around areas where integer combinations of the basis set were located. The algorithm appeared to have

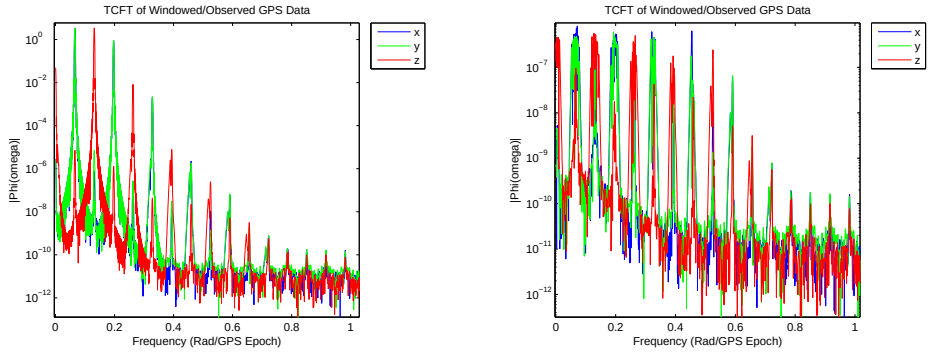

17.1: Prior to NAFF

17.2: After NAFF

Figure 17. Pre and Post NAFF TCFTs (PRN22/221 coefficients per axis)

sought out and identified numerous false peaks left over after legitimate peaks were removed, which in turn created additional false peaks and so on. This phenomenon is partly due to the fact that the spectra is not fully separated but also because the NAFF has not fully converged on the basis set with sufficient accuracy. The false peaks leftover after decomposition are evident in the plot at Figure 17.2 and are more clearly seen at Figure 18. Ideally, no residual peak would be left after decomposition, only the remaining portion of the Fourier transform curtain. However, due to the aforementioned issues, the result is a false, residual peak. This conclusion can be verified by a simple illustration with fabricated data somewhat similar to that of the real GPS data. 10-week and 200-week samples of data containing 7 frequency peaks created from 2 basis frequencies of $\Omega_1 = 0.7$ and $\Omega_2 = 0.361$ (a ratio of 1.94:1) were analyzed and decomposed by the NAFF decomposition process. The 10-week sample shows high residual peaks after extracting all seven frequencies and they can be seen at Figure 19. Figure 20 shows that while the 200-week simulation has less power in its residual peaks, they are still high enough to potentially cause confusion in the NAFF algorithm, if real peaks are below these false peaks. However, as noted previously, error in the fit on the order of centimeters can be expected from ignoring peaks, false or otherwise, at magnitudes of 10×10^{-10} in the Fourier transform of a GPS orbit.

While this simple example shows the issue is mitigated with a longer time span of data, the problem is dramatically more pronounced and difficult to resolve as the frequencies become more commensurate, like the two dominant GPS frequencies, and are more numerous. The behavior can still possibly be mitigated with longer periods of data (i.e. on the order of hundreds of years), but this solution is not helpful nor practical for satellite missions that only have a mission life of several years. As a result, this decomposition approach is also not an ideal candidate for GPS orbital tori construction either.

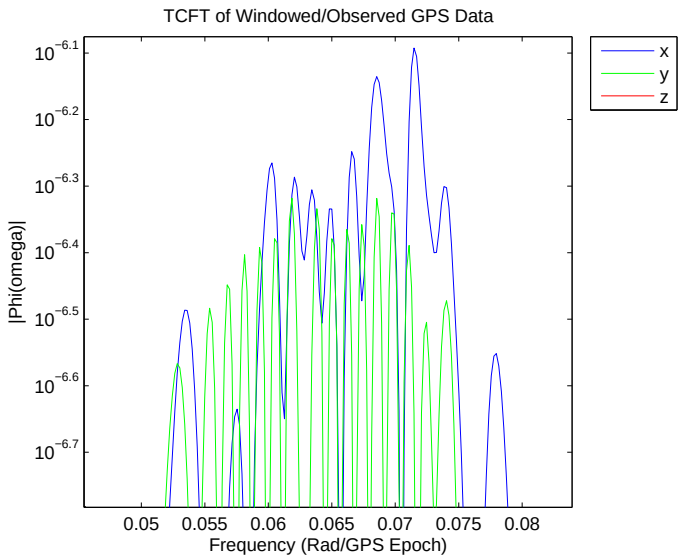

Figure 18. Zoom of TCFT after NAFF (PRN22/221 coefficients per axis)

3.4.3 Quick-Look Decomposition Trials with LAGEOS1.

Since efforts with the Laskar's decomposition process, and variations of it, struggled with GPS data, the data source was changed to see if other orbital regimes would allow more success. The Laser Geodynamics Satellites (LAGEOS) were selected due to their long-term study and data holdings. While most of the data is not in convenient form for the algorithms used in this research, some trial data currently being developed in the form of SP3 files was made available for use by NASA [86]. The

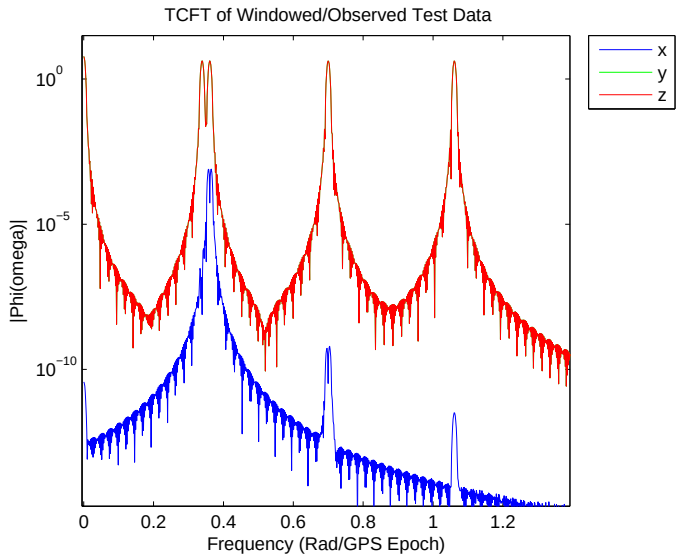

Figure 19. TCFT of Test Data ($\Omega_1 = .7$; $\Omega_2 = .361$, p=2, T=1000)

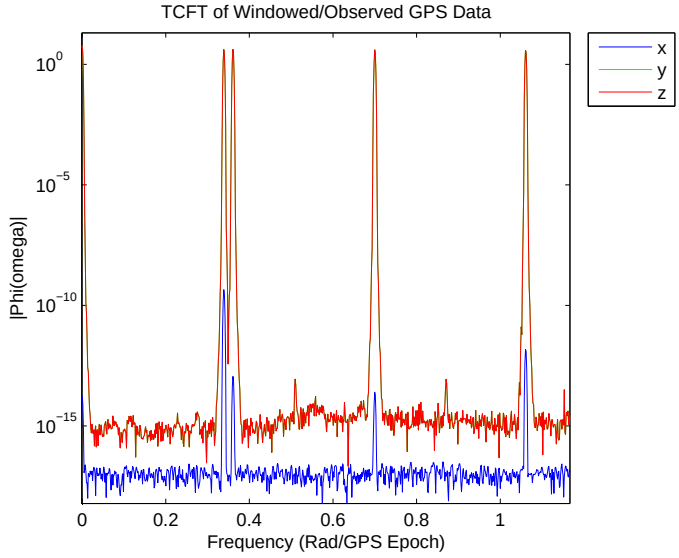

Figure 20. TCFT of Test Data ($\Omega_1 = .7$; $\Omega_2 = .361$, p=7, T=5000)

data was provided in the rotating frame in two-minute intervals. LAGEOS data in this form may be available for public use in 2010.

LAGEOS is a set of two spherical, passive, low area-to-mass ratio satellites used for space geodesy, geodynamics and fundamental physics studies. The satellites are tracked with extremely tight accuracy through laser ranging efforts, and accuracies in each axis are near 1 *cm* [55]. LAGEOS1 has an approximate semi-major axis of 12,270 km, an inclination of 109.8 degrees and an eccentricity of 0.004439 [1]. Using these parameters, the basis set for LAGEOS1 based on a 25-week data sample was approximated to be

Table 4. Basis Frequency Set for LAGEOS1

Basis Frequency	Value (Rad/15 minutes)
Ω_1	0.418010540006395
Ω_2	0.065566762302204
Ω_3	-4.432996482221456e-005

From Table 4 it is clear commensurability issues are not a problem. However, the basis frequency based on the apsidial regression rate is, like GPS, very small when compared to the others. The period of Ω_3 is just over 4 years, so it will once again need to be treated as a "static" frequency as decades of data were not available. Figure 21 shows a plot of the TCFT out through the first triplet structure for a 35-week sample of LAGEOS1 data. Unlike the GPS transform plots, the higher-order harmonics of the two fastest basis frequencies are clearly evident since these two frequencies have a ratio of about 6.38:1. There are also clear indications of several harmonics of the moon surrounding each of the main triplet peaks, the large peak near Ω_2, and the 0-frequency point. The lunar frequencies also appear sparsely around a few higher-order harmonics as well.

Two quick-look KAM-construction efforts were undertaken to see what success could be achieved. One was to use NAFF-like methods similar to Wiesel but in-

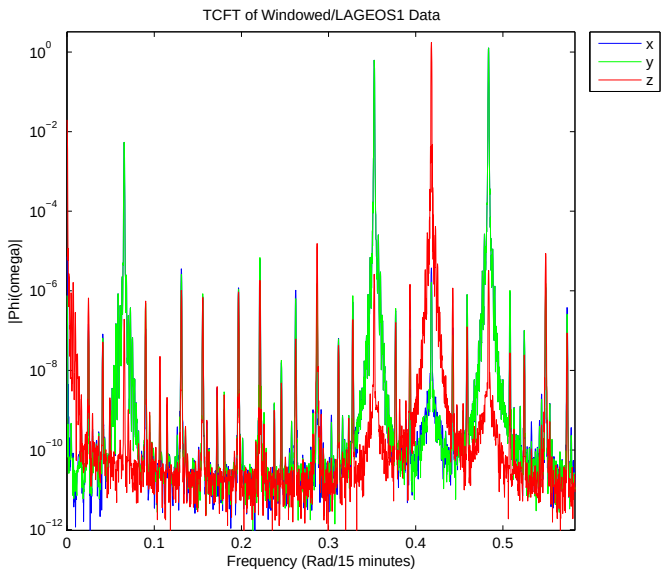

Figure 21. TCFT of LAGEOS1 Data (34 weeks/p=2)

cluding the synodic and anomalistic lunar frequencies while the other was to use a modified Laskar decomposition method. The latter would use a visual inspection of the transform in each axis to determine peaks to decompose rather than allow the process to proceed from peak-to-peak in largest-to-smallest, autonomous fashion. The intent was to avoid the sampling of a lobe and its subsequent residual false peaks, which was experienced with GPS data.

The first attempts used Wiesel-like methods on various time periods of LAGEOS1 data, from 1 week to 30 or more. The survey was designed to determine a cut-off time period, if one should exist, that captured sufficient short-frequency behavior without capturing too much long-frequency behavior. The only time span that kept residuals below 1 km was 1 week. The plots below at Figures 22.1 and 22.2 show the results of one particular trial with 20 weeks of LAGEOS1 data. The expansion chosen for the torus was $M = (4, 8, L6)$, where L6 means that 6 harmonics of both the anomalistic and synodic lunar frequencies were used. Figure 22.1 shows the familiar plot of observed vs. reconstructed transforms of the data in one axis, where the green

circles represent the frequencies chosen for decomposition. The Z-axis was chosen for illustration. From this plot, it can be seen that most of the peaks above 10×10^{-08} in magnitude have been accounted for. The subsequent plot at Figure 22.2 shows the error in this fit. Only the Z-axis was processed, so the 0-magnitude error lines are artifacts of not processing those axes' position data. Overall the fit is fairly good for a 20-week fit, but no where near precision levels. The error in the Z-axis is partially due the covering of smaller spectra by larger as well as the limited expansion done in the 2 basis frequencies used, but the fit is largely prohibited from precision quality due to poor frequency convergence at very low frequencies, namely the initial harmonics of the moon and Ω_3. Poor frequency resolution results in poor extraction of those frequencies' contributions in the data. The magnitude of this effect was not fully realized until after efforts taken that are described in the next chapter. Only then did it become clear that this is the primary limiting factor when applying trajectory following spectral methods.

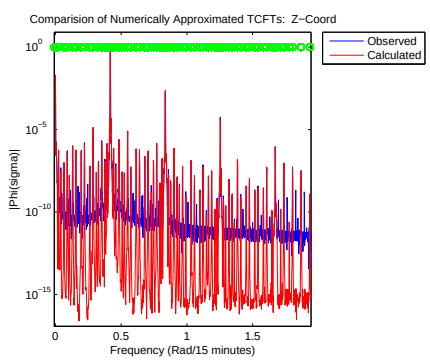

22.1: Orbital Data vs. Reconstruction

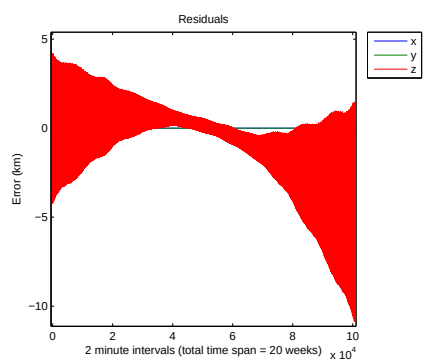

22.2: Residuals in Z-axis

Figure 22. Z-axis, 20-week LAGEOS1 Torus Fit (p=3/M = (4,8,L6))

The next quick-look effort used a slight modification of the NAFF method. Rather than let the algorithm identify peaks autonomously based on magnitude, the peaks were manually identified and presented to the NAFF for decomposition. Shorter time periods were chosen to keep slow-frequency effects to a minimum. The plots below at

Figures 23.1 and 23.2 show the results of one particular trial with 1 week of LAGEOS1 data. The expansion was manual, so no particular **M** can be given. Figure 23.1 once again shows a plot of the observed vs. reconstructed transforms of the data in one axis, where the green circles represent the frequencies chosen for decomposition. Only the Z-axis has been chosen here for illustration. From this plot, it can be seen that most of the peaks above 10×10^{-08} in magnitude have been accounted for. The subsequent plot at Figure 23.2 shows the error in this fit in all axes. The fit is decent, but once again no where near precision levels. As before, the error can be attributed to the limited expansion of the basis set, but a majority of the error is still due to poor frequency convergence as well as considerable omission of covered peaks and leakage effects due to the short period of data used. The poor characterization and decomposition of frequencies about the 0-frequency point, as discussed previously, also plays a part in the non-symmetric error in the Z-axis here.

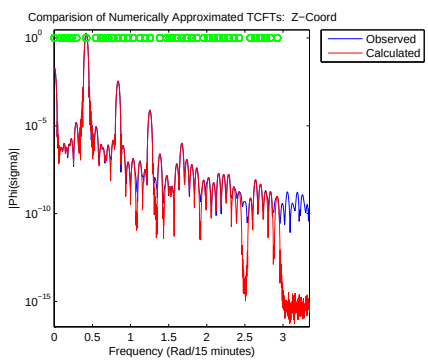

23.1: Orbital Data vs. Reconstruction

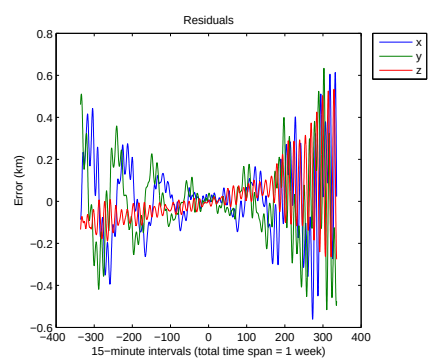

23.2: Residuals in Z-axis

Figure 23. Z-axis, 1-week LAGEOS1 Torus Fit (p=3/manual expansion)

While the incommensurability of the LAGEOS1 basis set and the inclusion of third-body frequencies allowed for considerable improvements in the orbital tori fits, they are still not to the level needed for precision applications. In addition to the problems presented by small values of Ω_3, the NAFF efforts, manual or otherwise, are hampered by leakage, lobe width, spectrally crowded peaks, and shoulder effects for

those peaks that they do sufficiently separate. It was believed that a way to mitigate these effects was to use a different fitting method, such as least squares, and/or use of the analytical form of the TCFT.

3.5 The Method of Least Squares

Since pure Fourier analysis methods failed to achieve desired results, a least squares method was sought to find a minimizing solution for the desired Fourier series, especially the Fourier coefficients. Laskar's NAFF approach would still be used to establish an initial estimate of the basis frequency set, but the coefficients would be determined by fitting the orbital data to an observation function relating the states (i.e. coefficients) to the data rather than inspection of the Fourier transform. The primary estimator/fitting algorithm in this work was chosen to be a batch form of least squares since it minimizes the sum of the square of the residuals as opposed to other methods, such as a minimax method like Chebyshev which minimizes the maximum error. This was primarily done since the sampled data being analyzed was already high-precision, smoothed data from a batch least squares run[3]. Thus, the desired effect of the estimator used here was to further smooth the data to a different observation relationship as opposed to compensating for excessive error.

By establishing an a priori basis frequency set, the estimation problem of coefficient determination reduces to a standard linear least squares algorithm if the observation, or measurement, relation is linear in the Fourier coefficients. This work used two such observation relations. This research also developed a nonlinear least squares routine to further refine the tori estimates, should the resulting fits not be sufficient due to small errors in the estimated basis set. Of course, by nonlinear it is meant that a linearized reference solution is created and used in a standard, linear

[3]IGS data has advsertised accuracies on the order of 2.5 centimeters rms in each axis.

least squares algorithm. A nonlinear approach is usually necessary when frequencies are added to the state since any observation relation will be nonlinear in terms of the frequencies. Since the nonlinear estimation case is the most general scenario, and it includes the entirety of the linear least squares estimation method, it will be fully developed here.

3.5.1 Initial Estimates of Fourier Coefficients.

A linear least squares estimate of the Fourier coefficients needs to be accomplished to create an a priori estimate of the state for the nonlinear least squares routine. This was accomplished in this work through the familiar problem of minimizing a sum of squared error terms. Most estimation texts detail linear least squares algorithms, however terminology varies. This work uses notation similar to that of Wiesel and Gelb [98, 38]. With that in mind, it can be more precisely said that we seek an estimate of the state vector, $\hat{\mathbf{x}}$, comprised of the Fourier series coefficients at epoch (i.e. $t_o = 0$) such that the following expression is satisfied:

$$\frac{\partial J}{\partial \hat{\mathbf{x}}} = \frac{\partial}{\partial \hat{\mathbf{x}}} \mathbf{e}^T \mathbf{e} = 0, \tag{55}$$

where J is the cost function to be minimized, $\mathbf{e}_i = \mathbf{z}_i - T_i \hat{\mathbf{x}}$ is the approximate error between the state estimate ($\hat{\mathbf{x}}$) and the measurement ($\mathbf{z}$) at every sample time, $T_i = H_i \Phi(t_i, t_o)$ is the linear mapping between the state at epoch and the measurement at each sample time, $\Phi(t_i, t_o)$ is the state transition matrix, and $\hat{\mathbf{x}} = [C_o \; C_j \; S_j \; \ldots]$, where $\mathbf{j}$ is once again the multiple summation vector. Since all of the states are constant in this problem, $\Phi(t_i, t_o) = I$ and Equation 55 becomes:

$$
\begin{aligned}
\frac{\partial J}{\partial \hat{\mathbf{x}}} &= \frac{\partial}{\partial \hat{\mathbf{x}}} \left\{ (\mathbf{z} - H\hat{\mathbf{x}})^T (\mathbf{z} - H\hat{\mathbf{x}}) \right\} && (56) \\
&= \frac{\partial}{\partial \hat{\mathbf{x}}} \left\{ \mathbf{z}^T\mathbf{z} - \mathbf{z}^T H\hat{\mathbf{x}} - \hat{\mathbf{x}}^T H^T \mathbf{z} + \hat{\mathbf{x}}^T H^T H\hat{\mathbf{x}} \right\} && (57) \\
&= -(\mathbf{z}^T H)^T - H^T\mathbf{z} + (\hat{\mathbf{x}}^T H^T H)^T + H^T H\hat{\mathbf{x}} && (58) \\
&= -2H^T\mathbf{z} + 2H^T H\hat{\mathbf{x}} && (59) \\
&= 0. && (60)
\end{aligned}
$$

Thus, the estimate of the state at epoch and the solution to the minimization problem is:

$$
\begin{aligned}
\hat{\mathbf{x}}(t_o) &= (H^T H)^{-1} H^T \mathbf{z} && (61) \\
&= P_{\hat{\mathbf{x}}}(t_o) H^T \mathbf{z}, && (62)
\end{aligned}
$$

where $P_{\hat{\mathbf{x}}}(t_o)$ is the state covariance matrix at epoch.

Finally, to obtain the solution to Equation 61 for the state vector of Fourier coefficients, several key pieces needed to be assembled: a set of sampled data, a linear transformation to map the states to the sampled data, and an a priori estimate of the basis frequencies to be used by this linear mapping. The basis frequencies have already been estimated by Fourier analysis, so the only pieces yet to be obtained are the linear mapping between the states and data as well as the form of the data itself.

The observation relationship (or linear mapping) is defined generically as:

$$
\mathbf{z}_i(t_i) = H_i \mathbf{x}(t_i), \tag{63}
$$

where H_i is the linear transformation matrix between the states (i.e. Fourier coef-

ficients) and the measurements. Initial estimation efforts attempted to directly fit the trajectory data to the Fourier series, so the linear mapping was the Fourier series representation of the assumed quasi-periodic oscillation:

$$z_i(t_i) = C_o + \sum_{\mathbf{j}} \left\{ C_{\mathbf{j}} \cos(\mathbf{j} \cdot \mathbf{\Omega} t_i) + S_{\mathbf{j}} \sin(\mathbf{j} \cdot \mathbf{\Omega} t_i) \right\}. \tag{64}$$

However, due to the near commensurability of the two dominant basis frequencies, the least squares algorithm failed to converge properly. Since the ratio of the second largest frequency to the largest frequency was 2.0000081 to 1, the principle and all subsequent harmonics of these two frequencies overlapped on each other such that the contributions of each individual integer combination of the basis frequencies became indistinguishable. It was determined that more success might be found by fitting the actual expression for the analytical, truncated, continuous Fourier transform (ATCFT) of the Fourier series within frequency domain instead of the Fourier series itself within the time domain. The merit of this idea lies in the fact that the ATCFT is the exact form of the transform. Thus, through the least squares estimator, each contribution to the ATCFT can be traced back to the time domain data incorporated into the estimate of the state. Wiesel attempted this in follow-on work to his first paper, however he did so with only one basis frequency at a time [100]. Once again, due to the near commensurability of the basis frequencies, this idea was expanded to use the two-frequency analytical form of the finite-time Fourier transform of the series found above at Equation 22. Only two frequencies were included since the third was once again ignored due to its small size. The final form of this analytical expression is:

$$
\begin{aligned}
ATCFT &= a_o \mathrm{sinc}(\omega T) \\
&\quad + \sum_{k=1}^{m} \Big\{ \frac{a_k}{2} \big\{ \mathrm{sinc}((\Psi - \omega)T) + \mathrm{sinc}((\Psi + \omega)T) \big\} \\
&\quad + \frac{ib_k}{2} \big\{ \mathrm{sinc}((\Psi + \omega)T) - \mathrm{sinc}((\Psi - \omega)T) \big\} \Big\},
\end{aligned} \tag{65}
$$

where $\Psi = (k_1\Omega_1 + k_2\Omega_2 + \ldots + k_m\Omega_m)$, $k \in \mathbb{Z}$ and in accordance to the summation vector $\mathbf{j}$. The derivation of this expression can be found in Appendix D. As can be seen by this expression, the result is simply a linear superposition of contributions from several *sinc* functions and it is easily seen how it could be expanded to account for any number of frequencies. Because of this, the contributions from each integer frequency combination can be stripped away and individually evaluated. As mentioned in this section and the previous chapter, this idea of fitting the exact analytical expression has been used in the past with successful results by a few authors [100, 85]. However, no research effort was found that tried to characterize a system with nearly two commensurate frequencies. As such, this effort pushed the envelope on the definition frequency commensurability from a practical standpoint. Now, considering Equations 65 and 63 as well as assuming a state vector of the form $\mathbf{x}^T = [C_o C_j S_j \ldots]$, where $\mathbf{j}$ is once again the multiple summation vector, $\mathbf{H}_{Coef}$ can quickly be seen to be:

$$
H_{Coef}^T = \begin{bmatrix} sinc(\omega T) & 0 \\ \frac{1}{2}(sinc((\Psi_j - \omega)T) + sinc((\Psi_j + \omega)T)) & 0 \\ 0 & \frac{1}{2}(sinc((\Psi_j + \omega)T) - sinc((\Psi_j - \omega)T)) \\ \vdots & \vdots \end{bmatrix}, \tag{66}
$$

where the final column dimension of $\mathbf{H}_{Coef}$ is dependent on the order of the Fourier

expansion, $\mathbf{M}$. The order of the Fourier series expansion can be done to arbitrary order, with the limiting factor in the order being the maximum number of Fourier coefficients desired, and unfortunately, the coefficients add up quickly as $\mathbf{M}$ increases. Every integer increment of $\mathbf{M}$ increases the number of coefficients by $8\mathbf{M}$ per coordinate axis. For example, if $\mathbf{M} = 2$ for both basis frequencies in a two-frequency system, that would generate 25 Fourier series coefficients per coordinate axis. By increasing to $\mathbf{M} = 3$, that number would increase by 24 for a total of 49 coefficients.

The last piece needed to execute the least squares algorithm was the data to be used. As indicated earlier, this research used high-precision estimates of GPS ephemerides provided by the IGS via final orbit files in SP3 format. However, since the function to be fit resides in the frequency domain, the time domain data, $\mathbf{z}_i(t_i)$, needed to be transformed to into frequency domain data, $\mathbf{z}_i(\omega_i)$, via the expression:

$$\Phi(\omega) = \frac{1}{2T} \int_{-T}^{T} f(t) e^{-i\omega t} dt. \tag{67}$$

This operation makes the data complex valued. Consequently, the measurement vector $\mathbf{z}_i(\omega_i)$ was created such that the real and imaginary parts of the Fourier-transformed time domain data were separated for numerical ease. This gives the state vector a length dimension of $2N$ instead of N, where N is still the number of coordinates in the system. Finally, with all least squares elements identified and/or defined, the solution to Equation 61 can be obtained.

3.5.2 Least Squares Fit of Frequencies and Coefficients.

Once initial estimates of the frequencies and coefficients have been accomplished, they can be treated as a reference state and then refined by a nonlinear least squares algorithm. To illustrate this mathematically, consider the following nonlinear differential equation model of the state:

$$\dot{\mathbf{x}} = \mathbf{f}[\mathbf{x}(t), t], \tag{68}$$

whose corresponding measurement equation is:

$$\mathbf{z}(t_i) = \mathbf{h}[\mathbf{x}(t_i), t_i]. \tag{69}$$

In these equations, the lower case notation for $\mathbf{f}$ and $\mathbf{h}$ signifies we are dealing with nonlinear expressions. Let a known solution nearby to the solution of Equation 68 for a particular problem be denoted as a reference solution (or nominal state solution) such that it satisfies the nonlinear state differential equation:

$$\dot{\mathbf{x}}_{ref} = \mathbf{f}[\mathbf{x}(t), t], \tag{70}$$

where $\mathbf{f}$ is the same as that found in Equation 68. Now, to investigate solutions about this reference solution, or if you will, a perturbation of the state, we can represent a perturbation of the state as:

$$[\dot{\mathbf{x}} - \dot{\mathbf{x}}_{ref}] = \mathbf{f}[\mathbf{x}(t), t] - \mathbf{f}[\mathbf{x}_{ref}(t), t]. \tag{71}$$

Equation 71 becomes useful once we find an approximation of it by expanding about the reference solution by way of a Taylor series. This yields:

$$[\dot{\mathbf{x}} - \dot{\mathbf{x}}_{ref}] = \left.\frac{\partial \mathbf{f}[\mathbf{x}(t), t]}{\partial \mathbf{x}}\right|_{\mathbf{x}=\mathbf{x}_{ref}(t)} [\mathbf{x} - \mathbf{x}_{ref}] + H.O.T. \tag{72}$$

Now, by ignoring higher order terms, we can find the first-order approximation about the reference solution to be:

$$\dot{\delta\mathbf{x}}(t) = \mathbf{A}[t; \mathbf{x}_{ref}(t)]\delta\mathbf{x}(t), \tag{73}$$

where $\mathbf{A}[t; \mathbf{x}_{ref}(t)]$ is a square matrix of size n of the partial derivatives of $\mathbf{f}$ with respect to the states, evaluated along the reference trajectory, or:

$$\mathbf{A}[t; \mathbf{x}_{ref}(t)] = \left.\frac{\partial \mathbf{f}[\mathbf{x}(t), t]}{\partial \mathbf{x}}\right|_{\mathbf{x}=\mathbf{x}_{ref}(t)}. \tag{74}$$

A solution to Equation 73 can be found which will approximate the solution to Equation 71. This approximate solution will remain valid as long as the omission of the higher order terms does not add significant error. However, recall this estimation problem has no dynamics to speak of since the system states are presumably constant, so the state state transition matrix is just an identity matrix. Hence, the solution to Equation 73 is just simply:

$$\delta\mathbf{x}(t) = \delta\mathbf{x}(t_o). \tag{75}$$

A similar linearization approach can be done to find a first-order approximation of the measurement relation found in Equation 69, and while the dynamics of the problem will provide simplification as well, they will not make it as trivial as Equation 75. Following the linearization process previously done, we see:

$$\delta\mathbf{z}(t_i) = \mathbf{H}[t; \mathbf{x}_{ref}(t_i)]\delta\mathbf{x}(t_i), \tag{76}$$

where $\mathbf{H}[t; \mathbf{x}_{ref}(t)]$ is an $[m\ x\ n]$ matrix of partial derivatives of $\mathbf{h}$ with respect to the states, evaluated at the reference solution. Explicitly, this means:

$$\mathbf{H}[t_i; \mathbf{x}_{ref}(t)] = \frac{\partial \mathbf{h}[\mathbf{x}(t), t_i]}{\partial \mathbf{x}}|_{\mathbf{x}=\mathbf{x}_{ref}(t_i)}. \tag{77}$$

Now, applying the dynamics of this problem to Equation 76, we get:

$$\delta\mathbf{z}(t_i) = \mathbf{H}[t; \mathbf{x}_{ref}(t_i)]\delta\mathbf{x}(t_o). \tag{78}$$

Upon close inspection of Equations 73 and 71, it can be seen that an estimator based on this linearized model estimates a partial, perturbed state rather than the whole state. Thus, in a filter such as this, the perturbed state estimate at any given time t will need to be *added* to the nominal state estimate at that given timestep to provide the whole-state estimate. This also means that in our estimator we desire to minimize the error in the perturbed state as opposed to error in the whole state as seen before in linear least squares formulation. Thus, defining the residual vector as:

$$\mathbf{r}_i = \mathbf{z}_i - \mathbf{h}[\mathbf{x}(t), t_i], \tag{79}$$

and noticing that Equation 78 relates the error in the measurement to the error in the reference solution, these relationships can be used as an estimate of the error in the perturbed state:

$$\mathbf{e}_i = \mathbf{r}_i - \mathbf{H}[t; \mathbf{x}_{ref}(t_i)]\hat{\delta\mathbf{x}}(t_o). \tag{80}$$

Hence, the familiar linear least squares solution can be immediately recalled to find that:

$$\begin{aligned}
\frac{\partial J}{\partial \hat{\delta\mathbf{x}}} &= \frac{\partial}{\partial \hat{\delta\mathbf{x}}}\left\{(\mathbf{r} - H\hat{\delta\mathbf{x}})^T(\mathbf{r} - H\hat{\delta\mathbf{x}}),\right\} && (81)\\
&= \frac{\partial}{\partial \hat{\delta\mathbf{x}}}\left\{\mathbf{r}^T\mathbf{r} - \mathbf{r}^T H\hat{\delta\mathbf{x}} - \hat{\delta\mathbf{x}}^T H^T\mathbf{r} + \hat{\delta\mathbf{x}}^T H^T H\hat{\delta\mathbf{x}}\right\} && (82)\\
&= -(\mathbf{r}^T H)^T - H^T\mathbf{r} + (\hat{\delta\mathbf{x}}^T H^T H)^T + H^T H\hat{\delta\mathbf{x}} && (83)\\
&= -2H^T\mathbf{r} + 2H^T H\hat{\delta\mathbf{x}} && (84)\\
&= 0, && (85)
\end{aligned}$$

where the linearization matrices over the entire time interval $2T$ have been concate-

nated and shortened to simply H for notational clarity. For completeness sake, H is explicitly defined as:

$$H = \begin{bmatrix} \mathbf{H}[t; \mathbf{x}_{ref}(t_{-T})] \\ \mathbf{H}[t; \mathbf{x}_{ref}(t_{-T+1})] \\ \vdots \\ \mathbf{H}[t; \mathbf{x}_{ref}(t_{T-1})] \end{bmatrix}. \tag{86}$$

Thus, the estimate of the state at epoch and the solution to the minimization problem is:

$$\hat{\delta\mathbf{x}}(t_o) = (H^T H)^{-1} H^T \mathbf{r} \tag{87}$$

$$= P_{\hat{\delta\mathbf{x}}}(t_o) H^T \mathbf{r}, \tag{88}$$

where $P_{\hat{\delta\mathbf{x}}}(t_o)$ is the state covariance matrix at epoch.

Just as in the least squares algorithm, to obtain the solution to Equation 109 for the state vector of Fourier coefficients and the basis frequencies, several key pieces needed to be assembled: a set of sampled data, a nonlinear observation function, a linearized version of the nonlinear observation function, and an a priori estimate of the basis frequencies and coefficients to be used by this linearized mapping. An initial, reference state and the form of the data have already been established, so the only pieces left are the nonlinear observation function and its linearization.

The nonlinear observation function, $\mathbf{z}(\omega)$, relating the states to the data is just Equation 65 for the ATCFT:

$$
\begin{aligned}
\mathbf{z}(\omega) &= a_o \mathrm{sinc}(\omega T) \\
&\quad + \sum_{k=1}^{m} \Big\{ \frac{a_k}{2} \big\{ \mathrm{sinc}((\Psi - \omega)T) + \mathrm{sinc}((\Psi + \omega)T) \big\} \\
&\quad + \frac{ib_k}{2} \big\{ \mathrm{sinc}((\Psi + \omega)T) - \mathrm{sinc}((\Psi - \omega)T) \big\} \Big\},
\end{aligned} \tag{89}
$$

and its linearization is already partially done from the initial least squares run to obtain an initial estimate of the Fourier coefficients. This portion of its linearized form can be seen at Equation 66. If we define this portion of linearization done for the coefficients as H_{Coef} and the linearization yet to be done for the frequencies as H_{Freq}, then the total linearization of $\mathbf{h}[\mathbf{x}(t), t_i]$ can be written as:

$$
H = \begin{bmatrix} H_{Coef,\, X-axis} & 0 & 0 & H_{Freq,\, X-axis} \\ 0 & H_{Coef,\, Y-axis} & 0 & H_{Freq,\, Y-axis} \\ 0 & 0 & H_{Coef,\, Z-axis} & H_{Freq,\, Z-axis} \end{bmatrix}, \tag{90}
$$

where H_{Freq} per coordinate axis is:

$$
H_{Freq} = \begin{bmatrix} \frac{\partial}{\partial \Omega_1} \Re(ATCFT) & \frac{\partial}{\partial \Omega_2} \Re(ATCFT) \\ \frac{\partial}{\partial \Omega_1} \Im(ATCFT) & \frac{\partial}{\partial \Omega_2} \Im(ATCFT) \end{bmatrix}. \tag{91}
$$

Thus, the elements of the array for a two-frequency system are:

$$
\begin{aligned}
H_{Freq}(1,1) &= \frac{C_{\mathbf{j}} k_{\mathbf{j},\,\mathbf{\Omega_1}}}{2} \frac{\partial}{\partial \Omega_1} \left\{ sinc(\Psi - \omega) + sinc(\Psi + \omega) \right\} \\
H_{Freq}(1,2) &= \frac{C_{\mathbf{j}} k_{\mathbf{j},\,\mathbf{\Omega_2}}}{2} \frac{\partial}{\partial \Omega_2} \left\{ sinc(\Psi - \omega) + sinc(\Psi + \omega) \right\} \\
H_{Freq}(2,1) &= \frac{i S_{\mathbf{j}} k_{\mathbf{j},\,\mathbf{\Omega_1}}}{2} \frac{\partial}{\partial \Omega_1} \left\{ -sinc(\Psi - \omega) + sinc(\Psi + \omega) \right\} \\
H_{Freq}(2,2) &= \frac{i S_{\mathbf{j}} k_{\mathbf{j},\,\mathbf{\Omega_2}}}{2} \frac{\partial}{\partial \Omega_1} \left\{ -sinc(\Psi - \omega) + sinc(\Psi + \omega) \right\},
\end{aligned}
$$

where $\mathbf{j}$ is once again the multiple summation vector, $k_{\mathbf{j},\,\mathbf{\Omega}}$ is the integer from the multiple summation vector $\mathbf{j}$ that corresponds to the basis frequency of which the partial derivative is being taken, and of course, the C_j and S_j variables are the coefficients of the Fourier series. Note, due to the "initial condition" Fourier coefficient, $C_{(0,0,\ldots,0)^N}$, not being a function of the basis frequencies, Equation 91 contains all Fourier coefficients except that of $C_{(0,0,\ldots,0)^N}$.

By using the basis frequency estimates from the NAFF algorithm and the Fourier coefficient estimates from the linear, least squares routine, the nonlinear, least squares routine was able to refine initial estimates of the orbital torus into a final, smoothed estimate. Figure 24 shows the residuals for one such torus using a 10-week GPS data batch. In this case, the Fourier series was expanded to the 6th order in Ω_1 and 6th order in Ω_2 (or $M = (6,6)$). This result is far from precision-level quality, and the estimator had to be forced to accept a large stopping criteria for it to converge. However, it does suggest that there may be a torus lurking beneath the noise. Unfortunately, the 2:1 resonance makes this torus, should it exist, much more elusive.

Efforts to increase the order of the Fourier series expansion in hopes to better the estimate were tried with mixed results. While increasing the M for Ω_1 does seem to contain/reduce the error growth over time, there is a limit to the order of the expansion due to the previously mentioned phenomena of decreasing observability into

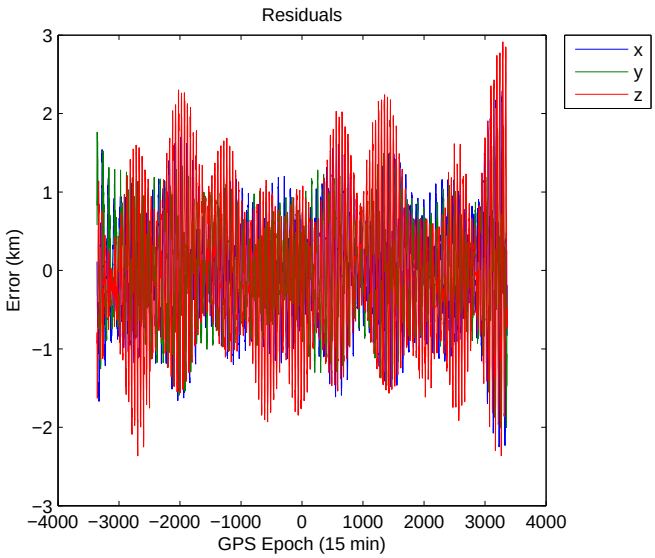

Figure 24. Least Squares Torus Fit (PRN22/10 Weeks/M = (6,6))

the states. At increasingly higher-order expansions, the estimator diverged to poor solutions, possibly indicating a large preponderance of local minima within the state space. Also, larger expansions were only possible in one frequency (specifically Ω_1), as trying to expand in both led to immediate divergence. Tori were also attempted to be fit to longer periods of data. Using the same expansion from Figure 24, the plot in Figure 25 shows a 52-week fit. The strength of the 3rd body and nonconservative perturbations are very prevalent in this plot as the filter had a hard time incorporating their effects into the limited torus model. This shows that on longer timescales, the third-body frequencies, at a minimum, absolutely must be accounted for in addition to the standard basis set.

3.6 Summary

In total, five variations on Laskar's NAFF decomposition method and two least squares methods were developed and tested in this chapter. All fell short in achieving desired results with precision GPS orbital data. Each successive method attempted to

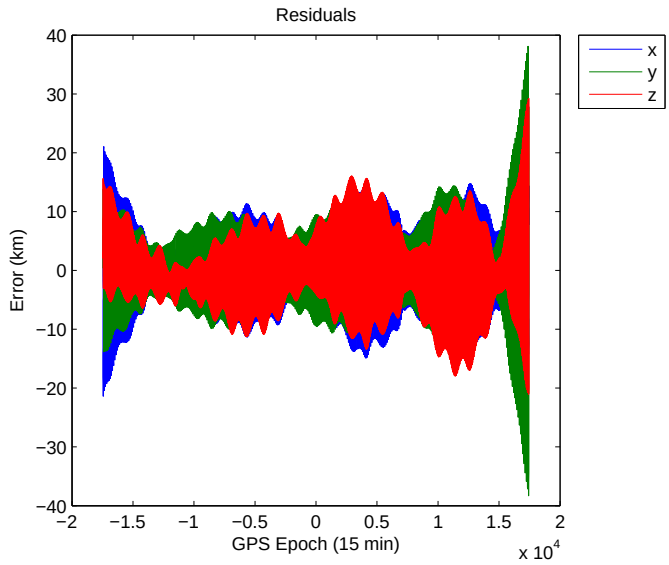

Figure 25. Least Squares Torus Fit (PRN22/52 Weeks/M = (6,6))

adapt to issues revealed by its predecessor, only to reveal others. Issues included those stemming from leakage, Fourier transform lobes covering nearby lobes, poor frequency convergence on slow frequencies, third-body perturbations, pseudo-Nyquist-Shannon limitations, and commensurability of frequencies. While the commensurability of GPS frequencies is not absolute, it is close enough from a practical perspective to meet the definition and it is the primary obstacle in numerically creating a GPS orbital torus via a trajectory following method.

To alleviate the near-commensurability problem, potentially hundreds of years of data may be required to properly separate the transform peaks such that the most significant ones could be analyzed for orbital torus construction. The same amount or more may be necessary to fully allow the NAFF algorithm to converge upon the slowest basis frequency. Even if this were feasible, increasing data batches to just a fraction of this size of a time span would most certainly cause third-body perturbations to not remain tolerable and they would need to be included into the torus model to make precision-level fits a possibility. Regardless, such long time spans make trajectory following spectral methods impractical for the operational

GPS mission. However, uses other than operational may be able to make use of the trajectory following methods since operational lifetimes are not a consideration and tight accuracies are not necessarily needed. These regimes are also not in a deep 2:1 resonance with the geopotential.

The method of least squares did help to find a torus "close" to that of the presumed actual torus by fitting to the ATCFT, however it appeared to easily get drawn into finding other local minima rather than the global solution. Hence, the torus found was not "close" enough for operational use. Thus, until a non-trajectory following method is developed or a way to circumvent the near-commensurability of the peaks is found, the operational GPS mission as we know it cannot benefit from this type of effort either. Of course, if the constellation were moved even 50 kilometers in altitude form where it is currently, trajectory following methods (either least squares based or otherwise) might be employed with somewhat better success. However, the issue of a very small third frequency would still remain, and as illustrated with two quick-look investigations with LAGEOS data, the z-axis is particularly prone to error due to the NAFF's poor convergence on this frequency with relatively small batches of data.

IV. Spectral Decomposition by Frequency Groupings

GPS KAM tori construction efforts using trajectory following methods proved difficult for several reasons, but primarily due to two main issues: near-commensurability of the basis frequencies and limits on frequency detection/resolution due to sampling restrictions similar to that of the Nyquist-Shannon Theorem. As previously discussed, little can be done to relieve problems stemming from near-commensurability if the amount and length of the data processed is kept to quasi-operational levels and the desire is to contain algorithm complexity. While very long sample periods and increased sampling rate do help, practical limits are ultimately the inhibiting factors when considering the use of more data. Similar to the issues associated with near-commensurability, frequency convergence problems rising from sampling/detection limits may also be solved, or at least mitigated, by sampling for longer periods and at faster rates. Unfortunately, the similarity to near-commensurability continues as the increase in frequency resolution is also checked by the practicality of using longer and larger amounts of data for man-made missions. Excluding these two primary issues, the rest of the impediments to GPS orbital tori construction have revealed themselves as shortcomings of the methods chosen, either from dealing with relatively short periods of sampled data or the algorithm used.

In previous work alluded to by this research, the NAFF had been used with literally millions of years of integrated data for problems within the solar system. Even though periodicities in these types of problems are much longer than those within the GPS regime, the spectral plots should be expected to be dominated by much sharper peaks than those obtained by this research. As such, the problems manifesting from wide and interfering lobe shoulders were not felt to the level experienced in the previous chapter with GPS and LAGEOS data samples, which precluded precision orbital tori fits. Akin to other roadblocks discussed, longer and more frequent

sampling may not provide sufficient relief from these issues. Another way to deal with these problems is to use the ATCFT in the fitting process, as discussed in Chapter III, as opposed to determining the Fourier coefficients directly from the spectral plot. It has already been shown that a least squares method can use the ATCFT. While this method did not elicit completely favorable results, it did not do so because of limitations inherent with the ATCFT. Rather, the least squares GPS algorithm's difficulties came from near-commensurability, third-body perturbations and the large state vector arrays needed when solving for all coefficients simultaneously. Inverting sometimes poorly conditioned, multi-thousand-element square arrays is not only a burdensome computational task, but it also revealed issues in the solution space, namely the potential to be influenced by nearby local minima. Thus, the desired end result of a n-tuple Fourier series still appeared to be valid, but the how, what and where of asking the question needed to change. It was believed the ATCFT would be the key to achieve the desired results.

Any trajectory-following, torus-fitting solution must address most, if not all, of the issues listed previously to be successful. Additionally and probably most importantly, the method must be applied to orbital regimes where it may experience more favorable outcomes. A method recognizing these shortcomings was attempted with considerable benefit. It bases its approach on sectioning the spectral plot into groups of frequency lines as opposed to a collection of individual peaks and using the ATCFT to fit this structure. Further, it backed away from using real-world, high-precision data, which is limited not only in availability but also by sampling rate, to a more controlled integrated data source as a beginning data set, with the intent of increasing fidelity of the integrated data until success with real-world data was achieved or failure was attained. The rest of this chapter details the premise of the new approach, the methods built on this idea, and the results garnered.

As presented in the previous chapter, Table 5 summarizes the spectral methods employed for all orbital tori construction efforts, to include GPS and LEO. The table clearly shows that avoiding nearly commensurate frequencies and increasing the number of periods of each basis frequency within the sampled data results in much better reconstruction of the orbital trajectory.

Table 5. Summary of Trajectory Following Spectral Methods

Orbit Type	Type of Data	Methods Applied	Issues	Key Results
MEO	Observed	3-Freq, Modifed NAFF	Near-commensurability, Small Ω_3, Unmodeled perturbations	Excessively large error
MEO	Observed	2-Freq, Modified NAFF	Near-commensurability, Small Ω_3, Unmodeled perturbations	Large error, Linear error growth $>$ 15 km per axis for 10-wk fit
MEO	Observed	1-Freq, Modified NAFF	Near-commensurability, Small Ω_3, Unmodeled perturbations	Large error (especially in Z-axis) Linear error growth $>$ 30 km per axis for 10-wk fit
MEO	Observed	NAFF	Near-commensurability, Small Ω_3	Error on the order of meters, however no underlying torus
LEO	Integrated	Frequency Cluster Decomp	Potential for small Ω_3 depending on orbital parameters	Error in fits range from a few meters to a few kilometers
LEO	Integrated	Least Squares Decomp	Potential for small Ω_3 depending on orbital parameters	Error in fits range from a few meters to a tens of kilometers, High sensitivity to "small" Ω_3
LEO	Integrated	Least Squares Decomp w/ Coefficient Correction by Simulated Annealing	Potential for small Ω_3 depending on orbital parameters	Corrects large errors due to "small" Ω_3. Error similar to that of cluster-based method

4.1 Geopotential Model and Satellite Dynamics

The geopotential model, $\mathcal{V}$, chosen for the numerical integrator within this chapter was a spherical harmonic model with coefficients through the 21st order and degree [97]. The coefficients used were taken from the National Aeronautics and Space Administration's (NASA) EGM96 solution [68]. This model was placed in a frame that is stationary with respect to the geopotential and tied to the center of the earth. As discussed in Section 3.3, this is the ECEF frame. This frame is modeled as a simple, Cartesian coordinate system whose X-Z plane is formed by orthogonal rays originating from the center of the earth and passing through the Prime Meridian and North Pole, respectively. The Y-axis lies in the plane of the equator with the X-axis and is found as the right-hand rule is completed. The difference between it and the earth-centered inertial frame is a single rotation about the Z-axis through an

angle formed between the inertial reference point and the Prime Meridian. Choosing a satellite's rectangular coordinate vector, $\mathbf{r}$, in the ECEF frame as the generalized coordinate position vector, $\mathbf{q}$, the time derivatives of that vector simply become the inertial velocities resolved in the ECEF frame:

$$\dot{\mathbf{r}} = \mathbf{v} = \begin{bmatrix} \dot{x} - \omega_{\oplus} y \\ \dot{y} + \omega_{\oplus} x \\ \dot{z} \end{bmatrix}, \tag{92}$$

where $\omega_{\oplus}$ is the rotation rate of the earth. The kinetic energy is easily calculated as $\mathcal{T} = \frac{1}{2}\mathbf{v}^2$ such that Lagrangian, $\mathcal{L}$, quickly becomes:

$$\begin{aligned} \mathcal{L} &= \mathcal{T} - \mathcal{V} \\ &= \frac{1}{2}\left((\dot{x} - \omega_{\oplus} y)^2 + (\dot{y} + \omega_{\oplus} x)^2 + (\dot{z})^2\right) \\ &\quad - \frac{\mu}{r} \sum_{n=1}^{\infty} \sum_{m=1}^{n} \left(\frac{r}{R_{\oplus}}\right)^{-n} P_n^m[\sin(\delta)]\{C_{nm}\cos(m\lambda) + S_{nm}\sin(m\lambda)\}, \end{aligned} \tag{93}$$

where μ is the gravitational parameter, $R_{\oplus}$ is the equatorial radius of the earth, C_{nm}, S_{nm} are the field coefficients that complete the gravity model, and P_m^n are the usual associated Legendre polynomials. The radius, r, geocentric latitude, δ, and east longitude λ, are found from [99]:

$$r = \sqrt{x^2 + y^2 + z^2} \tag{94}$$

$$\sin(\delta) = \frac{z}{\sqrt{x^2 + y^2}} \tag{95}$$

$$\tan(\delta) = \frac{y}{x}. \tag{96}$$

Thus, the momenta become the following after applying $p_i = \frac{\partial \mathcal{L}}{\partial \dot{q}_i}$:

$$\mathbf{p} = \begin{bmatrix} \dot{x} - \omega_{\oplus} y \\ \dot{y} + \omega_{\oplus} x \\ \dot{z} \end{bmatrix}, \tag{97}$$

which are just the inertial velocities resolved in the rotating earth frame that were found previously. Inverting the momenta to form the coordinate velocities, $\dot{q}_i$, in terms of the momenta, forming the the Hamiltonian according to $\mathcal{H} = \sum_i p_i \dot{q}_i - \mathcal{L}$, and applying Hamilton's equations found beginning at Equation 3 gives the EOMs as:

$$\begin{bmatrix} \dot{\mathbf{q}} \\ \dot{\mathbf{p}} \end{bmatrix} = \begin{bmatrix} p_x + \omega_{\oplus} q_y \\ p_y - \omega_{\oplus} q_x \\ p_z \\ \omega_{\oplus} p_y - \frac{\partial \mathcal{V}}{\partial q_x} \\ \omega_{\oplus} p_x - \frac{\partial \mathcal{V}}{\partial q_y} \\ -\frac{\partial \mathcal{V}}{\partial q_z} \end{bmatrix}, \tag{98}$$

where the partial of the potential function with respect to each coordinate is dependent on the position of the satellite. These equations were integrated with a Hamming fourth-order predictor-corrector algorithm. Since the Hamiltonian is independent in time, it is a constant of the motion. Consequently, it was used as a numerical check of the integrator. For LEO orbits, error in the Hamiltonian was on the order of $10x10^{-13}$ over 6 months.

4.2 A Frequency Cluster-Based Approach

The method chosen to evolve the concept of trajectory-following KAM tori construction was that based on decomposing clusters of frequencies from the data, as opposed to the single frequency lines themselves, by using the ATCFT. Employing the ATCFT mitigates some problems associated with short-length data samples by taking into account the exact shape of the Fourier transform. Previous efforts have relied mostly on assuming that the transform was close enough to the idealized form, a long succession of dirac delta functions, and determining by a quasi-inspection method the value of the Fourier coefficients. By using the ATCFT, the decomposition algorithm is allowed to successively solve for and extract local bands of coefficients and their associated frequency content under local transform effects (i.e. effects from large main lobes as well as shoulders of nearby transform peaks). In the context of least squares, this method will be most helpful since the size of the state vectors will be reduced by several orders of magnitude when compared to previous efforts that solved for all coefficients simultaneously. To further motivate this concept, a plot of a high-resolution Fourier transform of an integrated orbit is shown at Figure 26. The orbit portrayed is a low earth orbit (LEO) with an approximate semi-major axis of 1.1 Earth radii, an eccentricity of 0.05 and an inclination of 30 degrees.

The spectral plot is similar to those previously shown in that the transform is displayed through the first main triplet structure, however due to the higher frequencies found in LEO, many more decaying harmonics of the fastest two frequencies appear and the individual harmonics of Ω_3 are evident. A closer inspection of the main triplet at Figure 27 reveals the rich Ω_3 detail hinted at in Figure 26. The methods developed in this chapter attempt to solve for or fit these bands of Ω_3 frequency peaks flanking each larger, central integer-multiple of the basis frequencies. These local bands are referenced to here as frequency clusters. Figure 27 also allows the more significant

local abberations in the transform to be seen more clearly and shows that in addition to the shoulders and peak widths within a cluster being troublesome, the shoulders from nearby clusters are also affecting coefficient determination. While the former will be mitigated by the ATCFT, the latter can be addressed by extracting each frequency cluster's contribution to the data in descending order of magnitude.

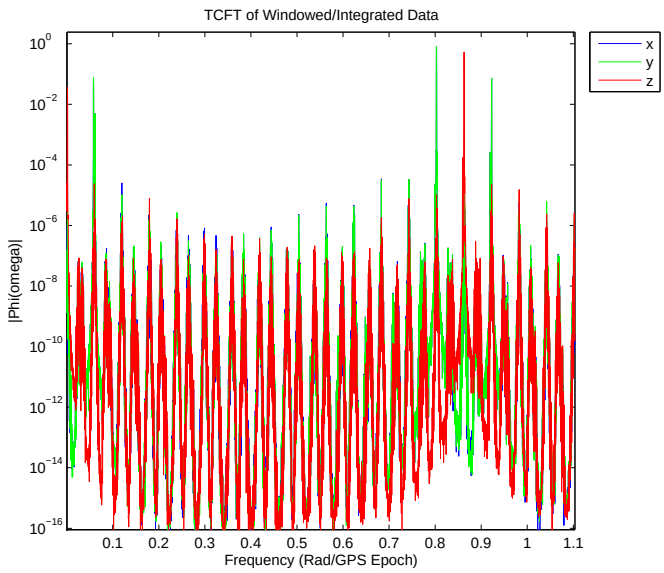

Figure 26. Spectra of Integrated Orbit (a=1.1 Re, e=0.05, i=30 deg)

4.2.1 Orbit Survey.

The commonly smallest basis frequency, Ω_3, has shown to be a formidable obstacle. Treating it as static has not been permissable since it does not just simply manifest as itself, but also as part of faster, more dominant frequencies within the data. As such, ignoring it induces error quickly and negates the prospect of precision orbital tori fits. However, it has up to this point also been so small that being able to fully characterize its individual spectral signature has not been possible while using short data samples, relatively speaking. A survey of how Ω_3 changes with semi-major axis, eccentricity, and inclination was accomplished to see which orbits may allow more

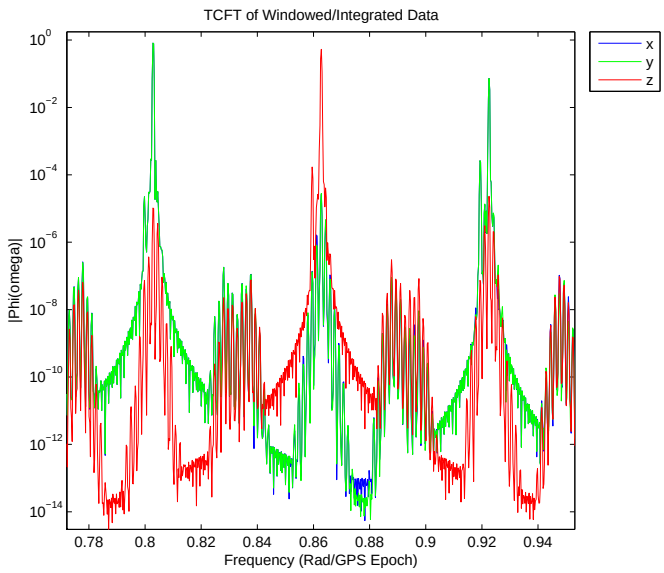

Figure 27. High-Detail Plot of Integrated Orbit's Primary Triplet

success for the trajectory following methods. The plots at Figures 28.1 and 28.2 show graphical forms of some results due to a particular set of initial conditions. Similar plots for the rest of the basis set can be found in Appendix G.

The plot at Figure 28.1 shows estimates of Ω_3 due to J2, varying on the orbital parameters of inclination and semi-major axis. The plot assumes a static value of 0.01 for eccentricity and that only one year of data is available. The two horizontal axes are intuitive, but the vertical axis shows values of Ω_3 in terms of periods per one year interval instead of using the more expected form of frequency units. This was done to more clearly convey where the useful limits within the data lie. Recall that approximately two periods of Ω_3 are needed within the sampled data to capture it spectrally in the plot of the Fourier transform. Hence, red planes are inserted at $\pm$ 2 periods per year. The negative sign is not indicative of negative periods, but that the sign of Ω_3 has flipped. The sign itself represents direction of rotation and not a positive or negative frequency. Clearly, from this picture, Ω_3 quickly approaches the no-go limit as the semi-major axis approaches 2 Earth radii (Re) and/or the

inclination nears the critical inclination. As the inclination approaches 90 degrees, Ω_3 does get large enough for potential analysis, as long as the semi-major axis stays close to 1 Re. While the red limits suggest clear stops, there is more than likely a practical limit somewhere short of them. The next sections will examine the details of the cluster-based approaches developed and the investigation on where those practical limits lie. The plot at Figure 28.2 has been included here to illustrate that a change in eccentricity has a much smaller effect on Ω_3 than does inclination and semi-major axis. In this plot, the semi-major axis is held constant at 1.1 Re while inclination and eccentricity are varied.

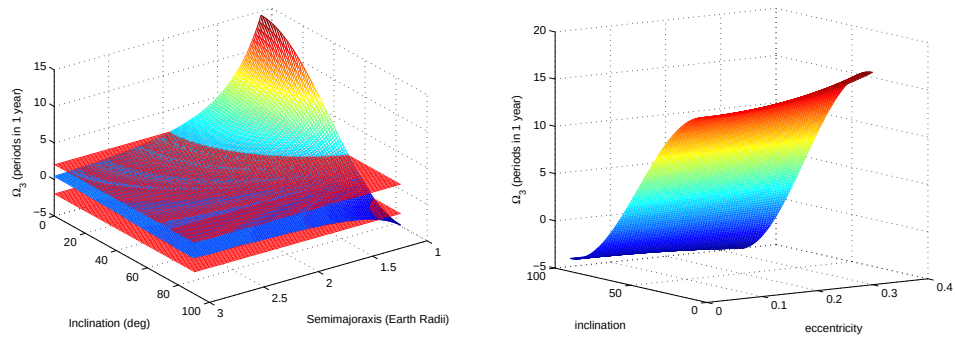

28.1: Sweep on Inclination/Semi-major Axis

28.2: Sweep on Inclination/Eccentricity

Figure 28. Orbital Survey of Acceptable Ω_3 Magnitudes

4.3 Decomposition by Frequency Clusters

The underlying premise of the frequency cluster decomposition method is to use the windowed form of the ATCFT to solve for the Fourier coefficients of a set of spectral lines that have strong spectral correlation by setting the analytical approximation of the Fourier transform of each spectral line equal to that of its numerically calculated value. Of note, is that the analytical expression used approximates the windowed ATCFT of the cluster by using a summed total of the individual analytical

contributions of each frequency line in the cluster. This is noteworthy as it lends itself easily to a system of linear equations. By solving for the imaginary and real portions of the Fourier transform separately, a linear system of n equations and n unknowns materializes, where n is twice the number of frequency lines being fit. Since there are two Fourier coefficients for every line, this gives a square system to solve in the familiar form of:

$$Ax = b. \tag{99}$$

The solution vector, x, is an $[n\ x\ 1]$ column vector of the alternating sine and cosine Fourier coefficients for each cluster spectral line. The result vector, b, is an $[n\ x\ 1]$ column vector of alternating real and imaginary portions of the actual numerically calculated Fourier transform corresponding to the coefficient pairs in the to-be-determined solution vector. The matrix of coefficients, A, is appropriately composed of coefficients in the linear system. Its construction is somewhat more complicated and requires a bit of extra care in it description.

The coefficients of the A matrix at Equation 99 are alternating rows of the real and imaginary portions of the summed Fourier coefficient terms in the windowed ATCFT expression, with the type of row depending on the type of value in the result vector (i.e. real or imaginary portion of the calculated Fourier transform value at that frequency line). Recall from Section 3.5.1 that the non-windowed ATCFT is obtained by taking the Fourier transform of the presumed n-tuple Fourier series form of the data:

$$\mathbf{q}(t) = C_{(0,0,\ldots,0)^N} + \sum_{\mathbf{j}} \left\{ C_{\mathbf{j}} \cos(\mathbf{j} \cdot \mathbf{\Omega} t) + S_{\mathbf{j}} \sin(\mathbf{j} \cdot \mathbf{\Omega} t) \right\}, \tag{100}$$

where the multiple index summation vector $\mathbf{j}^T = (j_1, j_2, \ldots, j_N)$ is carried out to any

arbitrary integer limit $\mathbf{M}$ in each element and axis, $\Omega^T = (\Omega_1, \Omega_2, \ldots, \Omega_N)$ is the basis frequency set, and N is the dimension of the basis set. After taking the transform, the ATCFT is seen to be:

$$\begin{aligned} ATCFT &= a_o \mathrm{sinc}(\omega T) \\ &\quad + \sum_{k=1}^{m} \Big\{ \frac{a_k}{2} \big\{ \mathrm{sinc}((\Psi - \omega)T) + \mathrm{sinc}((\Psi + \omega)T) \big\} \\ &\quad + \frac{ib_k}{2} \big\{ \mathrm{sinc}((\Psi + \omega)T) - \mathrm{sinc}((\Psi - \omega)T) \big\} \Big\}, \end{aligned} \tag{101}$$

where $\Psi = (k_1\Omega_1 + k_2\Omega_2 + \ldots + k_m\Omega_m)$, $k \in \mathbb{Z}$ and in accordance to the summation vector $\mathbf{j}$. Thus, Ψ is a composite coordinate variable composed of integer multiples of the basis set to represent each cluster spectral line. The derivation of the ATCFT can be found in Appendix D. To get the windowed form of the ATCFT, the desired window function of the form:

$$\chi_p\left(\frac{t}{T}\right) = \frac{2^p (p!)^2}{(2p)!} \left(1 + cos\left(\pi \frac{t}{T}\right)\right)^p, \tag{102}$$

where p is the order of the window, must be multiplied with the n-tuple Fourier series form prior to taking the transform, or the transformed form of the window must be convolved with the version of the ATCFT found at Equation 101. Either way, this is a daunting task by hand. However with the aid of Mathematica©, the analytical forms of these coefficients were easily obtained. For a Hann window of order two, the matrix of coefficients elements for spectral lines within a single frequency cluster are:

$$
\begin{aligned}
C &= -(2e^{-iT\omega}\pi^4((-1+e^{2iT\omega})(4i\pi^4\omega - 5i\pi^2T^2\omega(3\Psi^2+\omega^2) \\
&+iT^4\omega(5\Psi^4+10\Psi^2\omega^2+\omega^4)\cos[T\Psi] \\
&+(1+e^{2iT\omega})\Psi(4\pi^4 - 5\pi^2T^2(\Psi^2+3\omega^2) \\
&+T^4(\Psi^4+10\Psi^2\omega^2+5\omega^4))\sin[T\Psi])))/ \\
&(T(-\Psi^2+\omega^2)(16\pi^8+T^8(\Psi^2-\omega^2)^4 - 40\pi^6T^2(\Psi^2+\omega^2) \\
&-10\pi^2T^6(\Psi^2-\omega^2)^2(\Psi^2+\omega^2)+\pi^4T^4(33\Psi^4-2\Psi^2\omega^2+33\omega^4))) \quad (103)
\end{aligned}
$$

and

$$
\begin{aligned}
S &= -(2e^{-iT\omega}\pi^4((-1+e^{2iT\omega})(4\pi^4\Psi - 5\pi^2T^2(\Psi^3+3\Psi\omega^2) \\
&+T^4(\Psi^5+10\Psi^3\omega^2+5\Psi\omega^4)\cos[T\Psi] \\
&-i(1+e^{2iT\omega})\omega(4\pi^4 - 5\pi^2T^2(3\Psi^2+\omega^2) \\
&+T^4(5\Psi^4+10\Psi^2\omega^2+\omega^4))\sin[T\Psi])))/ \\
&(T(-\Psi^2+\omega^2)(16\pi^8+T^8(\Psi^2-\omega^2)^4 - 40\pi^6T^2(\Psi^2+\omega^2) \\
&-10\pi^2T^6(\Psi^2-\omega^2)^2(\Psi^2+\omega^2)+\pi^4T^4(33\Psi^4-2\Psi^2\omega^2+33\omega^4))), \quad (104)
\end{aligned}
$$

where C is the coefficient of each cosine term and S is the coefficient of each sine term. Also, T is the half-interval of the data, Ψ is the spectral cluster line of interest and ω is the sweep frequency, which is an element of the vector of frequency cluster spectral lines currently under investigation. To ease issues with the singularity experienced as Ψ approaches ω, L'Hopital's rule was applied. In this case, the coefficients found previously become:

$$C = \frac{\pi^8\Psi - 5\pi^6\Psi^3 + 4\pi^4\Psi^5 + \pi^8\cos[\Psi]\sin[\Psi]}{2\pi^4\Psi(\pi^4 - 5\pi^2\Psi^2 + 4\Psi^4)} \tag{105}$$

and

$$S = -\frac{i(\pi^8\Psi - 5\pi^6\Psi^3 + 4\pi^4\Psi^5 - \pi^8\cos[\Psi]\sin[\Psi])}{2\pi^4\Psi(\pi^4 - 5\pi^2\Psi^2 + 4\Psi^4)}. \tag{106}$$

The expressions for the coefficients while using Hann windows of order one and three as well as their expressions for when $(\omega^2 - \Psi^2)$ is close to zero can be found in Appendix F.

In the interest of compactness of the final form of the linear system described at Equation 99, define the Fourier coefficient pair for each spectral line as $\mathcal{K}$. This makes the $[2\ x\ 1]$ coefficient row vector for the *ith* spectral line Ψ_i become $\mathcal{K}_{[\Psi_i]}$ or:

$$\mathcal{K}_{[\Psi_i]} = [C_{[\Psi_i]} \quad S_{[\Psi_i]}], \tag{107}$$

where Ψ_i is as before. Thus, the two $[2\ x\ 1]$ row vectors representing the real and imaginary halves of this coefficient vector $\mathcal{K}_{[\Psi_i]}$ can be written as $\Re(\mathcal{K}_{[\Psi_i]})$ and $\Im(\mathcal{K}_{[\Psi_i]})$, respectively. By labeling each cluster line's Fourier coefficient set with respect to the sweep variable values (i.e. the other spectral lines, $(\Psi_j : j = 1, \ldots, n; j \neq i)$, in the cluster), a complete shorthand version of Equation 99 takes shape. Equation 108 shows this form explicitly.

$$\begin{bmatrix} \Re(\mathcal{K}_{[\Psi_1]_{wrt\ \Psi_1}}) & \cdots & \Re(\mathcal{K}_{[\Psi_1]_{wrt\ \Psi_n}}) \\ \Im(\mathcal{K}_{[\Psi_1]_{wrt\ \Psi_1}}) & \cdots & \Im(\mathcal{K}_{[\Psi_1]_{wrt\ \Psi_n}}) \\ \vdots & \vdots & \vdots \\ \Re(\mathcal{K}_{[\Psi_n]_{wrt\ \Psi_1}}) & \cdots & \Re(\mathcal{K}_{[\Psi_n]_{wrt\ \Psi_n}}) \\ \Im(\mathcal{K}_{[\Psi_n]_{wrt\ \Psi_1}}) & \cdots & \Im(\mathcal{K}_{[\Psi_n]_{wrt\ \Psi_n}}) \end{bmatrix} \begin{bmatrix} C_{\Psi_1} \\ S_{\Psi_1} \\ \vdots \\ C_{\Psi_n} \\ S_{\Psi_n} \end{bmatrix} = \begin{bmatrix} \Re(\Phi(\Psi_1)) \\ \Im(\Phi(\Psi_1)) \\ \vdots \\ \Re(\Phi(\Psi_n)) \\ \Im(\Phi(\Psi_n)) \end{bmatrix} \tag{108}$$

Once the cluster coefficients have been solved for, the cluster is extracted from the data similarly done in Section 3.4.2. As alluded to previously, the clusters should be processed in order of magnitude, largest to smallest, as to minimize effects from neighboring clusters' shoulders. This process should be repeated until desired accuracy in the fit is achieved. As an illustrative example, the year-long orbit depicted in Figure 26 was decomposed and reconstructed using this frequency cluster decomposition method, using an $\mathbf{M} = (6, 14, 6)$ expansion of the basis set. After decomposition, the orbit was recreated from the estimated basis set and numerically calculated Fourier coefficients. The residuals in the fit can be found at Figure 29. Clearly, the fit is excellent, especially considering the time span is one year. The 1-dimensional root mean square (rms) values for the X-, Y-, and Z-axis residuals are 3.87, 3.88 and 1.98 *meters*, respectively. The maximum residuals in each axis were 18.83, 17.58 and 9.35 *meters*, in the same order as previously listed.

Figure 30 shows a comparison of Fourier transforms before and after decomposition for a small portion of the X-coordinate axis. Notice how the cluster peaks are cleanly removed from orbital data based on the index chosen for the third basis frequency. In this case, the value chosen was 6 and as such, one harmonic of Ω_3 was left in the central cluster. This peak roughly contributes error on the order of centimeters or less, but it could be removed with a simple increase of 1 in the third element of $\mathbf{M}$.

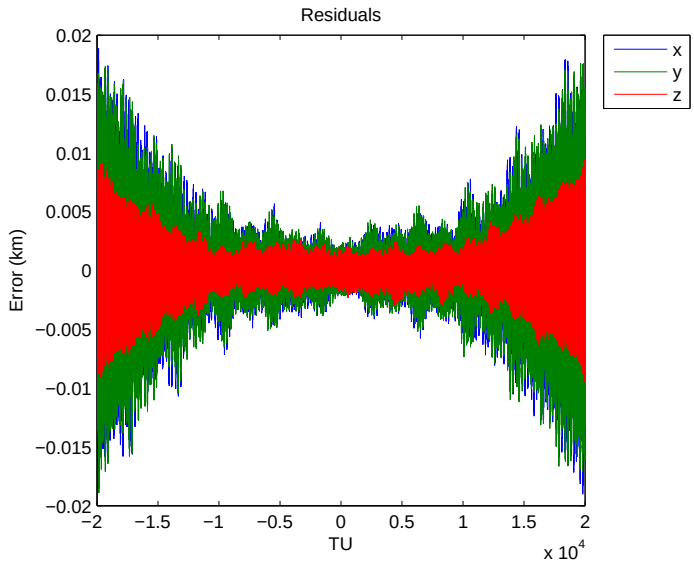

Figure 29. Cluster Decomposition Torus Fit (a=1.1 Re, e=0.05, i=30 deg)

The remaining clusters in this plot could be removed by increasing the second element of **M**, as the centers of each cluster represent echoes of the second basis frequency, or by possibly fitting the binary cluster structure born from the collision of the two clusters. The latter would need to be done only if treating each cluster independently did not lead to clean decompositions of both cluster structures.

Figure 31 illustrates the importance of using the frequency cluster method. If instead of fitting the entire frequency cluster structure, the individual lines of each cluster are removed sequentially, the result of the fit is much worse, as this figure shows. Instead of a maximum error of about 20 meters at $\pm$ 6 months from the center of the fit, the error is oscillatory with a maximum value near 60 meters during the entire time window. As a result, the 1-D rms values grow significantly for the X, Y and Z axes and are 25.20, 25.20, and 13.45 *meters*, respectively. While these values are still impressive considering the time span, it is the disparity between the two methods that is of concern. As the orbital parameters change to those of higher altitude and greater inclination, the disparity continues to grow. The orbits that show the worst effects are those where Ω_3 is exceptionally small (i.e. in the vicinity

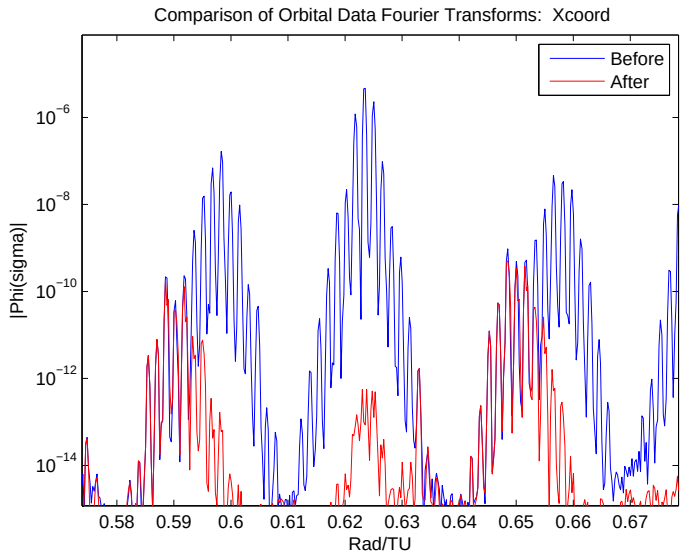

Figure 30. Comparison of Pre- and Post-Decomposition Transforms

of the critical inclination). Appendix H shows examples of these types of residuals for other orbital initial conditions.

4.3.1 Survey of Results.

The cluster decomposition algorithm was applied to several year-long orbit samples within the LEO belt. Test cases were chosen such that the data contained at least two periods of Ω_3, with the intent of defining a performance envelope for the algorithm. Hence, per Figure 28.1, initial cases focused on low-altitude, low-inclination orbits with low eccentricities where success was nearly guaranteed. Then, since a change in eccentricity has a smaller effect on the size of Ω_3 than semi-major axis and inclination, the latter two were varied while holding eccentricity constant. In all cases, an expansion in the basis frequencies of $\mathbf{M} = (6, 14, 6)$ was performed. These values were chosen as they accounted for most peaks at or below 10×10^{-08} in magnitude. Normally, a one-size-fits-all approach should not be used for orbital torus construction as each orbit is unique, but it was done during this effort so that comparisons could be drawn between test cases. Figure 32 shows a residual summary

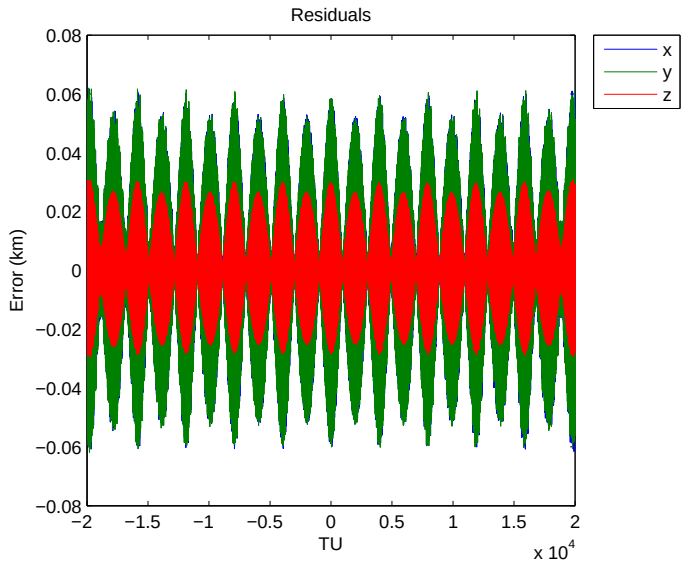

Figure 31. Torus Fit Error w/o ATCFT (a=1.1 Re, e=0.01, i=0 to 75 deg)

for 6 trial cases where the semi-major axis and eccentricity were held constant at 1.1 Re (approximately 560 km of orbital altitude at perigee) and 0.01, respectively, and inclination was varied between 0 and 90 degrees. The table that ensues it explicitly details pertinent numerical statistics from the trial runs.

All plots within Figure 32 show reasonably good fits, with the possible exception of the error plot in the 60-degree inclined orbit. The progression of the error within the plots shows that the level of goodness of fit decreases as inclination increases. For inclinations at or below 30 degrees, the maximum residuals are less than 5 meters in each axis over a 1-year time span. Further, the pattern in the residuals is mostly unremarkable, with the exception that only the 0-degree inclination plot shows the stereotypical bow-tie shape seen in research by Wiesel [99]. At 45 degrees, the goodness of the fit begins to degenerate as maximum residuals increase to about 40 meters in each axis. While the residuals have an oscillatory appearance similar to the plots that precede it, they have grown and have taken on a more banded shape. As with all oscillatory behavior, this can be attributed to very small portions of the periodic motion being left in the data after decomposition. The increasing size of the residuals

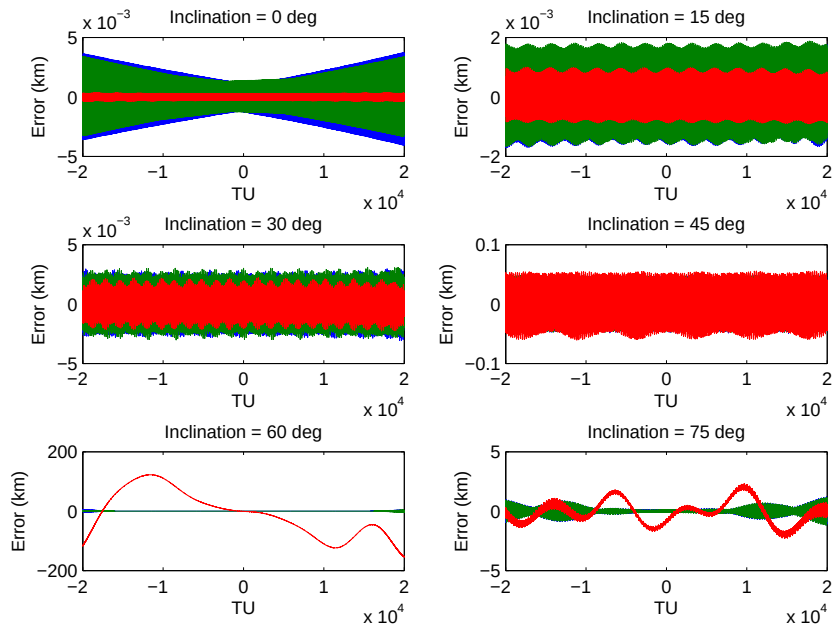

Figure 32. Error Survey (a=1.1 Re, e=0.01, i=0 to 75 deg)

Table 6. Summary of Trial Cases (a=1.1 Re, e=0.01, i=0 to 75 degrees)

Case	a (Re)	e	i (deg)	Basis Set (Rad/TU)	Max Error (meters)	1-D RMS Error (meters)
1	1.1	0.01	0	Ω_1=0.868006065429995 Ω_2=0.060008079780628 Ω_3=0.002350561816056	X=3.73 Y=3.41 Z=0.33	X=1.10 Y=1.13 Z=0.14
2	1.1	0.01	15	Ω_1=0.868008202046348 Ω_2=0.059965932900325 Ω_3=0.002148576472305	X=1.76 Y=1.87 Z=1.00	X=0.51 Y=0.54 Z=0.29
3	1.1	0.01	30	Ω_1=0.868008706206516 Ω_2=0.059847029822424 Ω_3=0.001608600149032	X=2.97 Y=3.08 Z=2.21	X=1.08 Y=1.09 Z=0.60
4	1.1	0.01	45	Ω_1=0.868009213741721 Ω_2=0.059659597133327 Ω_3=8.752517516733697e-004	X=49.33 Y=48.32 Z=55.61	X=24.74 Y=24.69 Z=24.79
5	1.1	0.01	60	Ω_1=0.868006240052059 Ω_2=0.059417406561384 Ω_3=1.476456155861873e-004	X=5,517.84 Y=3,948.49 Z=122,680.44	X=609.25 Y=390.24 Z=75,425.12
6	1.1	0.01	75	Ω_1=0.868007112295149 Ω_2=0.059135624578010 Ω_3=-3.886383249492136e-04	X=1,203.54 Y=1,147.69 Z=2,289.83	X=202.66 Y=202.09 Z=966.74

is mostly due to the NAFF-like algorithm's inability to precisely converge on all frequencies, where Ω_3's steady decrease in size is the primary contributor. Inclinations for 60 and 75 degrees support this assertion. At 60 degrees, the spectral peak at Ω_3 is pushing the boundaries of detectability by the Fourier transform method and as such, the NAFF-like algorithm has not fully converged on it. The result is only a partial extraction of Ω_3 from the data. This causes the large, oscillatory behavior in the Z-axis. Since Ω_3 is most prominent from a power perspective in the Z-axis, the error is most pronounced there. Fortunately, Ω_3 has been estimated rather precisely through a least squares fit of faster frequencies of which it is a part of within the data, thus the decomposition algorithm is working with a much better estimate of Ω_3 than the Fourier transform is showing at the primary Ω_3 occurrence in the spectral plot. Consequently, all other faster combinations of the basis set are decomposed from the data more cleanly than this primary spectral line and this explains why the rest of the fit is rather precise. Once inclination is increased to 75 degrees, the goodness of the fit is increased as the third basis frequency has grown to a more manageable magnitude. In general, Figure 32 shows that trajectory following methods attain considerably better success at lower inclinations, or at least those inclinations that stay clear of the critical inclination.

Figure 33 shows a residual summary for 6 trial cases where the inclination and eccentricity were held constant at 0 degrees and 0.01, respectively, while the semi-major axis was varied between 1.1 and 1.6 Re, the latter of which is approximately 3,700 km at perigee. Table 7 summarizes the most important numerical results in tabular form. Generally speaking, every case shows reasonable results. Similar to the previous batch of trials, as one parameter is increased, the overall goodness of the fit decreases. While the larger semi-major axis cases have kilometer-level maximum error in each axis, the maximum error grows somewhat gracefully as the semi-major

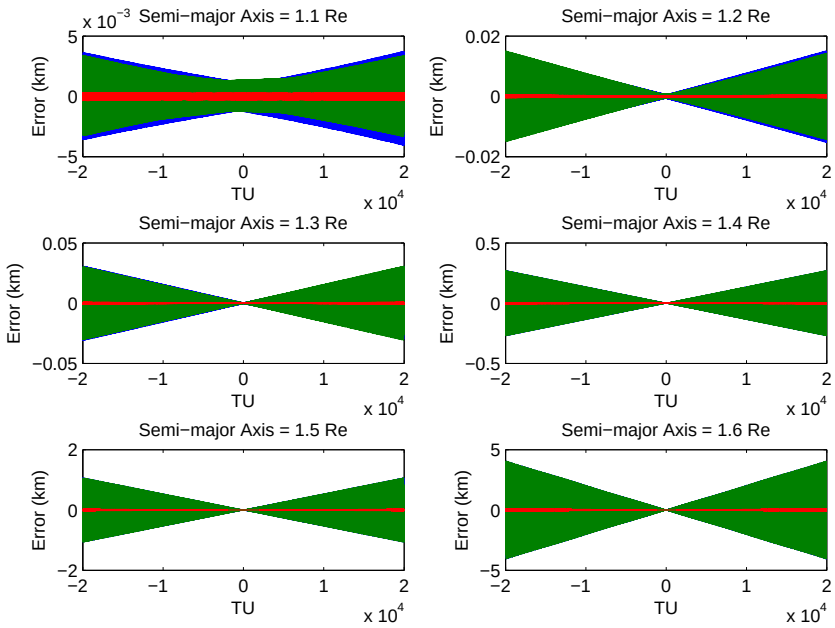

Figure 33. Error Survey (e=0.01, i=0 deg, a=1.1 to 1.6 Re)

Table 7. Summary of Trial Cases (i=0 degrees, e=0.01, a=1.1 to 1.6 Re)

Case	a (Re)	e	i (deg)	Basis Set (Rad/TU)	Max Error (meters)	1-D RMS Error (meters)
1	1.1	0.01	0	Ω_1=0.868006065429995 Ω_2=0.060008079780628 Ω_3=0.002350561816056	X=3.73 Y=3.41 Z=0.33	X=1.10 Y=1.13 Z=0.14
7	1.2	0.01	0	Ω_1=0.761626058424621 Ω_2=0.059697733797664 Ω_3=0.001729263976583	X=15.02 Y=15.06 Z=0.50	X=5.18 Y=5.18 Z=0.16
8	1.3	0.01	0	Ω_1=0.675339653904806 Ω_2=0.059485710677935 Ω_3=0.001304862747450	X=30.84 Y=30.79 Z=0.80	X=10.90 Y=10.90 Z=0.30
9	1.4	0.01	0	Ω_1=0.604205491017837 Ω_2=0.059336276385856 Ω_3=0.001005760994372	X=270.84 Y=270.43 Z=6.14	X=96.94 Y=96.94 Z=2.53
10	1.5	0.01	0	Ω_1=0.544742275076789 Ω_2=0.059227996330794 Ω_3=7.891859990634381e-004	X=1,063.52 Y=1,066.24 Z=24.66	X=379.91 Y=379.91 Z=10.10
11	1.6	0.01	0	Ω_1=0.494433849509274 Ω_2=0.059147719741224 Ω_3=6.287877665364505e-004	X=4,044.30 Y=4,047.84 Z=93.37	X=1,455.43 Y=1,455.45 Z=38.00

axis increases. Since the orbital motion resides very close to the x-y plane due to the inclination of these orbits, any error in the z-axis caused by a shrinking Ω_3 will be contained to the maximum out-of-plane motion. Since the inclination is zero, this motion is minimal. The increasing size of the linear growth of the residuals in the X and Y axes is attributable to error in the a priori estimates of the basis frequencies when compared to what is present in the spectral plot, with Ω_3 being the worst again. Thus, spectral methods are more successful at higher altitudes if the inclination is kept lower. This is not surprising as Figure 28.1 implies this.

Figure 34 shows a residual summary for 6 trial cases where the inclination and eccentricity were held constant at 30 degrees and 0.01, respectively, while the semi-major axis was once again varied between 1.1 and 1.6 earth radii. Table 8 summarizes the specific numerics implied by the plots. The results are somewhat surprising in the fact that it shows that orbits with inclinations of 30 degrees generally have better overall fits than those at 0 degrees, which the preceding set of trials seemed to suggest would not be the case. While the error in the X and Y axes has improved in all cases, the error in the Z axis has not. The relative smallness of Ω_3 is very much evident in this axis by the appearance of the larger oscillatory envelope of the error residuals.

4.4 Least Squares Fit of Frequency Clusters

Decomposition by frequency clusters using the method of least squares is a few steps more complicated than the method presented earlier using the windowed ATCFT to set up a linear system of equations. Fortunately, these steps are simplified as most of the work has been previously done in this research for other reasons. Since the analytical expressions for the windowed ATCFT have already been obtained, all that remains is to place these analytical forms into the shell of the linear least squares algorithm from Section 3.5.1.

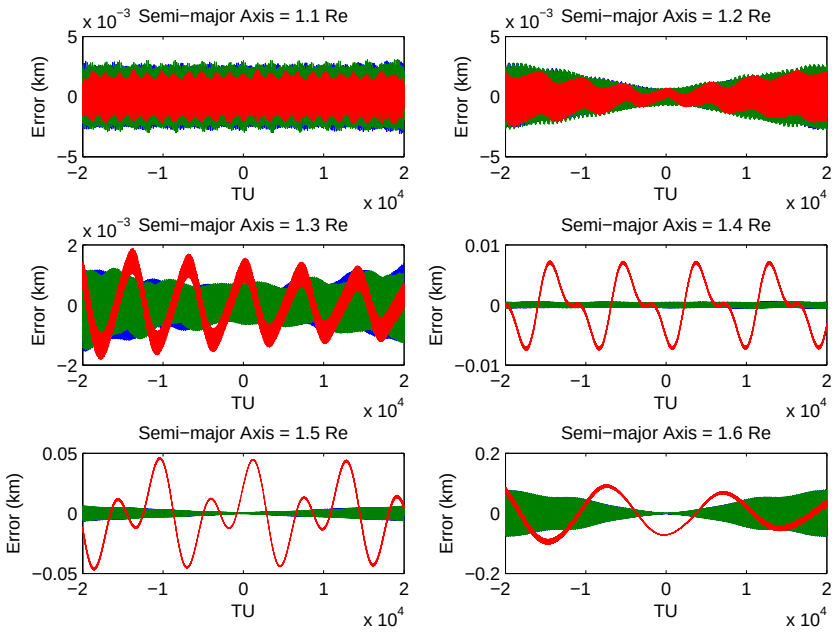

Figure 34. Error Survey (e=0.01, i=30 deg, a=1.1 to 1.6 Re)

Table 8. Summary of Trial Cases (i=30 degrees, e=0.01, a=1.1 to 1.6 Re)

Case	a (Re)	e	i (deg)	Basis Set (Rad/TU)	Max Error (meters)	1-D RMS Error (meters)
3	1.1	0.01	30	Ω_1=0.868008706206516 Ω_2=0.059847029822424 Ω_3=0.001608600149032	X=2.97 Y=3.08 Z=2.21	X=1.08 Y=1.09 Z=0.60
12	1.2	0.01	30	Ω_1=0.761627233324643 Ω_2=0.059580248613905 Ω_3=0.001185221743670	X=2.79 Y=2.78 Z=2.17	X=0.56 Y=0.59 Z=0.50
13	1.3	0.01	30	Ω_1=0.675340273632188 Ω_2=0.059397404517079 Ω_3=8.950332210211098e-004	X=1.37 Y=1.23 Z=1.87	X=0.33 Y=0.33 Z=0.79
14	1.4	0.01	30	Ω_1=0.604205859549051 Ω_2=0.059268341377315 Ω_3=6.901824242152189e-004	X=0.62 Y=0.59 Z=7.34	X=0.16 Y=0.16 Z=4.31
15	1.5	0.01	30	Ω_1=0.544742464009994 Ω_2=0.059174917478387 Ω_3=5.418847913191727e-004	X=6.20 Y=6.17 Z=46.22	X=1.83 Y=1.81 Z=25.38
16	1.6	0.01	30	Ω_1=0.494433844857701 Ω_2=0.059105803639924 Ω_3=4.321932732089173e-004	X=77.70 Y=77.08 Z=94.50	X=24.80 Y=24.79 Z=52.77

Recall from the previous chapter that the estimate of the state, and the solution to the minimization problem, at epoch is:

$$\hat{\mathbf{x}}(t_o) = (H^T H)^{-1} H^T \mathbf{z} \tag{109}$$

$$= P_{\hat{\mathbf{x}}}(t_o) H^T \mathbf{z}, \tag{110}$$

where $P_{\hat{\mathbf{x}}}(t_o)$ is the state covariance matrix at epoch. To obtain the solution to Equation 109 for the state vector of Fourier coefficients, several key pieces needed to be assembled: a set of sampled data, a linear transformation to map the states to the sampled data, and an a priori estimate of the basis frequencies to be used by this linear mapping. The basis frequencies are already estimated by Fourier analysis, thus the only pieces that required development were the linear mapping between the states and the form of the data used in the fitting process. Recall the observation relationship (or linear mapping) is defined generically as:

$$\mathbf{z}_i(t_i) = H_i \mathbf{x}(t_i), \tag{111}$$

where H_i is the linear transformation matrix between the states (i.e. Fourier coefficients) and the measurements. Under the premise that the windowed ATCFT is the observation relationship, its linear map to the states can be found by by creating a matrix of partial derivatives of the windowed ATCFT. Since the windowed ATCFT is linear in the coefficients, a partial derivative matrix with respect to the states looks very similar to the matrix of coefficients, A, developed in the last section. The only difference here is the that the estimator is processing just the Fourier transform at one specific spectral line (albeit both its imaginary and real parts) rather than the Fourier transform at every spectral line of a frequency cluster. Thus, the top two

rows of the matrix of coefficients can be leveraged to build the linear mapping for one measurement incorporation by the least squares estimator. Under this paradigm, the linear mapping, H_{Coef}, for every data point, i, can quickly formed by using the notation used previously:

$$H_{Coef} = \begin{bmatrix} \Re(\mathcal{K}_{[\omega_i]_{wrt\ \Psi_1}}) & \cdots & \Re(\mathcal{K}_{[\omega_i]_{wrt\ \Psi_n}}) \\ \Im(\mathcal{K}_{[\omega_i]_{wrt\ \Psi_1}}) & \cdots & \Im(\mathcal{K}_{[\omega_i]_{wrt\ \Psi_n}}) \end{bmatrix}, \tag{112}$$

where n is the number of frequencies in the current cluster being fitted and ω_i is the frequency corresponding to the current data point being processed. As it has already been alluded, the data used for fitting the windowed ATCFT were selected values from the Fourier transform of the orbital data. Similar to that of Palma and Echave, 5 points per transform peak were found to be sufficient to fit the peak in question [85]. These points were selected at equally spaced points on the transform within the intervals of $\Psi_k \pm \frac{\pi}{2T}$, where k is the particular integer combination of the basis set being fit and T is the half-interval of the data sample. Larger intervals were used, but this interval yielded the best results.

The rest of this method follows as the cluster frequency decomposition using spectral lines did. Once a cluster's coefficients are solved for, their contributions to the periodic motion is extracted from the data similar to that done in Section 3.4.2. Further, the clusters are processed in order of magnitude, largest to smallest, as to minimize effects from neighboring clusters' shoulders. This process is repeated until desired accuracy in the fit is achieved.

4.4.1 Survey of Results.

The least squares cluster decomposition algorithm was applied to the same year-long orbit samples within the LEO belt used for the line-based frequency cluster

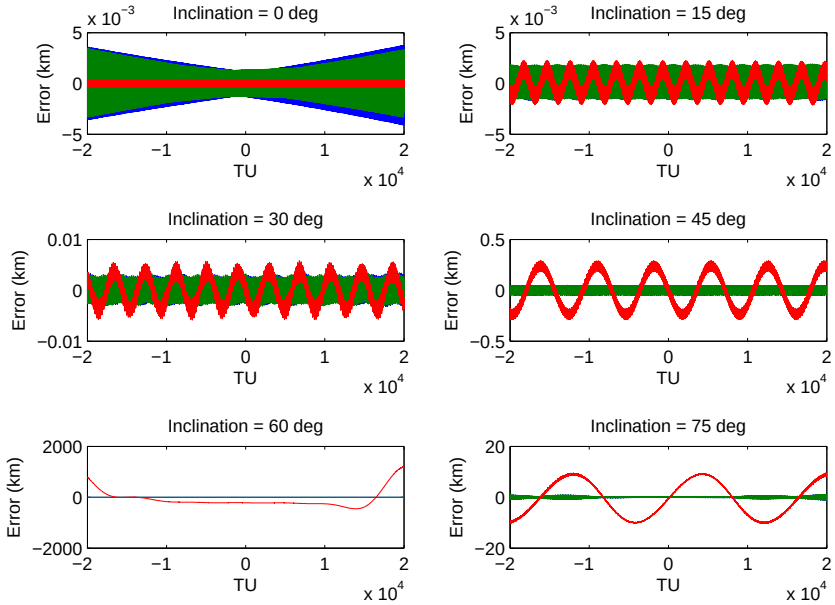

Figure 35. Error Survey (a=1.1 Re, e=0.01, i=0 to 75 deg)

Table 9. Summary of Trial Cases (a=1.1 Re, e=0.01, i=0 to 75 deg)

Case	a (Re)	e	i (deg)	Basis Set (Rad/TU)	Max Error (meters)	1-D RMS Error (meters)
1	1.1	0.01	0	Ω_1=0.868006065429995 Ω_2=0.060008079780628 Ω_3=0.002350561816056	X=3.75 Y=3.42 Z=0.33	X=1.10 Y=1.12 Z=0.14
2	1.1	0.01	15	Ω_1=0.868008202046348 Ω_2=0.059965932900325 Ω_3=0.002148576472305	X=1.82 Y=1.92 Z=2.25	X=0.51 Y=0.54 Z=0.98
3	1.1	0.01	30	Ω_1=0.868008706206516 Ω_2=0.059847029822424 Ω_3=0.001608600149032	X=3.41 Y=3.41 Z=5.80	X=1.12 Y=1.13 Z=2.70
4	1.1	0.01	45	Ω_1=0.868009213741721 Ω_2=0.059659597133327 Ω_3=8.752517516733697e-004	X=49.27 Y=47.82 Z=290.32	X=24.74 Y=24.70 Z=170.33
5	1.1	0.01	60	Ω_1=0.868006240052059 Ω_2=0.059417406561384 Ω_3=1.476456155861873e-004	X=188.62 Y=163.65 Z=1,206,320.59	X=160.40 Y=156.62 Z=334,623.14
6	1.1	0.01	75	Ω_1=0.868007112295149 Ω_2=0.059135624578010 Ω_3=-3.886383249492136e-04	X=1,177.30 Y=1,123.38 Z=9,438.77	X=203.77 Y=203.49 Z=6,683.32

method so that both methods could be compared side by side. Figure 35 and Table 9 show an error summary for 6 trial cases where the semi-major axis and eccentricity were held constant at 1.1 Re (approximately 560 km of orbital altitude at perigee) and 0.01, respectively, and the inclination was varied between 0 and 90 degrees. As with the line-based method, the level of goodness in the fit does decrease as inclination increases towards the critical inclination. After that point, the error once again decreases. In general, the plots show that the least squares method has greater error residuals than the line-based method when each trial case is compared, except the very first scenario where the inclination is zero. In this first trial, the performance of the least squares and line-based methods are nearly the same. A noteworthy pattern is also noticeable in the Z-axis for lower inclinations in the least squares method's results. As the plot of the error from the 60-degree-inclined orbit demonstrates, this Z-axis error is considerably greater than that seen previously with the line-based method. This poor Z-axis behavior, as before, is due to the incomplete decomposition of the main Ω_3 harmonic in this axis. A closer inspection of pre- and post-Fourier transforms confirms this assertion. These plots and their corresponding analysis will be presented at the conclusion of this section so that it can be discussed in context of all trial cases accomplished. In summary, Figure 35 shows that the least-squares-based trajectory following methods attain considerably better success at very low inclinations. If more data (in terms of time span) can be taken, then higher inclinations can be used with results similar to that of the line-based method.

Figure 36 and Table 10 show a residual summary for 6 trial cases where the inclination and eccentricity were held constant at 0 degrees and 0.01, respectively, and the semi-major axis was varied between 1.1 and 1.6 earth radii, the latter of which is approximately 3,700 km at perigee. As with the previous series of trials, as one parameter is increased, the overall goodness of the fit decreases. However, unlike

the previous trials with the least squares method, these results are nearly identical to that of the line-based method. This further confirms the assertion that the decrease in size of Ω_3 is the primary offender in the large, oscillatory error behavior. Once again we see here that since the inclination is zero, the minimal out-of-plane motion of the orbit contains the error in the Z axis. As usual though, the increasing size of the linear growth of the residuals in the X and Y axes is attributable to error in the estimates of the basis frequencies.

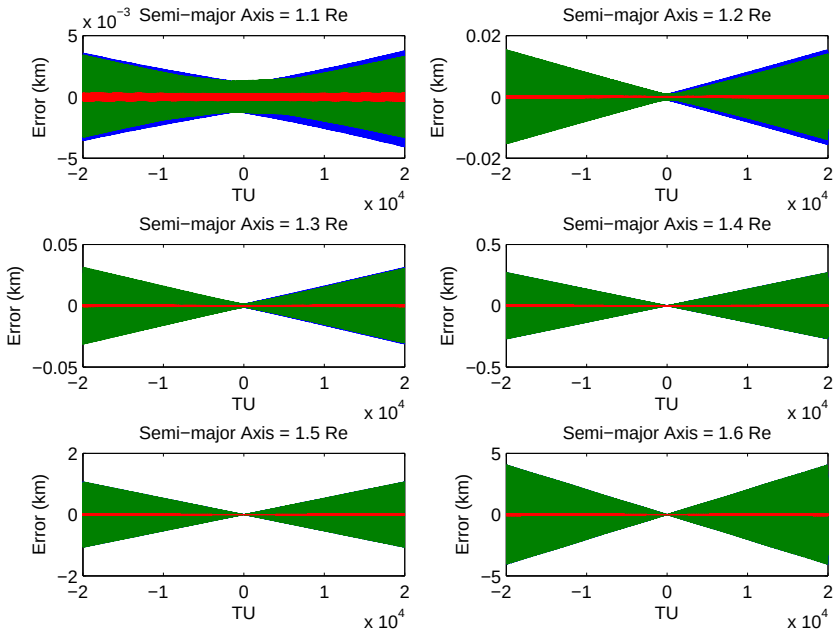

Figure 36. Error Survey (e=0.01, i=0 deg, a=1.1 to 1.6 Re)

Finally, Figure 37 and Table 11 show an error summary for 6 trial cases where the inclination and eccentricity were held constant at 30 degrees and 0.01, respectively, and the semi-major axis was once again varied between 1.1 and 1.6 Re. This figure shows the same general trends that the other least squares method error plots have shown. As inclination and semi-major axis increase, the error in the fit grows much more rapidly than as seen in the line-based method. Once again, this can be tied to the size of Ω_3 and its poor decomposition from the orbital data.

Table 10. Summary of Trial Cases (e=0.01, i=0 deg, a=1.1 to 1.6 Re)

Case	a (Re)	e	i (deg)	Basis Set (Rad/TU)	Max Error (meters)	1-D RMS Error (meters)
1	1.1	0.01	0	Ω_1=0.868006065429995 Ω_2=0.060008079780628 Ω_3=0.002350561816056	X=3.73 Y=3.41 Z=0.33	X=1.10 Y=1.13 Z=0.14
7	1.2	0.01	0	Ω_1=0.761626058424621 Ω_2=0.059697733797664 Ω_3=0.001729263976583	X=15.32 Y=15.36 Z=0.50	X=5.19 Y=5.19 Z=0.16
8	1.3	0.01	0	Ω_1=0.675339653904806 Ω_2=0.059485710677935 Ω_3=0.001304862747450	X=31.24 Y=31.20 Z=0.81	X=11.03 Y=11.03 Z=0.30
9	1.4	0.01	0	Ω_1=0.604205491017837 Ω_2=0.059336276385856 Ω_3=0.001005760994372	X=270.29 Y=271.10 Z=6.17	X=96.94 Y=96.94 Z=2.53
10	1.5	0.01	0	Ω_1=0.544742275076789 Ω_2=0.059227996330794 Ω_3=7.891859990634381e-004	X=1,064.30 Y=1,067.02 Z=24.66	X=380.28 Y=380.28 Z=10.10
11	1.6	0.01	0	Ω_1=0.494433849509274 Ω_2=0.059147719741224 Ω_3=6.287877665364505e-004	X=4,045.04 Y=4,047.04 Z=93.37	X=1,455.46 Y=1,455.47 Z=38.01

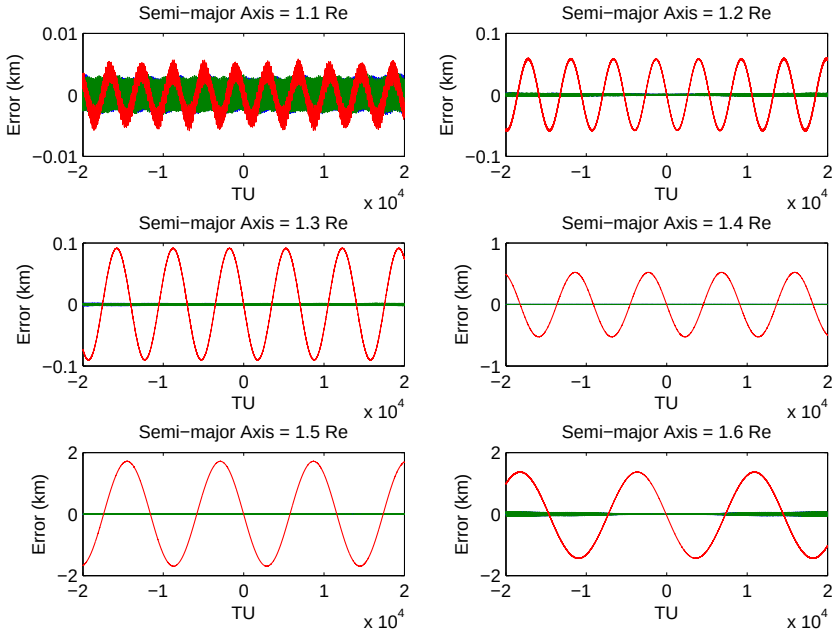

Figure 37. Error Summary (e=0.01, i=30 deg, a=1.1 to 1.6 Re)

Table 11. Summary of Trial Cases (e=0.01, i=30 deg, a=1.1 to 1.6 Re)

Case	a (Re)	e	i (deg)	Basis Set (Rad/TU)	Max Error (meters)	1-D RMS Error (meters)
3	1.1	0.01	30	Ω_1=0.868008706206516 Ω_2=0.059847029822424 Ω_3=0.001608600149032	X=3.41 Y=3.41 Z=5.80	X=1.12 Y=1.13 Z=2.70
12	1.2	0.01	30	Ω_1=0.761627233324643 Ω_2=0.059580248613905 Ω_3=0.001185221743670	X=3.29 Y=3.19 Z=60.10	X=0.66 Y=0.69 Z=41.03
13	1.3	0.01	30	Ω_1=0.675340273632188 Ω_2=0.059397404517079 Ω_3=8.950332210211098e-004	X=2.14 Y=2.01 Z=91.63	X=0.80 Y=0.78 Z=64.95
14	1.4	0.01	30	Ω_1=0.604205859549051 Ω_2=0.059268341377315 Ω_3=6.901824242152189e-004	X=1.40 Y=1.47 Z=521.74	X=0.64 Y=0.67 Z=366.38
15	1.5	0.01	30	Ω_1=0.544742464009994 Ω_2=0.059174917478387 Ω_3=5.418847913191727e-004	X=6.83 Y=7.03 Z=1,717.04	X=1.99 Y=2.00 Z=1,196.72
16	1.6	0.01	30	Ω_1=0.494433844857701 Ω_2=0.059105803639924 Ω_3=4.321932732089173e-004	X=76.26 Y=75.61 Z=1,376.53	X=24.70 Y=24.71 Z=1,020.48

In all least squares trial cases discussed previously, the common theme in explaining the larger residuals was an Ω_3 that was too small for the algorithm to successfully handle given the time span of the data used. Specifically, an insufficient number of periods of Ω_3 were present within the test case data for the NAFF-like algorithm to converge with enough precision on the signal's low-frequency content such that a majority of the signal at those frequencies was decomposed. Figure 38 compares the pre- and post-transforms of a portion of the spectrum in the X- and Z-axis for one particular orbit (a=1.2 Re, e=0.01 and i=30 degrees) using both the line-based and least squares decomposition methods. Each plot shows the peak at zero frequency plus one or more harmonics of Ω_3, with the smallest non-zero frequency peak being the primary harmonic. For the X-axis, both methods reduce the maximum power in the leftover signal at the frequencies of interest about the same. However, the least squares method does a much better job in removing the contributions from frequencies above the first harmonic. Figures 38.1 and 38.3 show how the line-based method leaves false, residual peaks due to slight differences in the basis frequency being used in the decomposition process versus what is being converged upon in the transform. This is similar to what was seen with GPS data in the previous chapter. Regardless, the power in the leftover primary harmonic of Ω_3 in the X-axis corresponds to error at or below the meter-level. On the other hand, Figures 38.2 and 38.4 show that the least squares method leaves considerable amount of the signal at the primary occurrence of Ω_3 after decomposition. The magnitude of the leftover signal is on the order of $10 \times 10{-}05$, which translates to roughly error in the tens or hundreds of meters. Figure 36 shows how this error in the Fourier transform translates to the frequency domain in the form of error in the fit. The error plot in question is the one that corresponds to the 30-degree-inclined orbit. As expected, the plot's maximum error in the Z-axis residuals is about 60 *meters*. One way to overcome this poor

decomposition effect, is to increase the time period of the data collection.

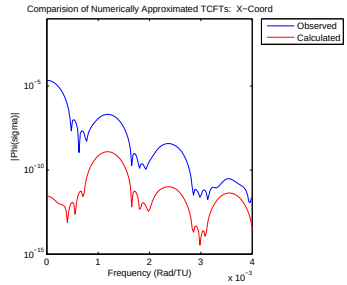

38.1: Line-Based - X-axis

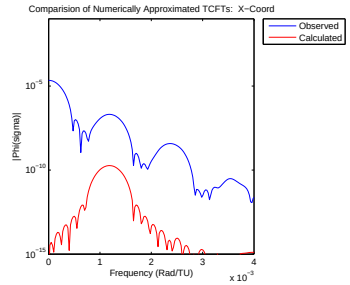

38.2: Least Squares - X-axis

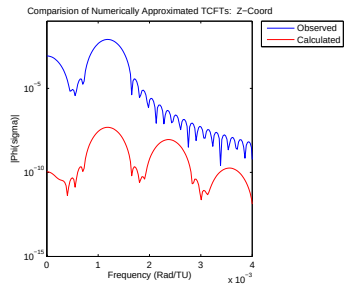

38.3: Line-Based - Z-axis

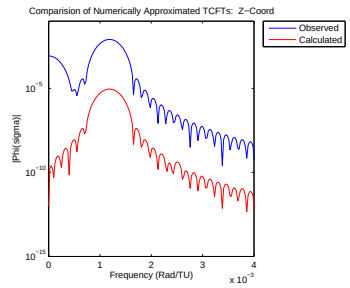

38.4: Least Squares - Z-axis

Figure 38. Fourier Transform Snippet Comparison

Since a only a small number of the lowest, low-frequency coefficients were significantly different between the two methods, another approach to overcome the poor decomposition of Ω_3 was thought to be an optimization method to *correct* those coefficients. Thus, a simulated annealing algorithm was developed to search for a global minimum in the fit of the poorly resolved least squares coefficients. Simulated annealing is a good candidate for this type of optimization problem as the number of unknowns are small, the solution space appears to have multiple local minima, and we have a relatively good guess on the coefficients already. This idea is explored in the next section.

4.5 Low-Frequency Coefficient Correction by Simulated Annealing

Simulated annealing (SA) is a global optimization method using a computational stochastic algorithm [61]. As such, it searches a solution space by randomly altering its current estimate of the global minimizing solution and comparing the new cost of this solution to that of the current solution. Depending on the cost and if necessary, the corresponding value of a probability distribution describing the risk of accepting a solution with a higher cost at the benefit of escaping a local minima in favor of a global, this step is either rejected or accepted. At higher energy levels, the probability of leaving a current state for another of higher cost is much greater than that at lower energies. In fact, as the algorithm approaches its terminal iteration, the probability function favors low-energy solutions and the algorithm essentially becomes a gradient decent method.

4.5.1 Simulated Annealing Algorithm.

The shell of the SA method is very simple. While the internal details do add complexity, they only do so as much as the implementer desires or the problem requires. The latter is usually driven by convergence issues. Like most optimization methods, SA is a systematic process. Only when the specifics of the optimization problem are included does the algorithm take on a more ad hoc flavor. This research used the core of the the SA model by Yang [105] as its skeleton. Specifically, the algorithms steps are:

1. Define an a priori estimate, $\mathbf{x}_c$, as the best estimate,$\mathbf{x}_o$. Determine the cost, $\mathbf{J}_c$, of this estimate and denote it $\mathbf{J}_o$.

2. Define a subset, $\mathbf{S}$, of the general solution space, $\mathbf{G}$, where the algorithm will confine itself.

3. Begin a loop on k, where $k = (1, 2, \ldots, k_{max})$.

4. Establish a new best estimate, $\mathbf{x}_k$, by taking a random step within the solution space such that $\mathbf{x}_k \in \mathbf{S}$. In order to make the random step as efficient as possible, it is constrained by the boundaries of the set $\mathbf{S}$, the current synthetic energy (or temperature) of the system, and the inverse μ-law:

$$F^{-1}(y) = sgn(y)\frac{(1+\mu)^{|y|} - 1}{\mu}, \tag{113}$$

where $\mathbf{y}$ is a random number vector of the same dimension as $\mathbf{x}_c$ selected from a uniform distribution on $[-1, 1]$ and μ is governed by:

$$\mu = 10^{100T^{-1}}, \tag{114}$$

where T is the current synthetic temperature. Thus, to obtain the random step, the random vector $\mathbf{y}$ is transformed by Equation 113 and then the result is subsequently multiplied by the difference in the upper and lower bounds of $\mathbf{S}$ for each corresponding element of $\mathbf{x}_c$. Should the new $\mathbf{x}_k$ not be an element of $\mathbf{S}$, the offending elements are lowered/raised to the boundary of $\mathbf{S}$ so that the constraints are not violated.

5. Evaluate the new cost, $\mathbf{J}_k$.

6. If $\Delta\mathbf{J} = \mathbf{J}_k - \mathbf{J}_c < 0$, let $\mathbf{x}_k$ become $\mathbf{x}_c$ and if $\mathbf{J}_k < \mathbf{J}_o$, then $\mathbf{x}_k$ and $\mathbf{J}_k$ become $\mathbf{x}_o$ and $\mathbf{J}_o$, respectively. However, if $\Delta\mathbf{J} \geq 0$, select a random number, n, from a uniform probability distribution on $[0, 1]$ and if:

$$n < f(\mathbf{J}_k, \mathbf{J}_c, T) = exp\left(-\frac{\Delta J}{T}\right), \tag{115}$$

let $\mathbf{x}_k$ become $\mathbf{x}_c$, where $f(\mathbf{J}_k, \mathbf{J}_c, T)$ is the Metropolis function [74] describing the probability of accepting a random step in the solution space.

7. Increment k and repeat algorithm from the random step and continue until k_{max}.

8. When $k = k_{max}$, the estimate $\mathbf{x}_o$ becomes the claimed global minimizing solution with associated cost, $\mathbf{J}_o$.

4.5.2 Selection of Simulated Annealing Parameters.

To this point, the SA algorithm has been non-specific to any given optimization problem. However, there are no universal choices for the cost function, temperature profile, quenching factor and iteration length since they are usually problem dependent. Unfortunately, there is no standard procedure to develop or select any of these pieces of the algorithm. While there may be some common choices with which to begin the design process, their ultimate selection is somewhat ad hoc and is based on engineering judgement and experience. Each of these definable quantities will be described here as well as their chosen forms or values.

Generally speaking, a temperature profile for any SA algorithm will start at some very high temperature and end at zero. What happens in between is up to the designer, and must be chosen carefully as the temperature profile is very important. Under a given iteration limit, keeping temperatures too high for too long may cause the SA algorithm to bounce away from a global solution while the opposite may cause it to never leave a locally minimizing solution. Temperature profiles can be as simple as a predetermined cooling schedule or as complex as one that dynamically controls the temperature such that system is kept in a pseudo-thermodynamic equilibrium. For this problem, the temperature profile was chosen to be an a priori temperature profile given by:

$$T^{-1} = \left(\frac{k}{k_{max}}\right)^q, \tag{116}$$

where k is the current iteration, k_{max} is the maximum iteration, and q is the quenching factor. The quenching factor is real number greater than zero. High q values result in very quick quenching, while low values yield the opposite. Initial efforts have found success with $q = 1$.

Outside of the temperature profile, selection of the cost function is probably the most important step in designing the algorithm. The cost function needs to represent an entity that needs to be minimized in the problem while at the same time sufficiently describing the totality of the model. For example, total error would more than likely be a better choice than maximum error. While a cost function for a given problem certainly is not unique, some make more sense than others depending on what is being minimized. The cost function used here was a that of a simple quadratic cost of the form:

$$J = \frac{1}{2}\sum_{i=1}^{n}(X_i - x_i)^2, \tag{117}$$

where X is "observed" orbital data, x is the estimated orbital data, and n is the number observation samples. Obviously, this is the common cost function from least squares used previously, the sum of the square of the residuals. While this is an effective and logical choice for a cost function, a drawback of it is the time required to transform the parameters (i.e Fourier coefficients) from the frequency domain to the time domain (i.e. orbital observations in the rotating frame) for each iteration of the optimization routine. Regardless of its mechanization drawbacks, it is important to note that the implementer has no care of the analytic or topographical attributes of the cost function are as only the value of it is needed by the SA algorithm.

The last user-selectable parameter left is that of algorithm iteration length. Iteration length is important as it may have an affect on the temperature profile (as it does here) but is also dictates how much of the solution space the algorithm is allowed to wander through. It has been shown by Granville et al [42] that as the iteration length is increased, the probability that the SA algorithm will converge upon the global solution approaches unity. However, this is obviously impractical. Thus, a starting point should be chosen and then adjusted as necessary. This holds true for all of the user-defined quantities discussed here. Should one particular set not work, all or some may need to be modified to allow for successful convergence of the algorithm within a reasonable amount of time. Fortunately, results within this research were found only after a few permutations.

4.5.3 Example of Results.

The preceding SA algorithm was implemented with excellent results. Succinctly stated, the SA algorithm successfully corrected the low frequency coefficients such that the overall residual profile of the orbital torus fit was nearly identical to that of the line-based frequency cluster method. This result not only validates the previous results obtained but also highlights how effective the modified Laskar method is in suppressing sidelobe information while still allowing for acceptable frequency determination. Figure 39 shows some of the results obtained. It shows the error in the fit from Case 4 for three different fitting methods: the frequency cluster approach, the least squares approach, and the least squares approach with coefficient correction by simulated annealing. The plot of the error in the fit clearly shows that the low-frequency oscillation in the least squares residuals has been removed and that the frequency cluster and simulated annealing approaches are now nearly identical from a performance perspective.

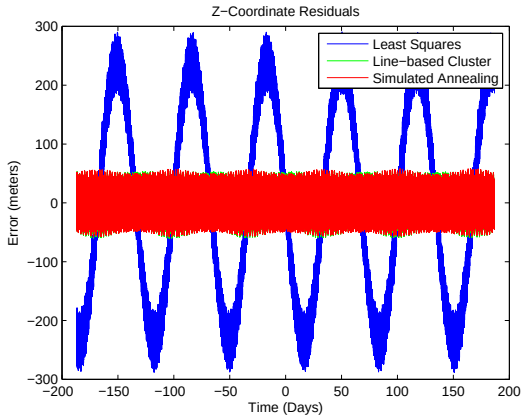

Figure 39. Comparison of Fitting Methods, Z-axis Residuals

4.6 Compare and Contrast Cluster-Based Methods

While the least squares method with coefficient correction may achieve better results than the lined-based frequency cluster method after further modifications of the SA algorithm (especially if the more coefficients are allowed to be "corrected"), the computational cost is not worth the marginal improvement in performance as the line-based method obtains similar performance in a fraction of the time. This is testament to the quality of the estimate of the basis set done prior to decomposition. Further, it shows that the Hann window order was wisely chosen as slight differences in the frequency used during decomposition with the line-based method does not drastically affect coefficient determination. The true benefit of the least squares method may be seen as the data used by the decomposition algorithm becomes corrupted with perturbations and noise, as found in real-world data. Further, higher-order Hann windows may prove beneficial as the performance envelope is pushed to higher altitudes, but no efforts to date have successfully mitigated the small divisors encountered with Hann windows above order 2.

4.7 Orbit Prediction Example with Geopotential Only

Thus far, only the initial fits of the orbital tori have been analyzed and presented, however for this concept to be useful, its effectiveness in predicting future ephemerides must be assessed. Of course, the basic assumption of this research is that earth orbital tori are invariant, or at least nearly invariant on operational timescales. Thus, the application of the calculated estimate of the torus to future orbital data should produce error in its fit on the order of the fits obtained during the initial fitting process. If not, the assumption of invariance is poor and the orbital tori concept would be in jeopardy. To test the period of validity of an orbital torus estimate, a sample orbit determination problem of real-world significance was undertaken. In particular, the Hubble Space Telescope (HST) was analyzed.

A NORAD two line element set from 18 February 2010 was used as the reference orbit. As with the preceding analysis, the initial conditions were used within a Hamming numerical integrator to create a 1-year sample of orbital position data. The time step within the data was 0.05 TU. Only the earth's geopotential was used as a source of perturbations. Table 12 shows the basis set that was converged upon.

Table 12. Basis Frequency Set for the HST

Basis Frequency	Value (Rad/15 minutes)
Ω_1	0.880626013433404
Ω_2	0.059897412917959
Ω_3	0.001731861820452

Using this basis set, the line-based cluster decomposition routine was used on the data set. An $\mathbf{M} = (6, 14, 6)$ expansion was accomplished. The results can be seen at Figure 40 with specific numerical results in Table 13. The fit is excellent, with 1-D rms values less than 2 *meters* in each coordinate axis.

The future applicability of the calculated series coefficients and basis set were tested on a 1-year, integrated data sample created by the same integrator used previ-

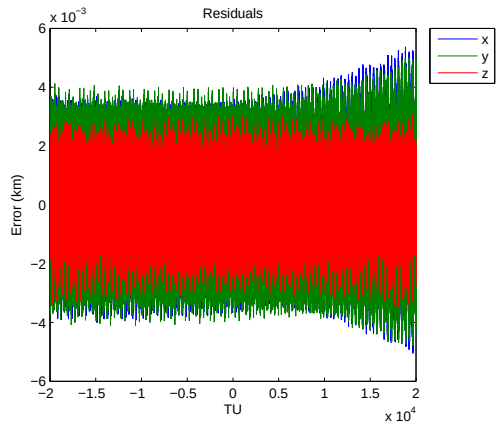

Figure 40. HST Orbital Torus Fit (p=2/$M = (6, 14, 6)$)

Table 13. Summary of HST Orbital Torus Fit

Case	a (Re)	e	i (deg)	Basis Set (Rad/TU)	Max Error (meters)	1-D RMS Error (meters)
HST	1.09	0.0	28.5	Ω_1=0.880626013433404 Ω_2=0.059897412917959 Ω_3=0.001731861820452	X=5.36 Y=4.99 Z=3.07	X=1.77 Y=1.78 Z=0.99

ously. Chronologically speaking, this simulated orbital data was chosen such that it immediately followed the sample data used to fit the orbital torus. An $\mathbf{M} = (6, 14, 6)$ expansion was accomplished using the the line-based cluster decomposition routine. The results can be seen at Figure 41. Table 14 shows associated results in tabular form. The fit once again is excellent.

The results clearly support the assertion that at a minimum, a nearly invariant torus is the resulting motion of a satellite under the influence of the earth's geopotential. The difference between the error in the fit with the error in the predicted

Table 14. Summary of HST Orbital Predication Results

Case	a (Re)	e	i (deg)	Basis Set (Rad/TU)	Max Error (meters)	1-D RMS Error (meters)
HST	1.09	0.0	28.5	Ω_1=0.880626013433404 Ω_2=0.059897412917959 Ω_3=0.001731861820452	X=5.75 Y=5.44 Z=3.16	X=1.82 Y=1.83 Z=0.99

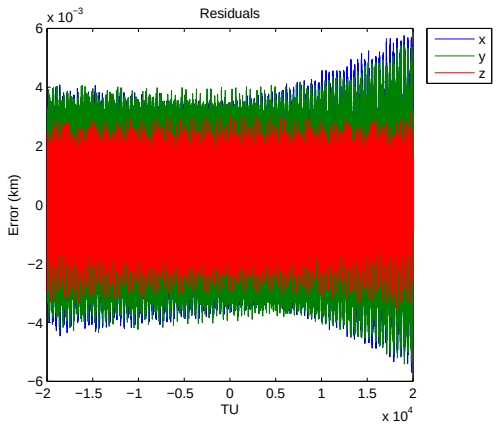

Figure 41. HST Orbital Torus 1-yr Prediction Fit ($M = (6, 14, 6)$)

ephemeris is on the order of a few centimeters in each axis. This small difference can be attributed to small and different section of the torus to find the initial basis set and Fourier coefficients. While the time sample of the orbit was chosen such that each of the basis set had 10 or more revolutions, the motion on the torus is multiply periodic. As such, it never truly repeats due to the incommensurate nature of the basis set. Thus, it should be expected that different torus samples may create slightly different estimates of the basis set and Fourier coefficients. In an operational scenario, the use of a sequential estimation method at this point would make sense, thus allowing the parameters of the orbital torus to be refined over time.

Figure 42 shows the results from a $\mathbf{M} = (6, 20, 6)$, and demonstrates that time and computational power seem to be the only practical limits on how low the error can be reduced as the error in the fit has been reduced by nearly a factor of 2 in each coordinate axis. However, at very large expansions in $\mathbf{M}$, the reduction in error is due more to squeezing out ever-decreasing contributions from the signal that are not necessarily tied to an underlaying toroidal object. While the fit will continue to marginally improve, the increase in fit is done so at unproportionate and unnecessary cost.

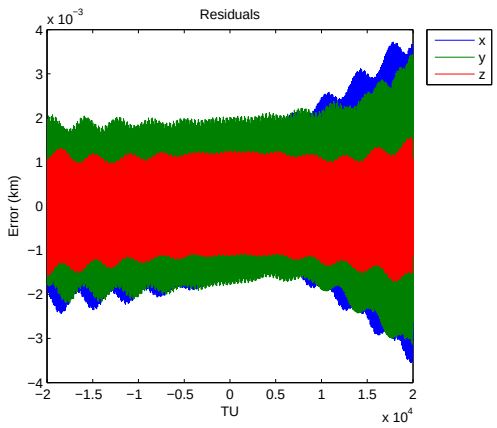

Figure 42. HST Orbital Torus 1-yr Prediction Fit ($M = (6, 20, 6)$)

V. Conclusions

Applying the KAM theory to real-world orbit determination problems is still in its infancy. To date, research has focused on the existence and description of earth orbits as invariant, or at least nearly invariant, KAM tori as well as on a few trajectory following spectral methods. Due to the requirement of precision, long-term data tracks for these methods to produce quality tori fits, alternatives to these methods will ultimately need to be developed. This is especially true for the operational user as real-world satellite mission lifetimes are short-duration and generally require station-keeping maneuvers, both of which make revealing any underlaying toroidal motion difficult. On the other hand, non-operational or non-maneuvering satellites (i.e. those in disposal orbits, miscellaneous space debris, etc.) still may benefit from trajectory following methods. This chapter will summarize some limitations of the trajectory following methods that have been revealed, the results from GPS orbital tori construction efforts, and a review of the frequency cluster decomposition methods developed as a result lessons learned during the GPS portion of this research. Finally, the chapter will conclude with overall conclusions and recommendations for future research.

5.1 Limitations of Trajectory Following Tori Construction Methods

This research has highlighted several limitations of the trajectory following methods. While some were to be expected, others were not. They can be generally summarized as:

- Individual spectral lines cannot be identified when basis frequencies are nearly commensurate when using *practical* timespans.

- Consequences of sampling limitations (similar to that of the Nyquist-Shannon Theorem) prevent precise analysis on any data set where the dominant periodic motion under consideration has less than approximately two complete periods within the data.

- Depending on the orbit and time window used, the basis set may not be converged upon with sufficient precision to be used successfully by trajectory following decomposition methods.

- Prominent spectral peaks within the spectra of an orbital data set have an increased chance of occluding (either partially or completely) nearby, lower-magnitude peaks when using short timespans, when compared to the periods of the basis set.

- In addition to spectral occlusion, nearby spectral peaks nontrivially affect the amplitude height of nearby peaks and should be accounted for when determining the amplitudes of each spectral peak.

- Local minima in the solution space appear to make finding a global minimum for least squares difficult when all coefficients are being determined simultaneously.

- Least squares methods also face challenges inverting sometimes large, ill-conditioned arrays causing large corrections to the state where either small or none are needed.

- Third-body perturbations cannot be ignored during the fitting process, especially when the timespans of data used contain multiple periods of the offending third-body frequencies. However, to properly account for these perturbations, even longer and possibly prohibitive time periods need to be used.

The limitations boil down to the reality that there is a battle between the competing desires to keep data intervals short and contain algorithm complexity yet have accurate orbital reconstruction. Unfortunately, the necessity to detect and properly recover low-frequency content generally increases the time period needed, if precision is desired, and it appears as a prohibiting factor at almost every turn in the analysis.

5.2 GPS Orbital Tori

Ultimately, the trajectory following methods used failed to achieve precision results required for operational GPS orbits. This was due primarily to the commensurability of the fastest two basis frequencies, but also due to the extremely long period of the smallest frequency, Ω_3. Most orbital tori fits were on the order of tens of kilometers or more for 10-week data batches, however least squares did find a minimizing solution such that fits were on the order of just a kilometer per coordinate axis. Unfortunately, this may be the limit of the error reduction. Thus, while orbital tori fits may suitable for long term tracking and accountability (i.e. disposal orbit operations), operational GPS satellites would not benefit from the fits obtained.

5.3 Orbital Spectral Decomposition by Frequency Cluster

From the lessons learned courtesy of the GPS orbit analysis, a new frequency cluster based method was proposed and developed. Rather than decompose one spectral line at a time, bands of lines (or frequency clusters) were decomposed from the orbital data by using the windowed form of the ATCFT. This allowed for the algorithm to compensate for local transform effects. A Hann window of order 2 was used to obtain torus fits with error as low as a few meters per coordinate axis in a year's worth of integrated LEO-type orbital position data. With clean, integrated data, the lower bound of error appears to be limited to the order of the expansion

of the basis set. The single-meter-per-axis error results were achieved with orbits containing 10 or more periods of the smallest non-negligible orbital frequency in the data sampled. With less than 10 periods, error in the fits grew quickly, especially using least squares methods. At 5 periods, error grew to tens and hundreds of meters per axis, depending on the orbital parameters of semi-major axis, inclination and eccentricity, and by 1 period, error was in the thousands of meters and as even as high as hundreds of thousand of meters. However, some of this error may be removed by a smart application of a simulated annealing algorithm to correct errors in the low-frequency coefficients. This is especially true if the cluster-based method initially used is based on least squares instead of a NAFF-based algorithm.

5.4 Final Conclusions and Recommendations

The goal of this research was to answer two primary research questions posed in the first chapter:

- Can GPS orbits be modeled as KAM tori? If so, will this effort lead to decreased GPS SIS URE? How much so?
- Can the KAM theorem be applied such that the burden on GPS operations is reduced?

The answer to the first part of the first question is potentially yes, but not with trajectory following methods in their current form. From the clean and delineated structure of the GPS's Fourier transform plot, it appears that there clearly is a KAM torus. However, the KAM theorem states that the basis set of a perturbed torus must be incommensurate for the torus to survive. While GPS orbits should still be a viable KAM tori candidate since they technically do not have any commensurabilities, the GPS basis set essentially does has a commensurate pair of frequencies from

a practical, trajectory-following-spectral-method perspective. Only by amassing hundreds of years of orbital data may the basis frequencies appear to be not completely commensurate to the methods used in this research. Should another method be devised, perhaps directly from the equations of motion themselves or by finding novel ways to characterize the torus indirectly through what can be gleamed from short timespans, it may be possible to model operational GPS orbits as KAM tori. The last two parts of this question cannot be definitively answered until the first part is, however preliminary analysis shows that it may be possible to lower the GPS SIS URE. While the effect may not be substantial when using the paradigm of current operational timescales due to the tremendous accuracy already achieved by present two-body methods, the invariant nature of orbital tori hint at a more dramatic effect over longer timescales. The exercise with the HST highlights this effect.

The second question posed can be answered with a qualified yes. If a method can be devised such that GPS orbital tori can be created, the invariant nature of tori allow one to conclude that should sufficient accuracy be obtained, the validity of the ephemerides provided by the orbital tori will have a much longer useful life. Since the ephemerides of current methods only have a useful life on the order of several hours, the orbital tori need only provide days of stability to decrease operational burdens. This by far is the largest, most significant impact to GPS operations or any constellation for that matter.

While this research has not satisfactorily satiated the proposed research questions, several contributions have been made in light of the discoveries made:

- KAM tori appear to be an excellent way to compress ephemerides.
- For non-operational missions, or those that are non-maneuvering, where years of data can be obtained, trajectory following methods may suffice.

- Until more sophisticated methods can be devised, the single largest class of earth-orbiting satellites that will benefit most from this research is orbital debris. With long data tracks, orbital tori estimates may be formed with considerable accuracy and allow for long-term tracking with potentially much less effort. Of course, those closest to the atmosphere will push the validity of the torus and research into how torus changes with air drag would need to be studied.

- Operational missions may have to hold out for equations-of-motion-based methods, or at least more sophisticated trajectory following methods that either more accurately back out an implied torus or stretch a nearby one such that it will suffice for operational requirements. Methods based on the equations of motion would employ a direct map from the equations of motion themselves to the torus, as opposed to the indirect method of surveying years of orbital data.

- Spectral decomposition by frequency cluster presents itself as the leading way to decompose and reconstruct an orbital torus. Unfortunately, the low-frequency detection issues limit the region of applicability of this method, assuming a relatively short finite amount of data. As the time span of the data increases, so does the applicability of the method.

- Coefficient correction by simulated annealing can fix low-frequency coefficient errors in certain special cases where a majority of the coefficients are properly decertified. Technique has potential to expand envelope of applicability of trajectory following methods.

While this work has made a few initial steps into the realm of trajectory following methods for artificial earth satellite orbits, many more can be accomplished. A few are:

- Incorporate third-body perturbations. Including frequencies attributable to third-body perturbations will increase the dimension of the torus by 2 dimensions for every additional frequency added. Thus, only those absolutely needed should be incorporated since the increased computational burden and complexity levied by their inclusion may become prohibitively costly in short order. Engineering trade-offs should be explored.

- Explore techniques to reveal long-period, toroidal motion while using orbital timespans that are a fraction of the long-period motion. While these techniques may be limited in use and scope, depending ont he orbital regime under consideration, and also increase the ad hoc nature and complexity of the overall method, they may be necessary until better methods can be obtained. The former issue is more important than the latter, however when introducing any new concept to an established, operational scenario, the less complex is usually better, especially when improvements may be marginal in the near term.

- Variations of the window used on the orbital data, to include higher orders of the Hanning window, should be examined to see if relief from decreasing values of Ω_3 can be obtained without having to resort to inordinate lengths of data.

Appendix A. Hamiltonian Dynamics

The following is a brief review of the Hamiltonian formulation of dynamics and assumes a basic understanding of Lagrangian mechanics. Further details can be found in selected reference texts in the bibliography from which this summary was extracted [29, 40, 44, 73]. For the sake of simplicity and to show the idealized power of Hamiltonian dynamics, it will be assumed for this section that the dynamical systems of interest are conservative with holonomic constraints only. While Hamiltonian dynamics can be applied to non-conservative systems with non-holonomic constraints after sufficient modifications, the solutions become arduous and unique to the problem. Hence, it is beyond the scope of this review.

Recall Lagrangian mechanics is premised on a recast of the definition of virtual work called D'Alembert's Principle:

$$\sum_i (\mathbf{F}_i - \dot{\mathbf{p}}_i) \cdot \delta \mathbf{r}_i = 0, \tag{118}$$

where $\mathbf{F}_i$ are the applied forces, $\dot{\mathbf{p}}_i$ are the time rate of change of momentum, and $\delta \mathbf{r}_i$ are the virtual displacements consistent with the coordinate r_i on every particle i. This expression states that the sum of the virtual work done by the virtual displacements consistent with the coordinates acting on the sum of the forces over all particles is zero. If the coordinates were independent, solving for the coefficients of each δr_i would yield the desired relationships to maintain this balance (i.e. the equations of motion of the system). However, since the coordinates are not necessarily independent in an arbitrary problem, transforming the native, physical coordinates into N generalized coordinates (i.e. one for each degree of freedom in the problem) is necessary. For a conservative system, doing so changes D'Alembert's Principle at Equation 118 to:

$$\sum_i \left\{ \frac{d}{dt}\left(\frac{\partial L}{\partial \dot{q}_i}\right) - \frac{\partial L}{\partial q_i} \right\} \delta q_i = 0, \tag{119}$$

where L is the Lagrangian (i.e. the difference of the kinetic and potential energies, $L = T - V$). Now, under the assumption of N independent q_i's, the coefficients of each δq_i is only possible if the following is true:

$$\frac{d}{dt}\left(\frac{\partial L}{\partial \dot{q}_i}\right) - \frac{\partial L}{\partial q_i} = 0, \tag{120}$$

where i is taken from $1, 2, \ldots N$. These N expressions are the N equations of motion, and the variables are the generalized coordinates q and their velocities $\dot{q}$.

Hamiltonian dynamics can be said to begin with a similar origin (i.e. the Principle of Virtual Work), however rather than using D'Alembert's Principle it uses Hamilton's Principle (which is just an integral form of D'Alembert's Principle). While the desired EOMs are obtained similarly to the Lagrangian EOMs, the fundamental idea behind Hamilton's principle is that the path of a system in phase space is such that the difference in the kinetic and potential energies are minimized. Hence, the problem reduces to finding an extremal such that Hamilton's Principle is met:

$$\delta I = \delta \int_{t_1}^{t_2} L dt = 0 \tag{121}$$

Per Legendre's dual transformation, the Lagrangian generalized coordinates of the q's and $\dot{q}$'s are discarded in favor of the q's and the generalized conjugate momenta, p's, where $p_i = \frac{\partial L}{\partial \dot{q}_i}$. Defining the Hamiltonian as:

$$\mathcal{H} = \sum_{i=1}^{N} p_i \dot{q}_i - L, \tag{122}$$

and taking the first variation yields:

$$\delta\mathcal{H} = \sum_{i=-1}^{N} \left(\dot{q}_i \delta p_i - \frac{\partial L}{\partial q_i} \delta q_i \right). \tag{123}$$

Since the first variation of the Hamiltonian as a function of the p's and q's is equivalent to that of Equation 122, then we can claim:

$$\sum_{i=-1}^{N} \left(\dot{q}_i \delta p_i - \frac{\partial L}{\partial q_i} \right) = \sum_{i=-1}^{N} \left(\frac{\partial \mathcal{H}}{\partial q_i} \partial q_i + \frac{\partial \mathcal{H}}{\partial p_i} \partial p_i \right). \tag{124}$$

Thus, it is clear the first half of the EOMs (i.e. the $\dot{q}$'s) are:

$$\dot{q}_i = \frac{\partial \mathcal{H}}{\partial p_i}. \tag{125}$$

By recalling (and rearranging) Lagrange's Equations at Equations 120, we see that:

$$\frac{d}{dt} \left(\frac{\partial L}{\partial \dot{q}_i} \right) = \frac{\partial L}{\partial q_i}. \tag{126}$$

Thus, introducing this result into Equation 124, we find the second half of the EOMs (i.e. the $\dot{p}$'s) are:

$$\dot{p}_i = -\frac{\partial \mathcal{H}}{\partial q_i}. \tag{127}$$

Equations 125 and 127 are known as Hamilton's Equations and are N first-order equations of motion that are linear in the coordinates and momenta.

Appendix B. Hamilton Jacobi Theory

This Appendix is a predominantly qualitative treatment of Hamilton-Jacobi theory. For a more detailed, mathematical description that includes illustrative examples, it is recommended that the reader peruse pertinent sections of Wiesel [97] or Goldstein [40]. Application of Hamilton-Jacobi theory to invariant tori can be found in Ott [82]. These sources were used in construction of this summary.

When studying a dynamical problem, it is often easier to solve the problem in one set of coordinates over another (i.e. polar vs. rectangular if circular motion is predominant in the problem). This holds true no matter the formulation of dynamics used. However, in the case of Hamiltonian mechanics, any transformation between coordinates must be canonical (i.e. a change of variables that preserves Hamilton's equations). A canonical transformation is the underlying fundamental of Hamilton-Jacobi theory. In fact, Hamilton-Jacobi theory seeks out one particular canonical transformation, should it exist, that literally solves the dynamical problem. Hamilton-Jacobi theory is also used in general perturbation theory to "solve" out the solvable part of a system's Hamiltonian. For example, in orbital mechanics applications, the two-body portion is separated from the alleged perturbation portion. This latter statement will make more sense shortly.

Recall, Hamilton's equations are of the the form:

$$\dot{q}_i = \frac{\partial \mathcal{H}(p,q)}{\partial p_i} \tag{128}$$

$$\dot{p}_i = -\frac{\partial \mathcal{H}(p,q)}{\partial q_i}, \tag{129}$$

where p and q are the momenta and coordinate variables, respectively. Thus, for a new set of variables P and Q, these equations would have the form:

$$\dot{Q}_i = \frac{\partial \mathcal{H}(\mathcal{P}, \mathcal{Q})}{\partial P_i} \tag{130}$$

$$\dot{P}_i = -\frac{\partial \mathcal{H}(\mathcal{P}, \mathcal{Q})}{\partial Q_i}. \tag{131}$$

For this transformation of variables to be canonical, Hamilton's principle for the old and new coordinates must hold. Recall Hamilton's Principle:

$$\delta I = \delta \int_{t_1}^{t_2} L dt = 0. \tag{132}$$

By remembering that $\mathcal{H}(p, q, t) = \sum_{i=1}^{N} p_i \dot{q}_i - L$, Hamilton's Principle in both sets of coordinates becomes:

$$\delta I = \delta \int_{t_1}^{t_2} \left(\sum_{i=1}^{N} p_i \dot{q}_i - \mathcal{H}(p, q, t) \right) dt = 0 \tag{133}$$

and

$$\delta I = \delta \int_{t_1}^{t_2} \left(\sum_{i=1}^{N} P_i \dot{Q}_i - \mathcal{K}(P, Q, t) \right) dt = 0, \tag{134}$$

where $\mathcal{H}$ and $\mathcal{K}$ are the old and new Hamiltonians, respectively. For this to be true, the integrands can differ only by as much as an arbitrary function, F, of some combination of the old and new variables. This function F is called the generating function and has four basic forms, denoted F_1, F_2, F_3 and F_4. The most commonly used form is F_2, and it is often denoted as S. By solving for S, the transformation laws between the old and new coordinates can be identified. Furthermore, the new Hamiltonian is found to be:

$$\mathcal{K}(P, Q) = \mathcal{H}(p, q) + \frac{\partial S}{\partial t}. \tag{135}$$

In Hamilton-Jacobi theory, the new variables are all constants and the problem is solved completely. Thus, $\mathcal{K}$ vanishes to zero. In perturbation theory, the solvable portion vanishes and the remaining term is attributed to the perturbations in the problem.

Appendix C. Notional UERE Analysis

This Appendix details the assumptions and simple calculations made to perform a notional UERE comparison between current, standard GPS operations and a possible new concept of GPS operations using KAM tori as the satellites' dynamics model. It must be stressed, this is done for illustrative purposes only and give a best case scenario for the application of KAM theory.

First, define the Space Segment errors with the following notation:

$$\delta_{Clk\ Stb} \quad : \quad Clock\ Stability \tag{136}$$

$$\delta_{Grp\ Del\ Stb} \quad : \quad Group\ Delay\ Stability \tag{137}$$

$$\delta_{Diff\ Grp\ Del\ Stb} \quad : \quad Differential\ Group\ Delay\ Stability \tag{138}$$

$$\delta_{Sat\ Acc\ Unc} \quad : \quad Satellite\ Acceleration\ Uncertainty \tag{139}$$

$$\delta_{Other\ Spc} \quad : \quad Other\ Space\ Segment\ Errors. \tag{140}$$

Similarly, define the Control Segment errors with the following notation:

$$\delta_{C/E\ Est} \quad : \quad Clock/Ephemeris\ Estimation \tag{141}$$

$$\delta_{C/E\ Pre} \quad : \quad Clock/Ephemeris\ Prediction \tag{142}$$

$$\delta_{C/E\ Fit} \quad : \quad Clock/Ephemeris\ Curve\ Fit \tag{143}$$

$$\delta_{Ion\ Del\ Fit} \quad : \quad Ionospheric\ Delay\ Model\ Terms \tag{144}$$

$$\delta_{Grp\ Del\ Corr} \quad : \quad Group\ Delay\ Time\ Correction \tag{145}$$

$$\delta_{Other\ Ctrl} \quad : \quad Other\ Control\ Segment\ Errors. \tag{146}$$

Thus, the squared sum of the space segment and control segment errors are calculated

by:

$$Space = \delta^2_{Clk\ Stb} + \delta^2_{Grp\ Del\ Stb} + \delta^2_{Diff\ Grp\ Del\ Stb} + \delta^2_{Sat\ Acc\ Unc} + \delta^2_{Other} \tag{147}$$

and

$$Control = \delta^2_{C/E\ Est} + \delta^2_{C/E\ Pre} + \delta^2_{C/E\ Fit} + \delta^2_{Ion\ Del\ Fit} + \delta^2_{Grp\ Del\ Corr} + \delta^2_{Other\ Ctrl}. \tag{148}$$

The root sum square of the space and control segment errors is the URE and is calculated by:

$$URE = \sqrt{Space + Control}. \tag{149}$$

Define the User Segment errors with the following notation:

$$\delta_{Ion\ Del\ Comp} \ : \ Ionospheric\ Delay\ Compensation \tag{150}$$

$$\delta_{Trop\ Del\ Comp} \ : \ Tropospheric\ Delay\ Compensation \tag{151}$$

$$\delta_{Rec\ Noise} \ : \ Receiver\ Noise\ and\ Resolution \tag{152}$$

$$\delta_{Mult} \ : \ Multipath \tag{153}$$

$$\delta_{Other\ User} \ : \ Other\ User\ Segment\ Errors. \tag{154}$$

The root sum square of the User Segment errors is the UEE and is calculated by:

$$UEE = \sqrt{\delta^2_{Ion\ Del\ Comp} + \delta^2_{Trop\ Del\ Comp} + \delta^2_{Rec\ Noise} + \delta^2_{Mult} + \delta^2_{Other\ User}}. \tag{155}$$

Finally, the root sum square of the URE and UEE is the UERE and is calculated by:

$$UERE = \sqrt{URE^2 + UEE^2}. \tag{156}$$

By assuming the values from Table 9 in Section 2.4 for standard GPS operations (Max AOD), the UEE, URE and UERE were found:

Table 15. URE, UEE and UERE for Standard GPS Operations

Error (meters)	Two Body GPS Model
URE	16.14
UEE	5.51
UERE	17.06

If we were to assume a KAM torus under the assumption given in Section 2.4, we would need to adjust the following parameters from the Space and Control Segment Errors in Table 9:

$$\delta_{Sat\ Acc\ Unc} \quad : \quad Satellite\ Acceleration\ Uncertainty \tag{157}$$

$$\delta_{C/E\ Est} \quad : \quad Clock/Ephemeris\ Estimation \tag{158}$$

$$\delta_{C/E\ Pre} \quad : \quad Clock/Ephemeris\ Prediction \tag{159}$$

$$\delta_{C/E\ Fit} \quad : \quad Clock/Ephemeris\ Curve\ Fit. \tag{160}$$

For a KAM torus, let us assume a best case scenario for the Satellite Acceleration Uncertainty term and set it to zero. Since the clock error, which is the dominant error when compared to ephemeris error, is included in the other three components which would change in a KAM torus scenario, the overall error components cannot just be set to zero. After consultation with navigation and timing experts within the 2SOPS [83], a rough estimate of each clock/ephemeris error component was established, which

were about 90 percent of each current estimate of the parameter. A summary of the changed values from Table 9 is:

$$\delta_{Sat\ Acc\ Unc} = 0\ meters \tag{161}$$

$$\delta_{C/E\ Est} = 1.8\ meters \tag{162}$$

$$\delta_{C/E\ Pre} = 6.03\ meters \tag{163}$$

$$\delta_{C/E\ Fit} = .72\ meters. \tag{164}$$

By inserting these new values into the previous calculations done for standard GPS operations, the UEE, URE and UERE for the KAM tori scenario were found to be:

Table 16. URE, UEE and UERE for Notional KAM Tori Model

Error (meters)	Notional KAM Tori GPS Model
URE	15.72
UEE	5.51
UERE	16.66

The preceding analysis shows that the KAM tori scenario has nearly 2.4 percent less error in the UERE. If this analysis is repeated using 14.5 days as the age of data (AOD), the pseudorange error is reduced by 18.2 percent.

Appendix D. Analytic Truncated Fourier Transform of Two Frequencies

Define the periodic function of m independent frequencies $f(t)$ as:

$$f(t) = \sum_{k_1,\, k_2,\, \ldots\, ,\, k_m} \tilde{C}_{k_1 \ldots k_m} \{ e^{i(k_1\omega_1 + k_2\omega_2 + \ldots + k_m\omega_m)t} \}, \tag{165}$$

where k represents each individual term of the Fourier Transform. Thus, the truncated Fourier transform of $f(t)$ over the interval $-T$ to T for 2 nearly commensurate, independent frequencies is:

$$TFT = \int_{-T}^{T} \left\{ \sum_{k_1,\, k_2} \tilde{C}_{k_1 k_2} \left\{ e^{i(k_1\omega_1 + k_2\omega_2)t} \right\} \right\} e^{-i\omega t} dt, \tag{166}$$

where ω is the range of frequencies over which the Fourier transform will be evaluated. Evaluating Equation 166 yields:

$$\begin{aligned}
TFT &= \sum_{k_1,\, k_2} \int_{-T}^{T} \left\{ \tilde{C}_{k_1 k_2} \left\{ e^{i(k_1\omega_1 + k_2\omega_2)t} \right\} \right\} e^{-i\omega t} dt && (167)\\
&= \sum_{k_1,\, k_2} \int_{-T}^{T} \tilde{C}_{k_1 k_2} \left\{ e^{i((k_1\omega_1 + k_2\omega_2) - \omega)t} \right\} dt && (168)\\
&= \sum_{k_1,\, k_2} \left\{ \frac{\tilde{C}_{k_1 k_2}}{i((k_1\omega_1 + k_2\omega_2) - \omega)} e^{i((k_1\omega_1 + k_2\omega_2) - \omega)t} \right\} \Big|_{-T}^{T} && (169)\\
&= \sum_{k_1,\, k_2} \frac{2\tilde{C}_{k_1 k_2}}{((k_1\omega_1 + k_2\omega_2) - \omega)} \sin\left(((k_1\omega_1 + k_2\omega_2) - \omega)T \right) && (170)
\end{aligned}$$

Or, without using complex coefficients Equation 165 becomes:

$$f(t) = a_o + \sum_{k_1,\, k_2,\, \ldots\, ,\, k_m} \left\{ a_k \cos(\Psi t) + b_k \sin(\Psi t) \right\}, \tag{171}$$

where once again k represents each individual term of the Fourier Transform and $\Psi = (k_1\omega_1 + k_2\omega_2 + \ldots + k_m\omega_m)$. Thus, the truncated Fourier transform of $f(t)$ over the interval $-T$ to T for 2 nearly commensurate, independent frequencies is:

$$TFT = \int_{-T}^{T} \left\{ a_o + \sum_{k_1,\, k_2} \{a_k \cos(\Psi t) + b_k \sin(\Psi t)\} \right\} e^{-i\omega t} dt, \tag{172}$$

where once again ω is the range of frequencies over which the Fourier transform will be evaluated. Evaluating Equation 172 yields:

$$\begin{aligned}
TFT &= \int_{-T}^{T} a_o e^{-i\omega t} dt + \sum_{k_1,\, k_2} \left\{ \int_{-T}^{T} \{a_k \cos(\Psi t) + b_k \sin(\Psi t)\} e^{-i\omega t} dt \right\} && (173)\\
&= a_o \left\{ \frac{e^{i\omega T} - e^{-i\omega T}}{i\omega} \right\} + \sum_{k_1,\, k_2} \left\{ \int_{-T}^{T} \{a_k \cos(\Psi t) + b_k \sin(\Psi t)\} e^{-i\omega t} dt \right\} && (174)\\
&= \frac{2a_o}{\omega} \sin(\omega T) + \sum_{k_1,\, k_2} \left\{ \int_{-T}^{T} \{a_k \cos(\Psi t) + b_k \sin(\Psi t)\} e^{-i\omega t} dt \right\} && (175)\\
&= 2Ta_o \mathrm{sinc}(\omega T) + \sum_{k_1,\, k_2} \left\{ \int_{-T}^{T} \{a_k \cos(\Psi t) + b_k \sin(\Psi t)\} e^{-i\omega t} dt \right\} && (176)\\
&= 2Ta_o \mathrm{sinc}(\omega T) + \sum_{k_1,\, k_2} \int_{-T}^{T} \Big\{ a_k \cos(\Psi t)\cos(\omega t) - ia_k \cos(\Psi t)\sin(\omega t) \\
&\quad + b_k \sin(\Psi t)\cos(\omega t) - ib_k \sin(\Psi t)\sin(\omega t) \Big\} dt && (177)\\
&= 2Ta_o \mathrm{sinc}(\omega T) + \sum_{k_1,\, k_2} \int_{-T}^{T} \Big\{ \frac{a_k \cos(\Psi t - \omega t)}{2} + \frac{a_k \cos(\Psi t + \omega t)}{2} \\
&\quad - \frac{ia_k \sin(\Psi t + \omega t)}{2} + \frac{ia_k \sin(\Psi t - \omega t)}{2} + \frac{b_k \sin(\Psi t + \omega t)}{2} + \frac{b_k \sin(\Psi t - \omega t)}{2} \\
&\quad - \frac{ib_k \cos(\Psi t - \omega t)}{2} + \frac{ib_k \cos(\Psi t + \omega t)}{2} \Big\} dt && (178)\\
&= 2Ta_o \mathrm{sinc}(\omega T) + \sum_{k_1,\, k_2} \Big\{ \frac{a_k}{(\Psi - \omega)} \sin((\Psi - \omega)T) + \frac{a_k}{(\Psi + \omega)} \sin((\Psi + \omega)T) \\
&\quad - \frac{ib_k}{(\Psi - \omega)} \sin((\Psi - \omega)T) + \frac{ib_k}{(\Psi + \omega)} \sin((\Psi + \omega)T) \Big\} && (179)
\end{aligned}$$

$$
\begin{aligned}
= \quad & 2Ta_o\text{sinc}(\omega T) + \sum_{k_1,\, k_2} \Big\{ Ta_k \big\{ \text{sinc}((\Psi - \omega)T) + \text{sinc}((\Psi + \omega)T) \big\} \\
& + iTb_k \big\{ \text{sinc}((\Psi + \omega)T) - \text{sinc}((\Psi - \omega)T) \big\} \Big\} \qquad (180)
\end{aligned}
$$

Normalizing by $2T$ results in the final, expected analytical result of:

$$
\begin{aligned}
TFT \quad = \quad & a_o\text{sinc}(\omega T) \\
& + \sum_{k_1,\, k_2} \Big\{ \frac{a_k}{2} \big\{ \text{sinc}((\Psi - \omega)T) + \text{sinc}((\Psi + \omega)T) \big\} \\
& + \frac{ib_k}{2} \big\{ \text{sinc}((\Psi + \omega)T) - \text{sinc}((\Psi - \omega)T) \big\} \Big\} \qquad (181)
\end{aligned}
$$

Appendix E. IGS Data Format Detail

GPS final orbit files are in SP3 format. The first 22 lines contain comments in the form of a header and they are described by Hilla as the following [49]:

On line one, character two is the format version identification character. This third SP3 version has been designated version 'c'. Subsequent versions will use lower case letters in alphabetical order. The first line comprises the Gregorian date and time of day of the first epoch of the orbit, the number of epochs in the ephemeris file (up to 10 million), the data used descriptor, the coordinate system used descriptor, the orbit type descriptor, and the agency descriptor. The data used descriptor was included for ease in distinguishing between multiple orbital solutions from a single organization. This will have primary use for the agency generating the orbit. Orbit type is described by a three character descriptor. At this time only four have been defined: FIT (fitted), EXT (extrapolated or predicted), BCT (broadcast), and HLM (fitted after applying a Helmert transformation). Naturally, others are possible. The computing agency descriptor allows four characters (e.g. NGS, IGS, etc.).

The second line has: the GPS week; the seconds of the GPS Week elapsed at the start of the orbit ($0.0 \leq$ seconds of week < 604800.0); the epoch interval ($0.0 <$ epoch interval < 100000.0) in seconds; the modified Julian Day Start (where 44244 represents GPS zero time – January 6, 1980); and fractional part of the day ($0.0 \leq$ fractional < 1.0) at the start of the orbit.

The third line to the seventh lines indicate the number of satellites followed by their respective identifiers. The identifiers must use consecutive slots and continue on lines 4-7, if required. The value 0 should only appear after all the identifiers are listed. Satellite identifiers may be listed in any order. However, for ease in reviewing satellites included in the orbit file it is recommended that alphabetical/numerical order be used. Each identifier will consist of a letter followed by a 2-digit integer

between 01 and 99. For example, “Gnn” for GPS satellites, “Rnn” for GLONASS satellites, “Lnn” for Low-Earth Orbiting (LEO) satellites, and “Enn” for Galileo satellites. Other letters will be allowed for other types of satellites. Lower numbered satellites must always have a preceding zero (e.g., “G09” not “G 9”). The letter, which represents the Satellite System Indicator, must always be present (i.e.,“ 09” is no longer a valid satellite identifier). This is a significant change from SP3-a and needs to be noted when software is updated to read the new SP3-c format. A list of identifiers created for LEO satellites can be viewed at http://cddis.gsfc.nasa.gov/sp3c satlist.html.

The eighth line to the twelfth lines have the orbit accuracy exponents. The value 0 is interpreted as accuracy unknown. A satellite’s accuracy exponent appears in the same slot on lines 8-12 as the identifier on lines 3-7. The accuracy is computed from the exponent as in the following example. If the accuracy exponent is 13, the accuracy is 2**13 mm or $\approx$ 8 m. The quoted orbital error should represent one standard deviation and be based on the orbital error in the entire file for the respective satellite. This may lead to some distortion when orbit files are joined together, or when a file contains both observed and predicted data.

On the thirteenth line, columns 4-5 hold the File Type descriptor. This is a single character left-justified in the two-character field. The currently defined values are: “G ” for GPS only files, “M ” for mixed files, “R ” for GLONASS only files, “L ” for LEO only files, and “E ” for Galileo only files. No default values are implied; either “G ”, “M ”, “R ”, “L ”, or “E ” is required. On this same line, columns 10-12 hold the Time System Indicator. In order to remove any ambiguity with respect to which time system is being used in mixed files, this field specifies the time system used in each SP3-c file: use “GPS” to identify GPS Time, “GLO” to identify the GLONASS UTC time system, “GAL” to identify Galileo system time, “TAI” to identify International

Atomic Time, or "UTC" to identify Coordinated Universal Time. No default value is implied; either "GPS", "GLO", "GAL", "TAI, or "UTC" must be specified.

On Line fifteen, columns 4-13 hold the floating-point base number used for computing the standard deviations for the components of the satellite position and velocity. Instead of using 2**nn as is done in lines 8-12 in the header, better resolution can be attained using a number like 1.25**nn. The units for position and velocity are mm and 10**-4 mm/sec, respectively. Likewise, columns 15-26 hold the floating-point base number for computing the standard deviations for the clock correction and the rate-of-change of the clock correction. Again, instead of using 2**nnn, one might use a number like 1.025**nnn. The units for the clock correction and the rate-of- change of the clock correction are picosec and 10**-4 picosec/sec, respectively.

Lines 13-18 have been designed so that additional parameters may be added to the SP3 format.

Lines 19-22 are free form comments (comments go in columns 4-60).

The remainder of the file is data and an example can be seen at Table 17. In the final orbit file the epoch identification lines have an asterisk in the first column. The remaining entries on this line are as follows: year, month, day of month, hour, minutes, seconds. The position and clock record for satellites are on lines beginning with P or PG. Columns three and four are the PRN identifying a given satellite. The remaining entries are in order: the x, y, and z coordinates in km, the clock given in microseconds, the standard deviations for each of the components x, y, z, and the clock. [31]

Table 17. Example of SP3 Data Format

* 2004	5	30	0	0	0.00000000
P	1	-23195.181622	-3013.628703	12772.712307	346.168808
P	3	-6071.476357	-14766.018074	-21325.242610	14.705685
P	4	-3171.971954	16942.297435	20131.630410	-160.386383
P	5	14182.976510	8030.597298	20868.712809	32.469264
P	6	25918.339563	-5232.697204	3405.070186	33.645445
P	7	-13590.421527	16754.326696	15797.234119	524.021782
P	8	-10193.750420	11333.779436	-21929.823800	-1.049732
P	9	21503.988245	15055.819657	4765.927650	-46.808114
P	10	2821.356383	22886.629373	-12986.985002	44.792169
P	11	-22897.779060	-12242.983231	5922.665335	121.012073
P	13	-25460.529360	7376.883081	-744.249839	-28.061732
P	14	15570.463029	-15101.394304	15375.474624	-20.715252
P	15	3569.405863	-17055.151526	-20193.186058	272.963268
P	16	-442.472257	-24795.755048	-9403.083465	11.328902
P	17	16335.412334	21449.056170	1099.506271	-18.064237
P	18	16159.292069	-12002.600170	-17181.172605	-39.499871
P	19	-17263.100304	-8999.348055	-17937.689026	-43.748995
P	20	-14597.895850	-3931.006035	21759.805549	-158.278298
P	21	16852.487012	-3166.666688	-20426.058120	75.974078
P	22	12750.270335	-21872.023246	-7932.434857	7.275665
P	24	8589.267241	21919.705779	12515.190864	30.655308
P	25	-1471.399252	-18959.301421	18916.065343	67.721208
P	26	14559.944198	10106.683930	-20249.569319	95.611734
P	27	-18197.929778	2065.712516	-18910.799911	221.286010
P	28	-11773.323318	22138.474599	-8066.944051	33.155490
P	29	9180.944520	12279.646310	-21442.038826	229.997463
P	30	16164.440850	-7022.161413	19610.354912	541.458122
P	31	-24344.771513	-680.289015	-11403.023026	186.126078

Appendix F. Windowed ATCFT Expressions

Using Mathematica, the expressions for the values within the matrix of coefficients corresponding to the cosine and sine terms within the ATCFT while using Hann (a.k.a. Hanning) windows of order one and three were calculated. Their equivalent forms after applying L'Hopital's rule for when $(\omega^2 - \Psi^2)$ is close to zero was also found. The results can be found below.

For the Hann window of order one:

$$\begin{aligned} C &= (e^{-iT\omega}\pi^2(-(-1+e^{2iT\omega})(i\pi^2\omega - iT^2\omega(3\Psi^2+\omega^2))\cos[T\Psi] \\ &\quad -(1+e^{2iT\omega})\Psi(\pi^2 - T^2(\Psi^2+3\omega^2))\sin[T\Psi]))/ \\ &\quad (2T(-\Psi^2+\omega^2)(\pi^4 + T^4(\Psi^2-\omega^2)^2 - 2\pi^2T^2(\Psi^2+\omega^2))) \end{aligned} \tag{182}$$

and

$$\begin{aligned} S &= (e^{-iT\omega}\pi^2(-(-1+e^{2iT\omega})(\pi^2\Psi - T^2(\Psi^3+3\Psi\omega^2))\cos[T\Psi] \\ &\quad +i(1+e^{2iT\omega})\omega(\pi^2 - T^2(3\Psi^2+\omega^2))\sin[T\Psi]))/ \\ &\quad (2T(-\Psi^2+\omega^2)(\pi^4 + T^4(\Psi^2-\omega^2)^2 - 2\pi^2T^2(\Psi^2+\omega^2))). \end{aligned} \tag{183}$$

After applying L'Hopital's rule, these expressions become:

$$C = \frac{2\pi^2\Psi - 8\Psi^3 + \pi^2\sin[2\Psi]}{4\Psi(\pi^2 - 4\Psi^2)} \tag{184}$$

and

$$S = -\frac{i(\pi^4\Psi - 4\pi^2\Psi^3 - \pi^4\cos[\Psi]\sin[\Psi])}{2\pi^2\Psi(\pi^2 - 4\Psi^2)}. \tag{185}$$

For the Hann window of order three:

$$\begin{aligned}
C = {} & (36\pi^6(-\Psi(-36\pi^6 + 49\pi^4T^2(\Psi^2 + 3\omega^2) - 14\pi^2T^4(\Psi^4 + 10\Psi^2\omega^2 + 5\omega^4) \\
& +T^6(\Psi^6 + 21\Psi^4\omega^2 + 35\Psi^2\omega^4 + 7\omega^6))\cos(T\omega)\sin(T\Psi) + \omega(-36\pi^6 + 49\pi^4T^2(3\Psi^2 + \omega^2) \\
& -14\pi^2T^4(5\Psi^4 + 10\Psi^2\omega^2 + \omega^4) + T^6(7\Psi^6 + 35\Psi^4\omega^2 + 21\Psi^2\omega^4 \\
& +\omega^6))\cos(T\Psi)\sin(T\omega)))/ \\
& (T(9\pi^4 - 10\pi^2T^2(\Psi - \omega)^2 + T^4(\Psi - \omega)^4)(\Psi^2 - \omega^2)(9\pi^4 - 10\pi^2T^2(\Psi + \omega)^2 \\
& +T^4(\Psi + \omega)^4)(16\pi^4 + T^4(\Psi^2 - \omega^2)^2 - 8\pi^2T^2(\Psi^2 + \omega^2)))
\end{aligned} \tag{186}$$

and

$$\begin{aligned}
S = {} & (36i\pi^6(\omega(-36\pi^6 + 49\pi^4T^2(3\Psi^2 + \omega^2) - 14\pi^2T^4(5\Psi^4 + 10\Psi^2\omega^2 + \omega^4) \\
& +T^6(7\Psi^6 + 35\Psi^4\omega^2 + 21\Psi^2\omega^4 + \omega^6))\cos(T\omega)\sin(T\Psi) - \Psi(-36\pi^6 + 49\pi^4T^2(\Psi^2 + 3\omega^2) \\
& -14\pi^2T^4(\Psi^4 + 10\Psi^2\omega^2 + 5\omega^4) + T^6(\Psi^6 + 21\Psi^4\omega^2 + 35\Psi^2\omega^4 \\
& +7\omega^6))\cos(T\Psi)\sin(T\omega)))/ \\
& (T(9\pi^4 - 10\pi^2T^2(\Psi - \omega)^2 + T^4(\Psi - \omega)^4)(\Psi^2 - \omega^2)(9\pi^4 - 10\pi^2T^2(\Psi + \omega)^2 \\
& +T^4(\Psi + \omega)^4)(16\pi^4 + T^4(\Psi^2 - \omega^2)^2 - 8\pi^2T^2(\Psi^2 + \omega^2))).
\end{aligned} \tag{187}$$

After applying L'Hopital's rule, these expressions become:

$$C = \frac{(9\pi^6\Psi - 49\pi^4\Psi^3 + 56\pi^2\Psi^5 - 16\Psi^7 + 9\pi^6\cos[\Psi]\sin[\Psi])}{2\Psi(9\pi^6 - 49\pi^4\Psi^2 + 56\pi^2\Psi^4 - 16\Psi^6)} \tag{188}$$

and

$$S = -\frac{i(9\pi^6\Psi - 49\pi^4\Psi^3 + 56\pi^2\Psi^5 - 16\Psi^7 - 9\pi^6\cos[\Psi]\sin[\Psi])}{2\Psi(9\pi^6 - 49\pi^4\Psi^2 + 56\pi^2\Psi^4 - 16\Psi^6)}. \tag{189}$$

Appendix G. Basis Set Survey

A survey of how Ω_1 and Ω_2 change with semi-major axis, eccentricity, and inclination was accomplished to demonstrate the the interplay between each variable. The results are summarized graphically in the following plots.

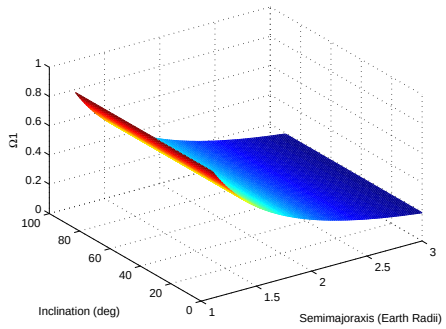

43.1: Sweep on Inclination/Semi-major Axis

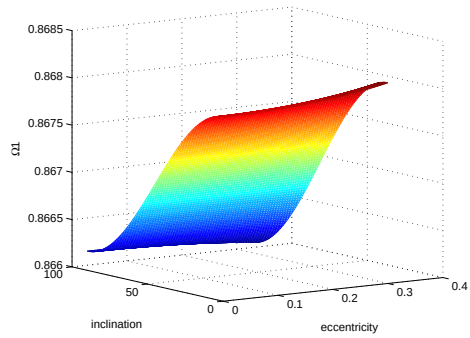

43.2: Sweep on Inclination/Eccentricity

Figure 43. Orbital Survey of Acceptable Ω_1 Magnitudes

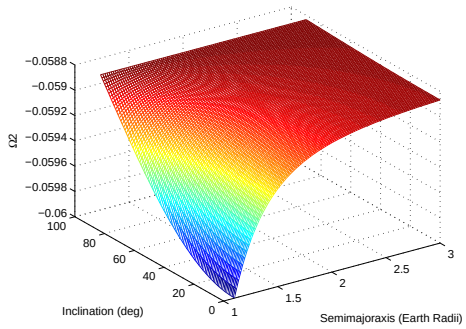

44.1: Sweep on Inclination/Semi-major Axis

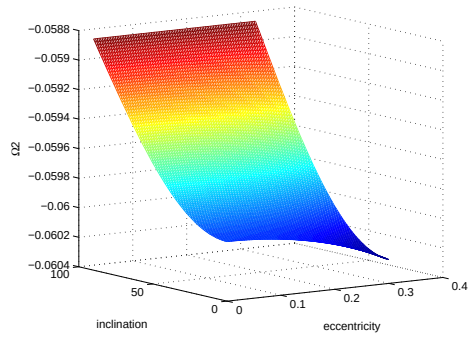

44.2: Sweep on Inclination/Eccentricity

Figure 44. Orbital Survey of Acceptable Ω_2 Magnitudes

Appendix H. Error From a Non-Cluster-Based Approach

The figures below depict the consequences of removing single lines within a frequency cluster instead of fitting/removing the entire frequency cluster structure to account for local transform effects. Each figure in this appendix has a corresponding twin in Chapter IV that shows the error in the tori fits if the frequency cluster is fit as a whole structure. In general, comparing the plots shows that at low altitudes the additional error is not overly significant, but as semi-major axis grows, so does the error.

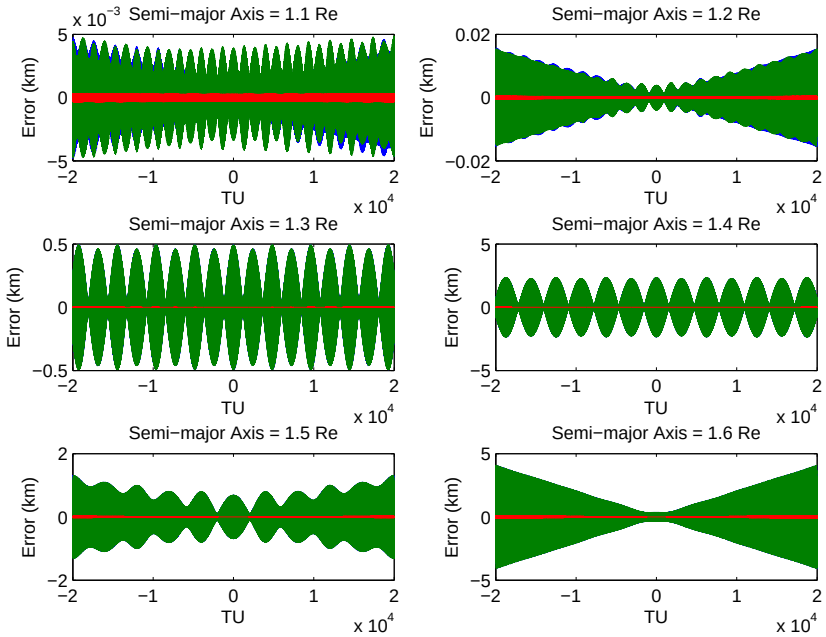

Figure 45. Torus Fit Error w/o ATCFT (i=0 deg, e=0.01, a=1.1 to 1.6 Re)

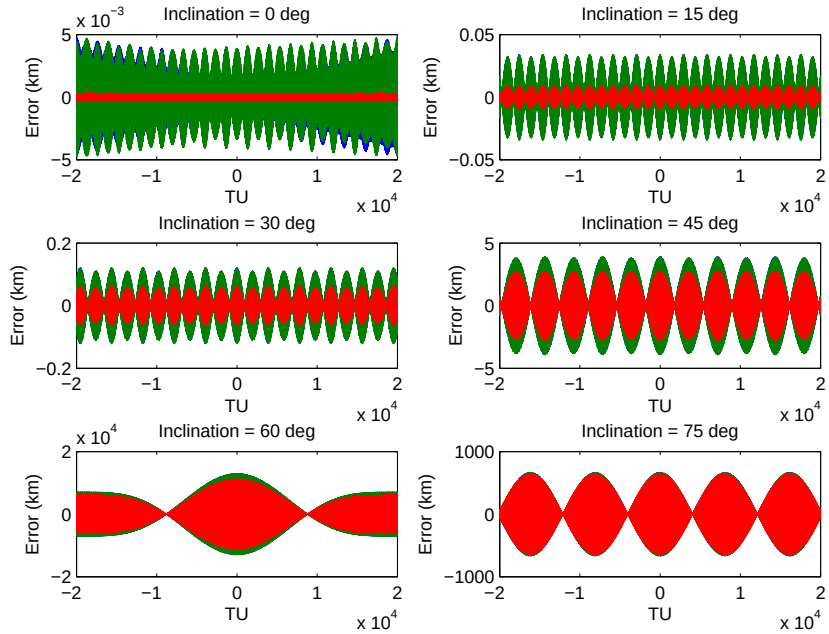

Figure 46. Torus Fit Error w/o ATCFT (a=1.1 Re, e=0.01, i=0 to 75 deg)

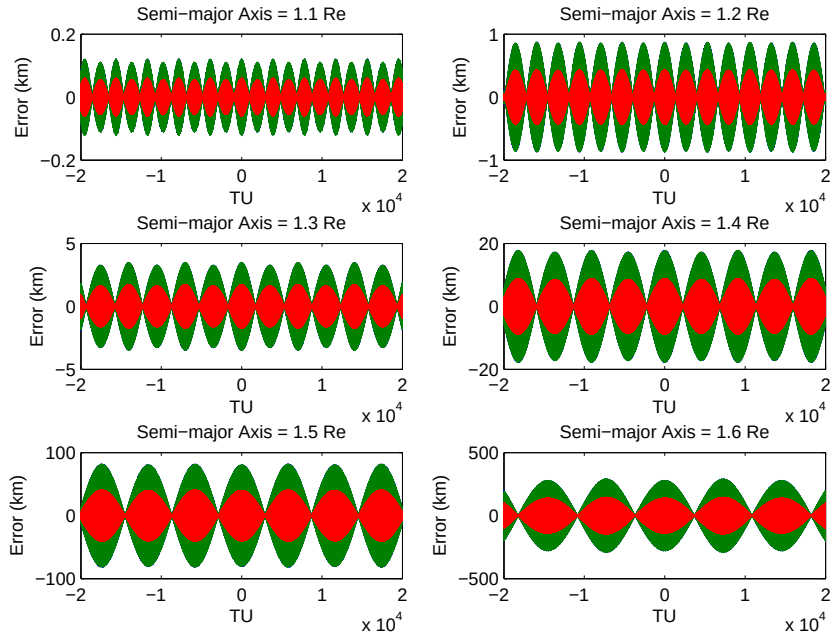

Figure 47. Torus Fit Error w/o ATCFT (i=30 deg, e=0.01, a=1.1 to 1.6 Re)

Bibliography

[1] Aeronautics, National and Space Administration. "LAGEOS". URL http://nssdc.gsfc.nasa.gov/nmc/spacecraftOrbit.do?id=1976-039A.

[2] Ananda, Mohan. *The Global Positioning System (GPS) Constellation and Coverage*. NASA Technical Report 198900015p5n, The Aerospace Corporation, Sep 1988.

[3] Arnold, V. I. "Proof of a Theorem of A. N. Kolmogorov on the Invariance of Quasi-Periodic Motions Under Small Perturbations of the Hamiltonian". *Russian Mathematical Surveys*, 18(5):9–36, 1963.

[4] Arnold, V.I. *Mathematical Methods of Classical Mechanics*. Springer, second edition edition, 1989.

[5] Asimov, Isaac. "Quotes: Pithy Sayings for the New World of Work". URL http://www.thephoenixprinciple.com/quotes/2004/11/isaac_asimov_th.html.

[6] Bar-Sever, Y. and D. Kuang. "New Empirically Derived Solar Radiation Pressure Model for Global Positioning System Satellites". *InterPlanetary Network Progress Report*, 42-159:1–11, 2004.

[7] Benjamin, Lt Col Frank K. *The Continued Evolution of the Air Mobility Command*. USAWC Research Project, United States Army War College (USAWC), Carlisle Barracks,Carlisle,PA,17013-5050, March 2006.

[8] Binney, J. and S. Kumar. "Angle Variables for Numerically Fitted Orbital Tori". *Monthly Notices of the Royal Astronomical Society*, 261:584–592, 1993.

[9] Binney, J. and D. Spergel. "Spectral Stellar Dynamics". *Monthly Notices of the Royal Astronomical Society*, 252:308–321, January 1982.

[10] Binney, James and David Spergel. "Spectral Stellar Dynamics II - The Action Integrals". *Monthly Notices of the Royal Astronomical Society*, 206:159–177, 1984.

[11] Book, Stephen A., Wayne F. Brady, and Paul K. Mazaika. "The Nonuniform GPS Constellation". *IEEE Position Location and Navigation Symposium*. Atlantic City, New Jersey, 8-11 Dec 1980.

[12] Bordner, Captain Ralph E. *Estimation of Relative Satellite Formation Element Positions in near Circular Orbits*. Master's thesis, Air Force Institute of Technology (AFIT), March 2001.

[13] Brady, Wayne F. and Paul S. Jorgensen. "Worldwide Coverage of the Phase II NAVSTAR Satellite Constellation". *Navigation: Journal of the Institude of Navigation*, 28(3):167–177, Fall 1981.

[14] Bruin, Peter. "Perturbations of Conditionally Periodic Motion", 16 November 2004. Lecture Notes.

[15] Castillo, LCDR A. Dean. *The Berlin Airlift: A Naval Aviators Perspective On The Greatest Combined Joint Humanitarian Airlift In The History Of Airpower*. ACSC Research Project, Air Command and Staff College (ACSC), Maxwell Air Force Base, Alabama, April 2006. AU/ACSC/8378/AY06.

[16] Celletti, Alessandra. "Construction of Librational Invariant Tori in the Spin-Orbit Problem". *Zeitschrift für Angewandte Mathematik und Physik*, 45:61–80, 1994.

[17] Celletti, Alessandra, Andrea Chessa, John Hadjidemetriou, and Giovanni Battista Valsecchi. "A Systemeatic Study of the Stability of Symmetric Periodic Orbits in the Planar, Circular, Restricted Three-Body Problem". *Celestial Mechanics and Dynamical Astronomy*, 83:239–255, 2002.

[18] Celletti, Alessandra and Luigi Chierchia. "On Rigorous Stability Results for Low-Dimensional KAM Surfaces". *Physics Letters A*, 128(3/4):166–168, 1988.

[19] Celletti, Alessandra and Luigi Chierchia. "KAM Stability Estimates in Celestial Mechanics". *Planet. Space Sci.*, 46(11/12):1433–1440, 1998.

[20] Celletti, Alessandra and Luigi Chierchia. "KAM Stability for a Three-Body Problem of the Solar System". *Zeitschrift für Angewandte Mathematik und Physik*, 57:33–41, 2006.

[21] Celletti, Alessandra and Luigi Chierchia. "KAM Tori for N-body Problems: A Brief History". *Celestial Mechanics and Dynamical Astronomy*, 95:117–139, 2006.

[22] Celletti, Alessandra and Corrado Falcolini. "Singularities of Periodic Orbits Near Invariant Curves". *Physica D*, 170:87–102, 2002.

[23] Chao, C. C. "MEO Disposal Orbit Stability and Direct Reentry Strategy, AAS 00-152". *AAS/AIAA Space Flight Mechanics Meeting*. Clearwater, Florida, 23-26 January 2000.

[24] Chao, C. C. and R. A. Gick. "Long-Term Evolution Of Navigation Satellite Orbits: GPS/GLONASS/GALILEO". *Advances in Space Research*, 34:1221–1226, 2004.

[25] Chapra, Steven C. and Raymond P. Canale. *Numerical Methods for Engineers*. McGraw-Hill Book Company, second edition, 1988.

[26] Craft, First Lieutenant Christopher. *Formation Flight of Earth Satellites on KAM Tori*. Master's thesis, Air Force Institute of Technology, 2009.

[27] Crider, Captain Jeffrey S. "GPS Contact Statistics", Aug 2007.

[28] Crider, Captain Jeffrey S. "Email and telephonic correspondence", Aug 2008.

[29] Danby, J.M.A. *Fundamentals of Celestial Mechanics*. Willman-Bell, Inc., second edition edition, 1992.

[30] Delshams, Amadeu and Pere Gutiérrez. "Effective Stability and KAM Theory". *Journal of Differential Equations*, 128(2):415–490, 1996.

[31] Derbis, Captain Rachel M. *Modeling GPS Satellite Orbits as KAM Tori*. Master's thesis, Air Force Institute of Technology, 2008.

[32] Dethomas, Scott V. *Aerial Humanitarian Operations: Delivering Strategic Effects*. SAASS Thesis, School Of Advanced Air And Space Studies (SAASS), Maxwell Air Force Base, Alabama, June 2004.

[33] Division, GEOINT SCIENCES OFFICE: Global Positioning System (GPS). "GPS Ephemeris Data". URL `http://earth-info.nga.mil/GandG/sathtml/`.

[34] Dow, J. M., R. E. Neilan, and G. Gendt. "The International GPS Service (IGS): Celebrating the 10th Anniversary and Looking to the Next Decade". *Adv. Space Res.*, volume 36, 320–326. 2005.

[35] Ely, Todd A. "Impact of Eccentricity on East-West Stationkeeping for the GPS Class of Orbits". *AAS/AIAA Astrodynamics Conference*. Girdwood, Alaska, 16-18 Aug 1999.

[36] Ely, Todd A. and Kathleen C. Howell. "East-West Stationkeeping Of Satellite Orbits With Resonant Tesseral Harmonics". *Acta Astronautica*, 46(1):1–15, 2000.

[37] Fullenwider, Elmer D. and Paul S. Jorgensen. "The Updated NAVSTAR/GPS Test and Operational Constellations". *IEEE Position Location and Navigation Symposium*. San Diego, California, 26-29 Nov 1984.

[38] Gelb, Arthur. *Applied Optimal Estimation*. MIT Press, 1974.

[39] Gick, R. A. and C. C. Chao. "GPS Disposal Orbit Stability And Sensitivity Study, AAS/AIAA 01-244". *AAS/AIAA Flight Mechanics Meeting*. Santa Barbara, California, 11-14 February 2001.

[40] Goldstein, Herbert. *Classical Mechanics*. Addison-wesley Publishing Company, Inc., 1950.

[41] Gomez, G., J.M. Mondelo, and C. Simoó. "Refined Fourier Analysis: Procedures, Error Estimates and Applications", Preprint 2002.

[42] Granville, V, M Krivanek, and JP Rasson. "Simulated Annealing: A Proof of Convergence". *IEEE Transactions on Pattern Analysis and Machine Intelligence*, 16(6):652–656, June 1994.

[43] Green, Colonel G. B., P. D. Massatt, and N. W. Rhodus. "The GPS 21 Primary Satellite Constellation". *Navigation: Journal of The Institute of Navigation*, 36(01):9–24, Spring 1989.

[44] Greenwood, Donald T. *Classical Dynamics*. Prentice-Hall, Inc., 1977.

[45] Guzzo, Massimilliano. "Long-Term Stability Analysis Of Quasi Integrable Degenerate Systems Through The Spectral Formulation Of The Nekhoroshev Theorem". *Celestial Mechanics and Dynamical Astronomy*, 83:303–323, 2002.

[46] Guzzo, Massimilliano and Giancarlo Benettin. "A Spectral Formulation Of The Nekhoroshev Theorem And Its Relevance For Numerical And Experimental Data Analysis". *Discrete and Continuous Dynamical Systems - Series B*, 1(1):1–28, 2001.

[47] Harris, Frederic J. "On the Use of Windows for Harmonic Analysis with the Discrete Fourier Transform". *Proceedings of the IEEE*, 66(1):51–83, January 1978.

[48] Herman, R. L. *An Introduction to Fourier and Complex Analysis with Applications to the Spectral Analysis of Signals*. Monograph, 2008. Online Book: http://people.uncw.edu/hermanr/mat367/FCABook/index.htm.

[49] Hilla, Steve. "The Extended Standard Product 3 Orbit Format (SP3-c)". National Geodetic Survey, 12 Feb 2007.

[50] HQUSAF/XPXT. *The USAF Transformation Flight Plan, FY03-07*. Transformation Division, Pentagon, Washington D.C., 2003.

[51] Hugentobler, U., D. Ineichen, and G. Beutler. "GPS Satellites: Radiation Pressure, Attitude and Resonance". *Advances in Space Research*, 31(8):1917–1926, 2003.

[52] Hughes. "CS004 Introduction to Scientific Computing: FFT Info". Class Notes, Spring 2007.

[53] Hunter, C. "Spectral Analysis of Orbits via Discrete Fourier Transforms". *Space Science Reviews*, volume 102, 83–99. October 2002.

[54] Ineichen, D., G. Beutler, and U. Hugentobler. "Sensitivity of GPS and GLONASS Orbits with Respect to Resonant Geopotential Parameters". *Journal of Geodesy*, 77:478–486, 2003.

[55] Iorio, Lorenzo (editor). *The Measurement of Gravitomagnetism: A Challenging Enterprise*. Nova Science Publishers, Inc., 2007.

[56] Kaasalainen, Mikko. "Construction of invariant tori in chaotic regions". *Physical Review E*, 52(1):1193–1196, 1995.

[57] Kaasalainen, Mikko and James Binney. "Construction of Invariant Tori and Integrable Hamiltonians". *Physical Reveiw Letters*, 73:2377–2381, 1994.

[58] Kaasalainen, Mikko and James Binney. "Torus construction in potentials supporting different orbit families". *Monthly Notices of the Royal Astronomical Society*, 268:1033–1040, 1994.

[59] Kaplan, Elliiot D. *Understanding GPS: Principles and Applications*. Artech House, Inc, 1996.

[60] Kaula, William M. *Theory of Geodesy: Applications of Satellites to Geodesy*. Dover, 2000.

[61] Kirkpatrick, S., Jr. C. D. Gelatt, and M. P. Vecchi. "Optimization by Simulated Annealing: Quantitative Studies". *Journal of Statistical Physics*, Volume 34(5-6):975–986, March 1983.

[62] Kolmogorov, A. N. "The Conservation of Conditionally Periodic Motions with a Small Variation in the Hamiltonian". *Doklady Akademii nauk SSSR*, 98:527–530, 1954.

[63] Kruh, Pierre. "The Navstar Global Positioning System Six-Plane 18-Satellite Constellation". *National Telecommunications Conference*. New Orleans, Lousianna, 1981.

[64] Kuntzelman, Lt Col Kurt W. "2 SOPS Mission Brief: GPS Ops and Applications", 27 Dec 2007.

[65] Larson, Wiley J. and James R. Wertz. *Space Mission Analysis and Design*. Microcosm Press and Kluwer Academic Publishers, third edition, 1999.

[66] Laskar, Jacques. "Introduction to frequency map analysis". C. Simo (editor), *Hamiltonian Systems with Three or More Degrees of Freedom*, 134–150. 1999.

[67] Laskar, Jacques. "Frequency Map Analysis and Quasiperiodic Decompositions". *Proceedings of Proquerolles School*, 1–31, Sept 2001.

[68] Lemoine, F. G., S.C. Kenyon, J.K. Factor, R.G. Trimmer, D.S. Chinn N.K. Pavlis and, C.M. Cox, S.M. Klosko, S.B. Luthcke, M.H. Torrence, Y.M. Wang, R.G. Williamson, E.C. Pavlis, R.H. Rapp, and T.R. Olson. "The Development of the Joint NASA GSFC and NIMA Geopotential Model EGM96", July 1998. URL `http://cddis.nasa.gov/926/egm96/egm96.html`.

[69] Little, Captin Brian. *Application of KAM Theorem to Earth Orbiting Satellites*. Master's thesis, Air Force Institute of Technology, 2009.

[70] Markeev, Anatoliy P. and Boris S. Bardin. "On The Stability Of Planar Oscillations And Rotations Of A Satellite In A Circular Orbit". *Celestial Mechanics and Dynamical Astronomy*, 85:51–66, 2003.

[71] Massatt, Paul and Michael Zeitzew. "The GPS Constellation Design - Current and Projected". *National Technical Meeting of the Institute of Navigation*, 435–445. Long Beach, California, 21-23 January 1998.

[72] McGill, Colin and James Binney. "Torus construction in general gravitational potentials". *Monthly Notices of the Royal Astronomical Society*, 244:634–645, 1990.

[73] Meirovitch, Leonard. *Methods of Analytical Dynamics*. McGraw-Hill Book Company, 1970.

[74] Metropolis, N., A. Rosenbluth, M. Rosenbluth, A Teller, and E. Teller. "Equation of State Calculations by Fast Computing Machines". *The Journal of Chemical Physics*, 21:108–113, 1953.

[75] de Moraes, R. Vilhena, K. T. Fitzgibbon, and M. Konemba. "Influence of the 2:1 Resonance in the Orbits of GPS Satellites". *Advances in Space Research*, 16(12):37–40, 1995.

[76] Morbidelli, Alessandro and Antonio Giorgilli. "Superexponential stability of KAM tori". *Journal of Statistical Physics*, 78(4-5):1607–1617, March 1995.

[77] Morbidelli, Alessandro and Massimilliano Guzzo. "The nekhoroshev theorem and the asteroid belt dynamical system". *Celestial Mechanics and Dynamical Astronomy*, 65:107–136, 1996.

[78] Moser, J. "On Invariant Curves of Area Preserving Mappings of an Annulus". *Nachrichten der Akademie der Wissenschaften in Gottingen. II, Mathematisch-Phusikalische Klasse*, Kl. II.:1–20, 1962.

[79] National Executive Committee for Space-Based Positioning Navigation and Timing. *Global Positioning System Standard Positioning Service Performance Specification*, 5 November 1993.

[80] National Executive Committee for Space-Based Positioning Navigation and Timing. *Global Positioning System Standard Positioning Service Performance Specification*, September 2008.

[81] Nekhoroshev, N.N. "An exponential estimate of the time of stability of nearly-integrable Hamiltonian systems". *Russian Mathematical Surveys*, 32:165, 1977.

[82] Ott, Edward. *Chaos in Dynamical Systems*. Cambridge University Press, second edition, 2002.

[83] Pace, James and P.J. Mendicki. "Telophonic and email correspondence", Feb 2009.

[84] Palacian, J.F. "Dynamics of a Satellite Orbiting a Planet with an Inhomogeneous Gravitational Field". *Celestial Mechanics and Dynamical Astronomy*, 98:219–249, 2007.

[85] Palma, Juliana and Julian Echave. "An analytical Fourier transform method for semiclassical quantization". *Chemical Physical Letters*, 270, 206–210. 1997.

[86] Pavlis, Erricos C. "Personal Correspondance on LAGEOS", Aug 2009.

[87] Perry, A. D. and S. Wiggins. "KAM tori are very sticky : rigorous lower bounds on the time to move away from an invariant Lagrangian torus with linear flow". *Physica D*, 71:102–121, 1994.

[88] Poincare, Henri. *Les Methods Nouvelles de la Mecanique Celeste*. Gautheir Villars, Paris, 1899.

[89] Priz, Ricardo, Beln Martn-Peir, and Miguel Romay-Merino. "The Galileo Constellation Design: A Systematic Approach". *ION GNSS 18th International Technical Meeting of the Satellite Division*. Long Beach, Califonia, 13-16 September 2005.

[90] Raquet, John. "Navigation Using the GPS Class Handouts", Spring 2000.

[91] Rossi, Alessandro. "Resonant Dynamics of Medium Earth Orbits: Space Debris Issues". *Celestial Mechanics and Dynamical Astronomy*, 100(4):267–286, 2008.

[92] Schutz, B. E. and D. E. Craig. "GPS Orbit Evolution: 1998-2000". *AIAA/AAS Astrodynamics Specialist Conference*. Denver, Colorado, 14-17 August 2000.

[93] Simoa, C. and T.J. Stuchi. "Central stable/unstable manifolds and the destruction of KAM tori in the planar Hill problem". *Phisica D: Nonlinear Phenomena*, 140(1-2):1–32, June 2000.

[94] Steichen, Daniel and Antonio Giorgilli. "Long Time Stability for the Main Problem of Artificial Satellites". *Celestial Mechanics and Dynamical Astronomy*, 69:317–330, 1998.

[95] Vallado, David A. *Fundamentals of Astrodynamics and Applications*. Microcosm Press, 2007.

[96] Violet, Michael D. "Re-tuning the GPS Constellation". *Performance Analysis Working Group (PAWG)*. 1999.

[97] Wiesel, William E. *Modern Astrodynamics*. Aphelion Press, 2003.

[98] Wiesel, William E. *Modern Orbit Determination*. Aphelion Press, 2003.

[99] Wiesel, William E. "Earth Satellite Orbits as KAM Tori, AAS 07-423". *AAS/AIAA Astrodynamic Specialist Conference*. 19-23 August 2007.

[100] Wiesel, William E. "Personal Correspondence Regarding KAM Tori Construction Algorithms", August 2008.

[101] Wiesel, William E. "Personal Correspondence Regarding KAM Tori Normal Coordinates", January 2009.

[102] Wiesel, William E. "Personal Correspondance on Earth Satellite Perturbation Theories as Approximate KAM Tori", Jan 2010.

[103] Wodnar, Karl. "A New Fast Fourier Method for Evaluating Fourier Spectra at Arbitrary Frequencies". *Celestial Mechanics and Dynamical Astronomy*, volume 65, 85–94. 1997.

[104] Wynne, Michael W. "Letter to Airmen, Air Force Smart Operations 21", March 2006.

[105] Yang, Won Young, Wenwu Cao, Tae-Sang Chung, and John Morris. *Applied Numerical Methods Using MATLAB*. John Wiley & Sons, Inc., 2005.

Vita

Major Ralph E. Bordner III was born in Peoria, Illinois. He was raised in Vero Beach, Florida from the age of 10, and he graduated from the Vero Beach Senior High School in 1991. He graduated from the University of Central Florida in Orlando, Florida in 1996 with a Bachelor of Science in Aerospace Engineering and a Minor in Aerospace Studies and from the Air Force Institute of Technology in 2001 with a Masters Degree in Astronautical Engineering. He has had papers published and presented with the American Institute of Aeronautics and Astronautics, of which he is a Senior Member. Since his commissioning on 5 May 1996, he has served at the 2nd Space Operations Squadron at Schriever AFB in Colorado Springs, Colorado, the National Air and Space Intelligence Center at Wright-Patterson AFB in Dayton, OH, and the Air Force Personnel Center at Randolph AFB in San Antonio, TX. Upon graduation he will be assigned to the Sensors Directorate of the Air Force Research Laboratory at Wright-Patterson AFB.

REPORT DOCUMENTATION PAGE

Form Approved
OMB No. 0704–0188

The public reporting burden for this collection of information is estimated to average 1 hour per response, including the time for reviewing instructions, searching existing data sources, gathering and maintaining the data needed, and completing and reviewing the collection of information. Send comments regarding this burden estimate or any other aspect of this collection of information, including suggestions for reducing this burden to Department of Defense, Washington Headquarters Services, Directorate for Information Operations and Reports (0704–0188), 1215 Jefferson Davis Highway, Suite 1204, Arlington, VA 22202–4302. Respondents should be aware that notwithstanding any other provision of law, no person shall be subject to any penalty for failing to comply with a collection of information if it does not display a currently valid OMB control number. **PLEASE DO NOT RETURN YOUR FORM TO THE ABOVE ADDRESS.**

1. REPORT DATE *(DD–MM–YYYY)*	2. REPORT TYPE	3. DATES COVERED *(From — To)*
30–09–2010	Doctoral Dissertation	Aug 2007 — Sep 2010

4. TITLE AND SUBTITLE

Orbital Tori Construction Using
Trajectory Following Spectral Methods

5a. CONTRACT NUMBER

5b. GRANT NUMBER

5c. PROGRAM ELEMENT NUMBER

6. AUTHOR(S)

Bordner III, Ralph E., Major, USAF

5d. PROJECT NUMBER

5e. TASK NUMBER

5f. WORK UNIT NUMBER

7. PERFORMING ORGANIZATION NAME(S) AND ADDRESS(ES)

Air Force Institute of Technology
Graduate School of Engineering and Management (AFIT/EN)
2950 Hobson Way
WPAFB OH 45433-7765

8. PERFORMING ORGANIZATION REPORT NUMBER

AFIT/GA/ENY/10-09

9. SPONSORING / MONITORING AGENCY NAME(S) AND ADDRESS(ES)

Intentionally left blank

10. SPONSOR/MONITOR'S ACRONYM(S)

11. SPONSOR/MONITOR'S REPORT NUMBER(S)

12. DISTRIBUTION / AVAILABILITY STATEMENT

Approval for public release; distribution is unlimited.

13. SUPPLEMENTARY NOTES

This material is declared a work of the U.S. Government and is not subject to copyright protection in the United States.

14. ABSTRACT

The Kolmogorov-Arnold-Moser (KAM) theorem states that lightly perturbed integrable Hamiltonian systems maintain their multiply periodic, toroidal motion in the phase space. The assertion that earth orbiting satellites under the influence of the geopotential mimic this behavior is the underlying premise of this work. This paper focuses on applying trajectory following spectral methods on selected orbits to decompose them into multi-periodic Fourier series, effectively compressing ephemerides for long-term use. The proposed approach focuses on fitting local spectral structures, denoted as frequency clusters, within the sampled orbital data to the analytical form of the windowed, truncated, continuous Fourier transform. This approach is significantly more numerically efficient than fitting every coefficient within the N-tuple Fourier series simultaneously. Numerical results using integrated data show maximum error in orbital torus fits can be kept at the single-digit-meter level per coordinate axis over a 1 year period.

15. SUBJECT TERMS

KAM tori, orbital tori, Fourier analysis, trajectory following spectral methods, Numerical Analysis of Fundamental Frequencies (NAFF)

16. SECURITY CLASSIFICATION OF:			17. LIMITATION OF ABSTRACT	18. NUMBER OF PAGES	19a. NAME OF RESPONSIBLE PERSON
a. REPORT	b. ABSTRACT	c. THIS PAGE			Dr. William E. Wiesel (ENY)
U	U	U	UU	185	19b. TELEPHONE NUMBER *(include area code)* (937)255-3636 x4312; william.wiesel@afit.edu